



**HAL**  
open science

## Coated single crystal superalloys: processing, characterization, and modeling of protective coatings

Vincent Maurel, Marion Bartsch, Marie-Helene Vidal-Sétif, Robert Vassen,  
Vincent Guipont

### ► To cite this version:

Vincent Maurel, Marion Bartsch, Marie-Helene Vidal-Sétif, Robert Vassen, Vincent Guipont. Coated single crystal superalloys: processing, characterization, and modeling of protective coatings. Nickel Base Single Crystals Across Length Scales, Elsevier, pp.283-338, 2022, 10.1016/B978-0-12-819357-0.00018-4 . hal-03599696

**HAL Id: hal-03599696**

**<https://hal.science/hal-03599696>**

Submitted on 1 Apr 2022

**HAL** is a multi-disciplinary open access archive for the deposit and dissemination of scientific research documents, whether they are published or not. The documents may come from teaching and research institutions in France or abroad, or from public or private research centers.

L'archive ouverte pluridisciplinaire **HAL**, est destinée au dépôt et à la diffusion de documents scientifiques de niveau recherche, publiés ou non, émanant des établissements d'enseignement et de recherche français ou étrangers, des laboratoires publics ou privés.

NiScAl

# Contents

<b>1</b>	<b>Coated single crystal superalloys</b>	<b>III</b>
1.1	Introduction . . . . .	V
1.2	Innovative materials and coating processes . . . . .	VIII
1.3	Characterizing properties of protective coating systems . . . . .	XVII
1.4	Properties of protective coating systems . . . . .	XXXII
1.5	Evolution of TBC microstructure and associated damage under thermal and thermo-mechanical loads . . . . .	XXXV
1.6	Challenges due to ingested mineral particles CMAS . . . . .	XLV
1.7	Modelling issues . . . . .	L



# Chapter 1

## Coated single crystal superalloys: processing, characterization, and modelling of protective coatings

Vincent Maurel<sup>1</sup>, Marion Bartsch<sup>2</sup>, Marie-Helene Vidal-Sétif<sup>3</sup>,  
Robert Vaßen<sup>4</sup>, Vincent Guipont<sup>1</sup>

<sup>1</sup>MINES ParisTech, PSL University, MAT - Centre des Matériaux, UMR  
CNRS 7633, BP 87, F-91003 Evry Cedex, France

<sup>2</sup>DLR Institute of Materials Research, Linder Höhe, 51147 Cologne, Germany

<sup>3</sup>Department of Materials and Structures (DMAS), ONERA Université Paris  
Saclay, F92322, Châtillon, France

<sup>4</sup>Institute of Energy and Climate Research: Materials Synthesis and Processing  
(IEK-1), Forschungszentrum Jülich, Jülich, Germany

### abstract

Superalloy parts are typically employed under high temperature conditions, often in hot gas paths of gas turbines for aviation or energy conversion. The thermal load of such parts is reduced by active back side cooling and additional application of thermal barrier coating systems. While the use of thermal barrier coating systems is industrial praxis, technological and scientific challenges are pushing the development of new coating systems and improved characterization and lifetime prediction methods. This chapter addresses some new developments which aim at allowing higher in-service temperatures and improving resistance

to harsh environments. Further, innovation in characterization, testing, and modelling of protective high temperature coatings is reviewed.

### **keywords**

*Thermal Barrier Coating (TBC); Emerging processes; oxidation protection; CMAS attack; damage mechanisms; characterization methods; thermal degradation; damage evolution; mechanical testing*

# Contents

## Glossary

APS air plasma spray  
BC bond coat  
BSE back scattered electrons  
CMAS calcia magnesia alumino silicate  
DIC digital image correlation  
EB-PVD electron beam physical vapor deposition  
NMG net mass gain  
OM optical microscopy  
RE rare earth element  
RT room temperature  
SE secondary electron  
SEM scanning electron microscopy  
SX single crystal  
TBC thermal barrier coating  
TC top coat  
TGO thermally grown oxide  
Y(P)SZ yttria (partially) stabilized zirconia

## 1.1 Introduction

Nickel based superalloys, especially single crystalline (SX) materials, are developed for parts operating under demanding conditions, such as gas turbine vanes and rotor blades. While the superalloys are optimized to sustain high thermal and mechanical loads, they need protective coatings against oxidation and corrosive attack. Further, the request for increasing the turbine inlet temperatures beyond the melting temperature of the superalloys motivated the implementation of active internal cooling of turbine vanes and blades. Applying an additional thermal barrier coating (TBC) system improved the efficiency of internal cooling, resulting in lower substrate temperatures or allowing either higher turbine inlet temperatures or reducing cooling air mass flow. Examples of TBC coated vane and blade for an aero engine are displayed in Fig. 1.1.

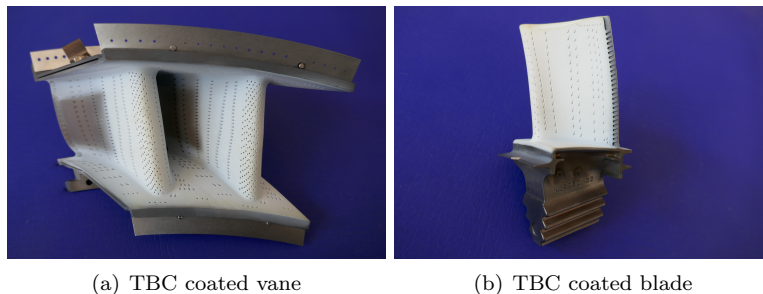


Figure 1.1: TBC coated vane (a) and blade (b) of a GP7000 aero engine

The most widely used material for thermal insulation is partially yttria stabilized zirconia (YSZ) with about 6-8 wt% yttria. The main coating technologies currently employed are electron beam - physical vapor deposition (EB-PVD) and air plasma spraying (APS) leading to highly porous coatings with a columnar or lamellar microstructure, respectively. The porosity entails a low thermal conductivity and a low elastic modulus, the latter providing a high strain tolerance. Since the YSZ allows fast diffusion of oxygen as well as transport of oxygen and corrosive media via open porosity, it is mandatory to apply onto the substrate metallic layers which provide a sufficient reservoir of Al or Cr to form  $\text{Al}_2\text{O}_3$  or  $\text{Cr}_2\text{O}_3$  diffusion barriers, referred to as thermally grown oxide (TGO) layers. Because the TGO formation improves the adherence of the ceramic top coat (TC), the protective metallic layer in a TBC system is referred to as bond coat (BC). Most BC applications are made either of NiAl, (Ni, Pt)Al, or MCrAlY (M representing Co or Ni). Figure 1.2 shows a schematic of a thermal TBC system, with typical EB-PVD and APS top coat, respectively. The range of typical values for thermal conductivity, thermal expansion coefficient (CTE), and Young's modulus are given in tables 1.1, 1.2, and 1.3 respectively.

The design of a TBC system, implying the composition and processing of each layer, TC, TGO, BC, and substrate, has a deep impact on the durability of TBC systems. Differences in thermal expansion coefficient (CTE) between the layers and mismatch of their elastic properties result in residual stresses and stress gradients across the layer system during temperature changes, such as cooling after processing or thermal cycling in service. Thermal gradients due to the internal cooling of coated components contribute to high stresses and stress gradients across the TBC system. Phase transformations, such as temperature dependent ductile-to-brittle transformations, may cause in some BC materials damage and subsequent failure of the TBC system. In service, time dependent processes, such as the growth of the TGO or sintering of the TC, change the stress field but also material properties, such as strength and fracture toughness. Especially, at the interfaces of different layers diffusion of elements is driven by concentration gradients and may lead to phase reactions or the formation of

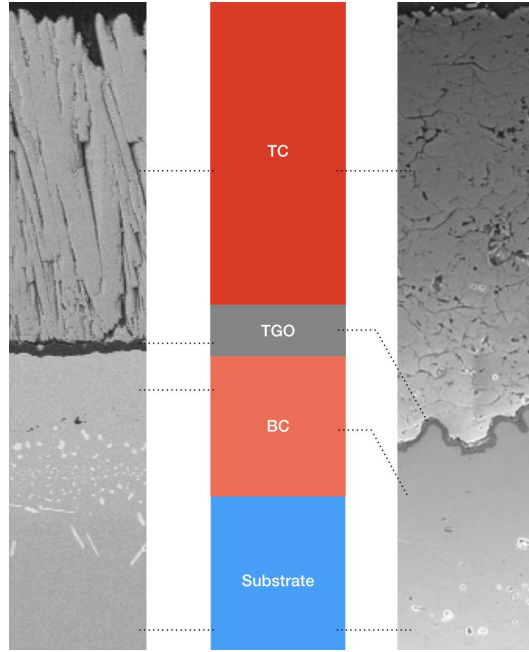


Figure 1.2: Typical TBC systems comprising ceramic TC, TGO, and metallic BC applied on a superalloy substrate. Left: EB-PVD processed TC with a (Ni,Pt)Al BC (courtesy of Lara Mahfouz) Right: APS processed TC with a MCrAlY BC adapted from [130]

voids and precipitates. Simultaneously, fatigue loads are effective, such as low cycle fatigue (LCF) associated to an entire engine cycle, e.g. one flight mission of an aero engine, or high cycle fatigue (HCF), e.g. associated to transient pressure differences.

TBC systems have been intensively investigated because of their importance for the performance of high temperature components made from Ni based superalloys and because of the implied technological and scientific challenges associated to their processing and use. Tremendous literature has been published on TBC systems for superalloys, including comprehensive overviews e.g. [47, 130, 150] or focused review articles, e.g. [157] on processing, [210] on industrial application, [57, 207] on lifetime modelling and testing.

However, continuing demands of increasing the turbine inlet temperature for raising the thermal efficiency of the gas turbine process entails new challenges for the coating systems and enhances research and development in processing and characterization of TBC systems. Another strong motivation for innovations is the need for lowering the production costs of high performance components with protective coatings. Main research activities aim at lowering thermal conductivity, improving phase stability at high temperature, limiting

sintering of the ceramic TC, controlling TGO formation and behavior during service, and developing measures to avoiding damage by the intake of low fusion point materials, such as volcanic ash or mineral deposits containing CaO-MgO-Al<sub>2</sub>O<sub>3</sub>-SiO<sub>2</sub>. These efforts include innovations in characterization, modelling, and lifetime assessment. Some of the recent developments which aim at allowing higher in-service temperatures and improving resistance to harsh environments are addressed in this chapter. Further, related innovation in characterization, testing, and modelling of protective high temperature coatings is reviewed.

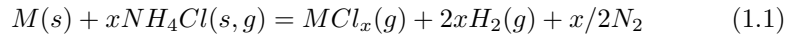
## 1.2 Innovative materials and coating processes

### 1.2.1 Corrosion protection layers

As single crystal superalloys are mainly developed towards high temperature mechanical properties, their oxidation and corrosion resistance is not sufficient to guarantee long-term operation at elevated temperatures under a corrosive environment. As a result, superalloys are in most cases coated with corrosion resistant coatings typically consisting of high aluminum and/or chromium containing alloys. The standard deposition methods are chemical vapor deposition (CVD) for aluminide coatings and different thermal spray techniques for NiCoCrAlY coatings. These deposition techniques as well as alternative routes are described in the following section. In addition to the corrosion protection, aluminide and MCrAlY coatings often serve as so-called bond coats for thermal insulation layers, the thermal barrier coatings (TBCs). Due to the rather high temperatures (above 900 °C) at the interface bond coat / thermal barrier coating, chromia scale formers are not suitable as the scale growth rates are high and additionally volatile CrO<sub>3</sub> species are formed at temperatures above 1000 °C [64].

#### Deposition from the gas phase: chemical vapor deposition (CVD) of aluminide and platinum aluminide coatings

Aluminide coatings are often deposited by CVD methods. A rather simple set-up using gas phase deposition is the pack cementation. In this process the parts are embedded into a powder mixture of a pure metal or alloy source (e.g. Al, FeAl, Al-alloys, or also Cr depending on the envisaged composition of the coating), a halide salt activator (e.g., NaCl, NaF, NH<sub>4</sub>Cl) and an inert filler material (often Al<sub>2</sub>O<sub>3</sub> powder) which guarantees a certain porosity level for the gas phase transport [211]. Under a controllable atmosphere, usually Ar or H<sub>2</sub>/Ar, this powder mixture, the pack, is heated to a temperature of 800 °C to 1000 °C. At this temperature the master metallic powder reacts with the halide salt activator to form volatile metal halide species providing significant partial pressures. In the case NH<sub>4</sub>Cl is used as the activator, the general reaction can be written as:



with M being Cr, however also other metals as Al or Si can be deposited; subscripts (s) and (g) correspond to solid and gaseous state, respectively. On the surface of the component the metallic chlorides decompose reacting with the nickel of the substrate to form intermetallics (NiAl) or forming metallic chromium layers [24]. The following focuses on aluminide coatings. A better control of the aluminide deposition process compared to the pack cementation is possible in a high temperature furnace in which activator gases as ammonium halides are passing through a porous bed of the source material (Al) and then flow along the surface of the components where the deposition takes place. Due to the gas flow used for the deposition (non-line of sight) also internal borings or complex shaped parts can be coated.

In the CVD process two extreme cases are established for the aluminide deposition: low and high aluminum activity coatings. The first type of coatings is deposited at high temperatures (1050–1100 °C) which lead to NiAl layers by Ni outward diffusion. The second type of coatings is made by deposition at low temperatures (750–900 °C) promoting aluminum inward diffusion resulting in Ni<sub>2</sub>Al<sub>3</sub> and NiAl layers [133]. A further improvement of the nickel aluminide can be gained by the addition of platinum. A thin platinum layer is deposited by electroplating up to about 10 μm, see Figure 1.3. In the subsequent aluminizing process the aluminum diffusion into the substrate is improved by the platinum. Both high and low activity aluminizing processes can be used leading to (Ni, Pt)Al and/or PtAl<sub>2</sub> containing coatings. The platinum significantly improves the oxidation properties of the aluminide coatings, however too large amounts of PtAl<sub>2</sub> might lead to a detrimental embrittlement. Also the formation of brittle interdiffusion zones between aluminide and substrate can be critical [64].

### Thermal spray techniques for NiCoCrAlY-coatings

Different thermal spray techniques are used to deposit NiCoCrAlY coatings on metallic substrates. In these coating processes a plasma gun which is accelerating and heating the powderous feedstock (particle sizes in the range between 10 and 100 μm) is mounted on a robotic system which moves along the surface of the component and allows the deposition of quite homogenous coatings in the range of 100 μm and above. Bonding in thermal spray processes is in most cases due to mechanical clamping. Therefore, a rough substrate surface is needed before coating. To achieve that, the substrate is often sand blasted by coarse (0.5 mm) ceramic (e.g. Al<sub>2</sub>O<sub>3</sub>) grids which gives roughness values of about  $R_a \simeq 5 \mu\text{m}$ .

The thermal spray technique which gives the lowest impurity content (mostly oxygen, content below 1000 ppm) in combination with low porosity values (below 1%) is vacuum plasma spraying (VPS). A micrograph of a VPS NiCoCrAlY is shown in Fig. 1.4(a). In this process, the plasma gun is operated in a chamber, which is first evacuated to pressures below 10<sup>-2</sup> mbar to remove mainly oxygen and then refilled by an inert gas up to about 50 mbar for spraying. Before spraying, typically a transverse arc cleaning is frequently applied for an

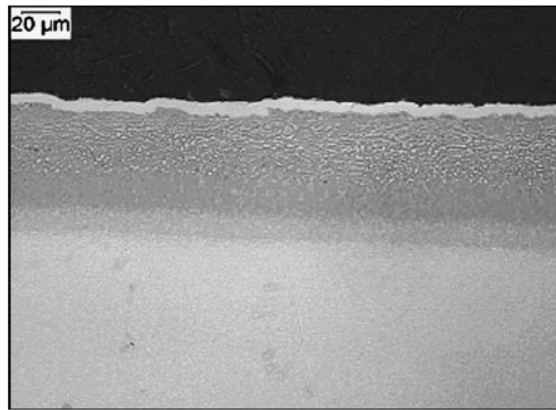


Figure 1.3: Optical micrograph of an outwardly grown platinum aluminide diffusion coating. The top thin white layer is electroplated nickel, used for edge retention during metallographic preparation of the sample. Image reproduced from [64]

effective removal of contaminations from the surface of the substrate.

Another thermal spray technique which is cheaper than VPS, as it does not need a vacuum chamber, is the high velocity oxygen fuel (HVOF) spraying. In this process, fuel which is kerosene, a hydrocarbon, or hydrogen, is burned at elevated pressures (about 6 bars) in a combustion chamber. The powderous feedstock is added and the particle loaded gas expands through a De Laval nozzle given supersonic conditions and hence very high impact velocities ( $>500$  m/s). A shroud gas (typically nitrogen) reduces the intermixing with the surrounding air and hence oxygen contamination. In combination with the rather short in flight time the oxygen content is limited (in the order of several thousand ppms) and the high velocity leads to rather dense coatings as seen in Fig. 1.4(b) [146]. Meanwhile, increasing numbers of especially stationary turbine parts are coated by HVOF spraying instead of VPS.

Another technology more recently used for bond coat application is high velocity air fuel (HVOF) spraying. In this process the pure oxygen of the HVOF process is substituted by air at a higher pressure level (about 10 bars) in special designed nozzles. The additional nitrogen in the combustion process leads to lower temperatures and higher velocities of the coating process (about 1000 m/s). Hence, dense coatings can be produced [218].

Another process using very fast particles is the cold gas spraying (CGS). Here the pressure level is further increased (in modern facilities about 50 bars). Even though the process is called "cold", the gas is heated up to more than 1000 °C to allow the formation of so-called shear instabilities during impact of the particles which gives dense coatings without melting. The avoidance of high temperatures during spraying reduces the oxygen up-take considerably. As mentioned above,

the major bonding mechanism in thermal spray is mechanical clamping. As a result, the bond coats deposited on the superalloys have to show a rather high substrate roughness (well above  $5\ \mu\text{m}$ ). This is often difficult to obtain with highly kinetic processes as HVOF and more specifically CGS. However, adequate selection of deposition parameters can lead to dense coatings with  $R_a$  values above  $10\ \mu\text{m}$  [41].

The last thermal spray method to discuss here is the atmospheric plasma spraying (APS). It is the cheapest process, however due to the mixing in of air a rather high oxygen up-take (in the percentage range) is observed. This leads to reduced oxidation properties and also the density is limited. Despite of these disadvantages, APS bond coats are used in commercial applications with limited thermo-mechanical loading. The importance of the oxygen level in the coatings is related to the so-called reactive elements (e.g. Y) in the coatings. These elements improve the bonding of the growing alumina scale to the bond coat and they also reduce the growth rates. If the bond coats take up oxygen during spraying mainly these reactive elements oxidize and they are no longer available for improving the oxidation behavior. However, also too good spraying conditions might be a problem as typically an excess of reactive elements is in the bond coats which might lead to increased internal oxidation if not bonded during thermal spraying [172].

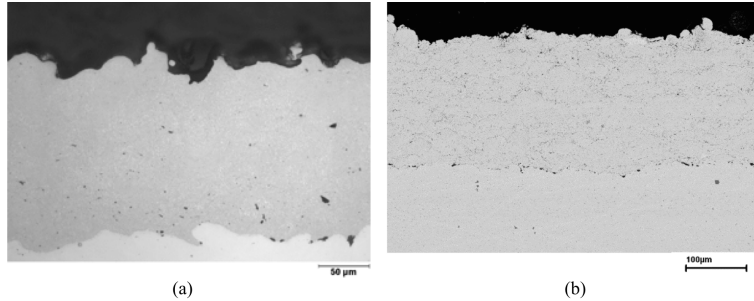


Figure 1.4: SEM micrograph of a VPS (a) and a HVOF bond coat (b).

The need for high density and simultaneously high surface roughness is difficult to achieve with only one process and just one particle size. Therefore, the combination of a dense coating (e.g. deposited by VPS using fine particles) with on top a coating with high roughness (deposited e.g. using large particles with APS) has been developed and is called flash coating. Essential for a good performance of flash coats is the good interconnection of the individual spray splats so that the aluminum can be supplied from the reservoir of the dense MCrAlY layer [128]. A final aspect which should be addressed here is the necessary compatibility of the bond coat with the substrate. As the chemical composition of bond coat and substrate is rather different, an interdiffusion e.g. of chromium and aluminum into the substrates and alloying elements of the substrate into the bond coat will take place. This can lead to the formation

of brittle phases as topologically close packed (tcp) phases and secondary reaction zones (SRZs) with coarsened  $\gamma/\gamma'$  microstructure [174], see more details in chapter ???. Furthermore, the reduction of the aluminum reservoir in the bond coat might reduce the lifetime of the coating.

### Other coating techniques

Also, the EB-PVD process can be used to deposit highly dense and homogeneous MCrAlY bond coats with a low amount of roughness. Due to relatively high costs this coating method is used in research environments [160]. Also slurries using fine aluminum particles can be used to manufacture aluminide coatings. The slurries are deposited by spraying on Nickel base alloy and performing a heat-treatment for the aluminizing step. If the process is made in air, the outer aluminum particles can oxidize and form a hollow sphere isolative layer [120].

### New bond coat approaches

Recently, the rather old idea of oxide dispersion strengthened (ODS) bond coats have been further developed [23]. These materials are adopted in their thermal expansion to the ceramic top coat and show often outstanding oxidation properties. They can be used as flash coats on top of a conventional bond coat. This approach led to excellent performance in TBC systems [199]. A further interesting new class of materials for the use as bond coats might be MAX phases. It could be demonstrated that these materials form a slow growing good adhering scale, e.g. made out of alumina, and can be used as bond coat [70]. In plasma-sprayed systems the bonding of the ceramic top coat to the bond coat mainly results from an interlocking at the roughness profile of the bond coat. This bonding can be further improved by introducing structures within the bond coat surface e.g. by laser ablation. Also the structuring of the substrate directly can be used [100].

## 1.2.2 Thermal insulation

### EB-PVD and APS as standard deposition methods for yttria stabilized zirconia coatings

Since several decades 6-8 wt. % yttria stabilized zirconia (YSZ) is the material of choice for advanced thermal barrier coatings for a number of reasons. The major reasons are a low thermal conductivity, a high thermal expansion coefficient (rather close to the substrate), high sintering resistance, and excellent toughness of YSZ. So the description of the processes will focus on this material although there are some drawbacks which will be discussed in the sequel.

The EB-PVD process uses an electron beam to heat a porous ingot of the coating material (e.g. YSZ) in a vacuum chamber above the melting temperature up to about 3500 °C. The porosity is needed so that the ingot can withstand the fast heating by electron beam. By this procedure the material is vaporized and condensates in a line-of sight process on the typically preheated

substrates with temperatures between 950–1100 °C. During the deposition a columnar structure with an often  $\{100\}$  texture is formed. The columns show a feather like outer structure and their microstructure can be adjusted by the proper choice of process conditions as substrate temperature, evaporation rate, or geometrical conditions (e.g. rotation) during deposition [160].

Defect free coatings can be deposited on rather smooth substrates with low roughness values typically below  $R_a < 2 \mu\text{m}$ . Here mainly aluminide or platinum aluminide bond coats are used. On the bond coat surface a thin alumina scale is formed before the EB-PVD deposition during a thermal treatment and further during the EB-PVD coating process, since a substantial partial pressure of oxygen is present in the coating chamber. The thin alumina scale is called thermally grown oxide (TGO) and ensures a good adhesion of the EB-PVD top coat.

The microstructure of such an EB-PVD system is shown in Figure 1.5(a). The columnar microstructure reduces tensile stresses in the coating. Such tensile loading is expected in a TBC system at elevated temperatures due to the higher thermal expansion of the substrate compared to the coating.

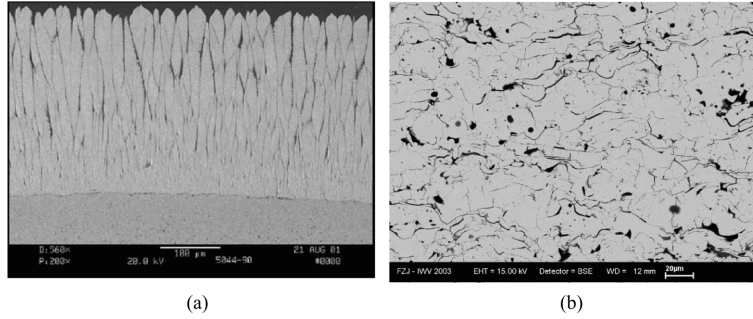


Figure 1.5: SEM micrographs of EB-PVD [64] (a) and APS (b) coatings.

In the atmospheric plasma spraying (APS) process powderous e.g. fused and crushed or spray dried feedstocks of YSZ in the size range between 20 and 60  $\mu\text{m}$  are used. The most often produced microstructure contains a lot of micro-cracks and pores giving a total porosity level above 10 % [177]. The micro-cracks are formed due to high tensile stress levels as a result of the fast cooling of the molten splats while the pores are due to the non-optimal filling of gaps between deposited splats by the newly arriving splats. In Fig. 1.5(b) the microstructure of such a TBC is shown. The micro cracks are essential for the good performance of APS TBCs as they allow some degree of strain tolerance due to the sliding of splats along each other [2]. In addition, the micro cracks are perpendicular to the heat flow direction leading to rather low thermal conductivities below 1 W/(m K) in the as-sprayed condition. Another microstructure often used for thick coatings in the micrometer range are segmented or also often called dense vertically cracked (DVC) coatings. In these coatings, high

substrate temperatures in combination with hot plasma conditions and good powder melting lead to dense coatings under high tensile stress. These stress levels initiate segmentation cracks [73]. The cracks are beneficial under high tensile loading as they can open, leading to reduced stresses. As the columns are rather dense, the thermal conductivity of segmented coatings is higher than that of micro cracked TBCs.

### Innovative thermal spray techniques

Instead of using powderous feedstocks also the injection of liquid suspensions or precursors is employed for the manufacture of thermal barrier coatings. At first, the suspension plasma spraying (SPS) will be described [62]. The suspension consists of fine scaled particles which allow the deposition of coatings with features in the submicrometer or even nanometer scale range. The suspensions can be introduced as a full stream or as atomized droplets into the plasma plume. In both cases the droplets are further fragmented into finer droplets by the high velocity plasma plume. The degree of atomization is depending on many process variables as the viscosity of the suspension, its surface tension, and the plasma conditions. As the droplets are much smaller than typical thermal spray powders, it is often, especially when using a radial injection, more difficult for fine droplets to penetrate into the center part of the plasma plume. This can lead to pore bands in the coatings from non-properly molten droplets at the outer fringe of the plasma plume.

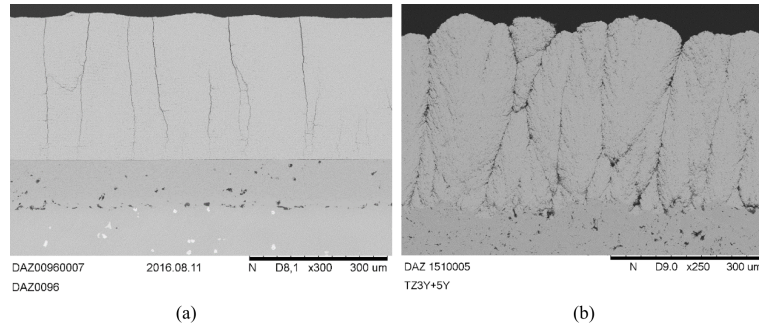


Figure 1.6: Suspension plasma sprayed coatings, (a) segmented and (b) columnar structured coatings (courtesy D. Zhou, Forschungszentrum Jülich).

The axial injection is certainly an advantage for the SPS process. After the fragmentation, the evaporation of the liquid carrier of the suspensions leads to a porous agglomeration of particles which sinter and then melt to form a liquid droplet. The SPS process can lead to highly porous coatings with porosity levels even above 40%. With this process also a highly segmented coating with a certain porosity level can be achieved (see Fig. 1.6). This microstructure shows interesting properties combining low thermal conductivity and Young's

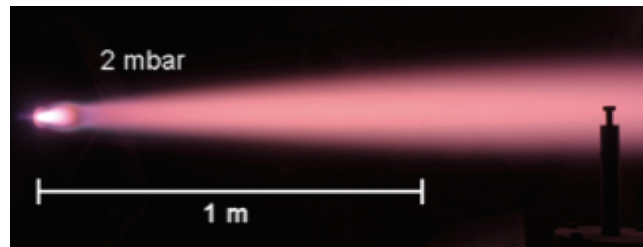
modulus with high strain tolerance due to the high amount of segmentation cracks [193]. A further step forward with the technology was possible with the development of columnar structured coatings by SPS. About a decade ago it was found that such coatings can be deposited under certain process conditions. The key for this development was the use of fine droplets with small Stokes numbers as they can be rather simply obtained in SPS. For these conditions the droplets follow the plasma plume parallel to the substrate instead of just directly impinging on it. They will hit obstacles on the surface of the substrates and these deposited droplets will form columns at these locations [191]. An example of such a columnar microstructure is shown in Fig. 1.6(b). Meanwhile the process has been introduced for the coating of gas turbine components.

In the solution precursor plasma spraying (SPPS) process also liquid feedstocks are employed, however, in this case the final coating material is formed during the deposition process by the decomposition of the precursors. This process offers the possibility to easily change and adjust the coating materials. On the other hand, due to the decomposition and formation step there are additional process variables which increase the complexity of the process. In the past, it was demonstrated that this process can be used for the manufacture of high performance TBC systems [86].

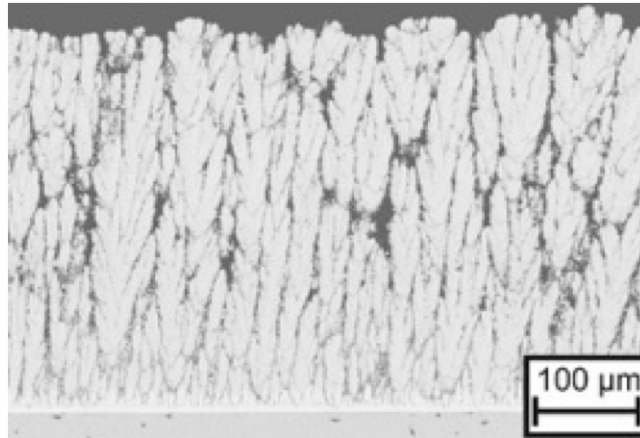
Another innovative process which was especially developed by Oerlikon Metco, Switzerland, is the plasma spray physical vapor deposition process (PS-PVD) [198]. This process is basically modified vacuum plasma spraying with powerful pumping units to maintain a low chamber pressure of about 1 mbar even with the inlet of process gas flows of 100 l/min. In addition, very powerful guns as the O3CP with up to a power of 180 kW are used. In this combination the plasma can expand to a length of more than 1 m (Fig. 1.7(a)). If specific fine powders are injected in the central part of the plasma, these powders are not only molten but even evaporated to a large degree. So coating deposition takes place from the gas phase similar to PVD, resulting in columnar microstructures (Fig. 1.7(b)). There are certainly differences to a conventional EB-PVD process, especially also due to the process gas flow, leading to a boundary layer which influences the deposition process [76]. Using optimized process conditions, a highly strain tolerant microstructure can be produced which shows extremely good performance in burner rig tests [153]. Meanwhile a number of PS-PVD coating facilities are in operation worldwide, especially in China a number of institutions are investigating the technology (e.g. [5]).

One interesting feature of both the PS-PVD and partly also the SPS and SPPS process is their non-line of sight characteristic. If particles/droplets to be deposited are small enough (e.g. their Stokes number considerably smaller than 1) they can follow the gas flow along the surface of the substrate before being deposited. In contrast to conventional thermal spray process this mechanism offers the possibility to coat also complex shaped parts with hidden surfaces.

An additional cost-efficient technique to apply TBCs is the use of slurry or sol-gel routes. Applications can be made by simple dip coating or spraying with a subsequent heat treatment. It could be demonstrated that coatings survive thermal cycling under rather moderate conditions [125].



(a)



(b)

Figure 1.7: (a) Photo of the plasma plume in the PS-PVD process, (b) SEM micrograph of the columnar structure of PS-PVD YSZ coating (courtesy H. Moitoux, S. Rezanka, Forschungszentrum Jülich).

### New Materials

Since more than two decades intense investigations have been made to find alternatives to the 4-5 wt.% yttria stabilized zirconia. The reasons are the claimed limited temperature capability of YSZ due to pronounced sintering and phase transition at temperatures above 1200 °C. The major identified materials are pyrochlores, perovskites [192], and zirconia with different dopants as rare earth elements [220] and five valent cations like tantalum [137]. A recent overview on the developments is given by Bakan [9]. An issue of many new ceramics especially if not using zirconia as base material is their low toughness which leads to early delamination. As delamination is often located close to the top coat/bond coat interface a possible solution to overcome this problem is the use of double layer coatings with a tough YSZ layer directly on the bond coat and on top a layer using the new material. In Fig. 1.8 such a double layer coating made by APS using  $\text{Gd}_2\text{Zr}_2\text{O}_7$ , an often employed new TBC pyrochlore material, as top layer is shown as a double layer system on the left, on the right a double layer using a perovskite sprayed by SPS is shown. Both systems showed an excellent performance in burner rig tests.

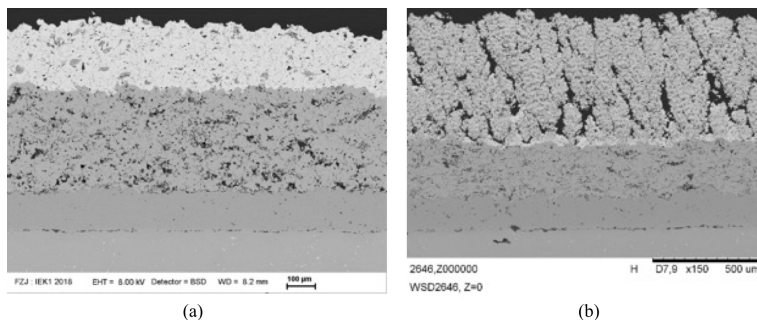


Figure 1.8: SEM micrographs of (a) an APS  $\text{Gd}_2\text{Zr}_2\text{O}_7/\text{YSZ}$  and (b) a SPS  $\text{La}(\text{Al}_{0.25}\text{Mg}_{0.5}\text{Ta}_{0.25})\text{O}_3/\text{YSZ}$  double layer system.

## 1.3 Characterizing properties of protective coating systems

### 1.3.1 Properties relevant for damage and failure behavior

Protective coatings on superalloy components for high temperature applications are multilayer systems with each layer having its special tasks and different properties. However, all layers have to be compatible during processing and service to maintain structural integrity of the coating system. Depending on the processing conditions transient thermal gradients may occur and lead to high residual stresses. In the case of EB-PVD coatings it is assumed that during the

deposition process the layered system is stress free at substrate temperature, which is typically in a range between 950 °C and 1100 °C. When cooling to ambient temperature, residual stresses build up depending on the CTE, the elastic constants, and yield strength of the individual layer materials. In service residual stresses are present because the temperature distribution in the coated system is always different to the temperature field during coating deposition. Additional stresses in the coating system originate from mechanically induced deformations of coated components, which are generated by e.g. aerodynamic forces or the rotation of engine parts.

Structural integrity of a TBC is ensured if stress, strain, and fracture mechanical load variables, such as stress intensity or strain energy release rate, are below the respective admissible values. Failure of a TBC system is associated to spallation of the ceramic thermal insulation which may occur due to an initial overload or delayed, as a consequence of stress build up and damage accumulation. For calculating the stress and strain state, knowledge of thermal conductivity, CTE, and the elastic constants is essential. Determination of yield strength is necessary to capture instantaneous stress relaxation and stress redistribution, respectively. Fracture strength and fracture toughness of individual layers and interfaces are key properties for evaluating if a coating may fail under an applied load. These properties are generally observed to decrease with time in service governing duration before failure.

### **1.3.2 Determination of thermal expansion coefficient and thermal conductivity**

For determining the CTE of individual coating layer materials dilatometry is well established. Since the CTE does not depend on microstructure features such as porosity, it can be measured using bulk material samples having the same crystallographic structure and chemical composition as the coating materials. Another option is X-ray diffractometry which allows for simultaneous determination of the crystallographic structure. For CTE data of substrates, bond coat, and TBC materials a huge number of data sets exists, however data can be found in diverse publications but are not yet summarised in central data banks.

Measuring the thermal conductivity of thin layers is still challenging. Microstructure has a crucial impact on the thermal conductivity. Thus, it is not possible to simply use data from reference bulk material, especially not for the porous ceramic topcoat of a TBC system. If gradients in the microstructure occur over the layer thickness, as it is the case for EB-PVD coatings, the thermal conductivity is a function of the layer thickness. Further, the partial transparency of YSZ coatings for infrared radiation has to be considered. Therefore, it is not sufficient to know the thermal conductivity of the solid but the total heat transfer coefficient should be known.

To achieve accurate data for the thermal conductivity of ceramic TBC layers, well established methods for measuring solid conductivity have been refined. E.g. [149] applied the laser flash method (ASTM, E 1461-01) to determine the

### 1.3. CHARACTERIZING PROPERTIES OF PROTECTIVE COATING SYSTEMS XIX

thermal diffusivity on free standing EB-PVD processed coating samples. This technique allowed a higher accuracy than using multi-layered samples with the coating applied on the superalloy substrate. Coatings of more than 200  $\mu\text{m}$  thickness were separated from the metallic substrate by chemical etching. Very thin layers of 50 - 200  $\mu\text{m}$  were deposited on a sapphire substrate of about 1 - 2 mm thickness, which is transparent for the laser light of the laser flash apparatus but ensured that the fragile coating stayed intact. Further, a thin platinum layer was sputtered on both surfaces, which reduced radiation into the sample on the side where the laser hits the sample and improved on the back side the detection of the temperature signal by an infrared detector. The thermal conductivity  $\lambda$  is then calculated via the relationship  $\lambda = a \times C_p \times \rho$  with the thermal diffusivity  $a$ , the specific heat capacity  $C_p$ , and the density  $\rho$ . The specific heat capacity is determined by means of differential scanning calorimetry (DSC) or differential thermal analysis (DTA) and does not depend on the microstructure. The density is typically determined at ambient temperature by established standard methods, and the temperature dependency of the density is derived from temperature dependent CTE data. The experiments presented in [149] showed that the thermal conductivity of a 300  $\mu\text{m}$  thick EB-PVD processed YSZ coating was about 40% higher than that of a 50  $\mu\text{m}$  thick coating. This significant difference can be explained by the gradient in the coating microstructure. The much smaller columnar grain size at the interface to the substrate, compared to the grain size in some ten microns distance, results in a higher thermal resistance due to the higher density of grain boundaries.

The effect of heat transfer in ceramic insulation layers by radiation and the factors influencing it have been discussed in a review by [126]. For reducing radiation, addition of dopant materials and introduction of internal interfaces such as grain boundaries, especially perpendicular to the direction of the heat flux, are proposed. However, quantitative experimental data are rare. One detailed study on a 280  $\mu\text{m}$  thick free standing EB-PVD YSZ coating is presented in [104]. Experimental data of thermal conductivity from laser flash testing and of transmittance and emittance, using the integrated sphere method at ambient temperature and the black boundary condition method for elevated temperatures, were combined to determine the contribution of radiation on the total heat transfer. Depending on thermal history of the coating the contribution of radiation at 1150 °C was about 18% (after 100 h at 1100 °C) and 24% (after 2 h at 1080 °C). The differences between the differently heat treated samples are attributed to microstructural changes, especially of the pore size and shape, due to sintering effects. Comparing EB-PVD and APS coatings, the lamellar microstructure of APS coatings provides much more internal interfaces perpendicular to the heat flux and is expected to be less prone to heat transfer by radiation.

In APS coatings the microstructure is much more homogenous over the coating thickness than in EB-PVD coatings and does not depend on the coating thickness. Therefore, it may be expected that the experimental procedure for measuring thermal conductivity of APS coatings is quite robust. However, thermal conductivity data reported in literature show a wide spread, which makes

it difficult to decide which values to use for numerical calculations. A database for thermal transport properties of APS coatings is provided in [202]. Thermal diffusivity data from more than 200 APS coatings with standard composition of  $ZrO_2$  with 7-8 wt. %  $Y_2O_3$  have been collected over 12 years in collaboration of 16 Institutes and companies. All data points were included in one diagram (Figure 1.9), revealing a huge scatter band.

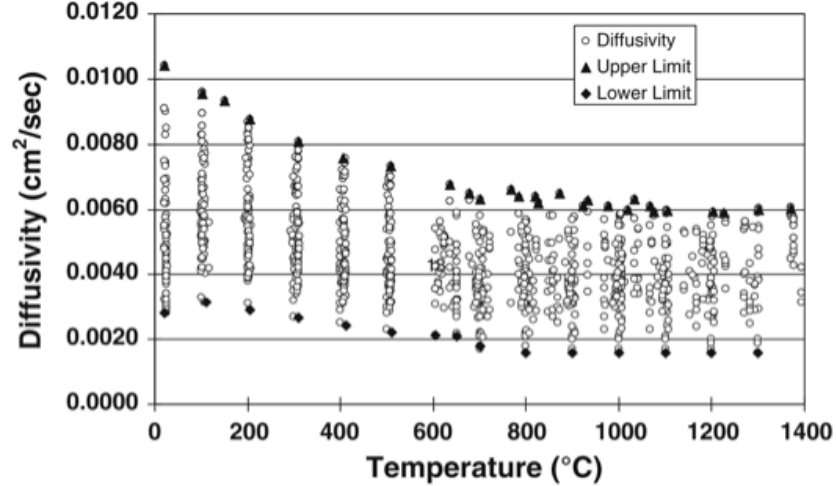


Figure 1.9: Spread of thermal diffusivity data of 133 APS 7-8 wt % YSZ TBC collected by [202]

### 1.3.3 Characterizing mechanical properties of the different coating layers (BC, TGO, TC)

#### Mechanical testing of the TBC system

To assess mechanical properties of a TBC system, testing of a complete TBC system, including the superalloy substrate, enables to capture the effect of constraints and interactions between the layers. For evaluating test results achieved on the complete layered structure, inverse analyses, either by analytical approaches or employing numerical methods such as Finite Element Analyses (FEA) are needed. However, the range of thicknesses in a typical TBC should be kept in mind: 100-200  $\mu\text{m}$  for the EB-PVD TC (up to mm for APS TC), 1-8  $\mu\text{m}$  for the TGO, 50-100  $\mu\text{m}$  for the BC and IDZ, and 0.5-2 mm for the substrate. Thus, mechanical testing of a complete TBC system including the entire substrate would hardly provide relevant information of each layer. To overcome this issue several authors have developed tests with reduced thickness of the substrate. Taylor et al. have developed a high temperature creep test based on reduced thickness of the substrate [176]. Since their work focused on the BC

### 1.3. CHARACTERIZING PROPERTIES OF PROTECTIVE COATING SYSTEMSXXXI

properties, they applied this method on a system without TC and were able to improve the sensitivity of the method [176]. For mechanical evaluation of a complete TBC system, Hemker and coworkers have developed a micro-bending facility where the substrate thickness has been further reduced. This approach enables a direct view of the cross-section, and thus digital image correlation (DIC) could be used to measure the strain and strain gradient in each layer, yielding the mechanical behaviour of the layers and enabling the assessment of interfacial fracture toughness at room temperature [53]. Using such methodologies at high temperature needs to consider ageing of the layered system due to diffusion or oxidation, respectively. While oxidation can be reduced by testing in vacuum, diffusion processes at the interfaces between the layers cannot be avoided.

Tensile testing of substrates coated with a BC layer only has been conducted in [54] to identify the strain at crack initiation as a function of aging. This is done in using a high-resolution optical microscope together with a CCD camera to measure in situ both crack initiation and strain field by DIC. The strain field measurement is a key tool to assess the local critical strain to coating cracking, in particular when strain localization is observed in the single crystal substrate, Figure 1.10(a). This methodology does not modify the coating and substrate interactions and is very straightforward to handle with the modification of properties with phase transformation due to aging. It has been evidenced that for (Ni,Pt)Al bond-coat the thermal cycling has induced both surface roughness evolution, so-called rumpling effect, see Fig. 1.10(b), and phase transformation from  $\beta$  to  $\gamma'$  (Fig. 1.10(c)).

The use of intermetallic BC, which is brittle in a wide temperature range, can induce crack initiation at a very low strain level [117]. During thermo-mechanical fatigue (TMF), it has been evidenced that the substrate can stand compressive strain dwell at high temperature leading to substantial stress relaxation, which results for out-of-phase TMF loading in tensile stress in the low temperature range [151]. Thus, the substrate can fail due to crack initiation in the metallic bond-coat and further crack propagation into the substrate [55].

Emerging synchrotron facilities providing high energy X-rays enable to access the local strain in layered systems in situ via X-ray diffraction. At the advanced photon source (APS) of the Argonne National Laboratory Knipe et al. have assembled a thermal-mechanical fatigue testing equipment and used it to determine the strain evolution in each layer of an EB-PVD coating system during combined thermal and mechanical loading [95]. The strain in BC and TC (see Fig. 1.11) and later in TGO of an aged system with sufficiently thick TGO has been determined based on the  $\theta - 2\theta$  method [95, 105].

#### **Free standing coating**

An alternative approach promotes a complete identification of mechanical behavior of the individual coating layers using free-standing coatings [131, 3, 182]. It is possible to obtain small-scale specimen by either manipulating the coating process for inhibiting the adherence of the coating to the substrate by electro-

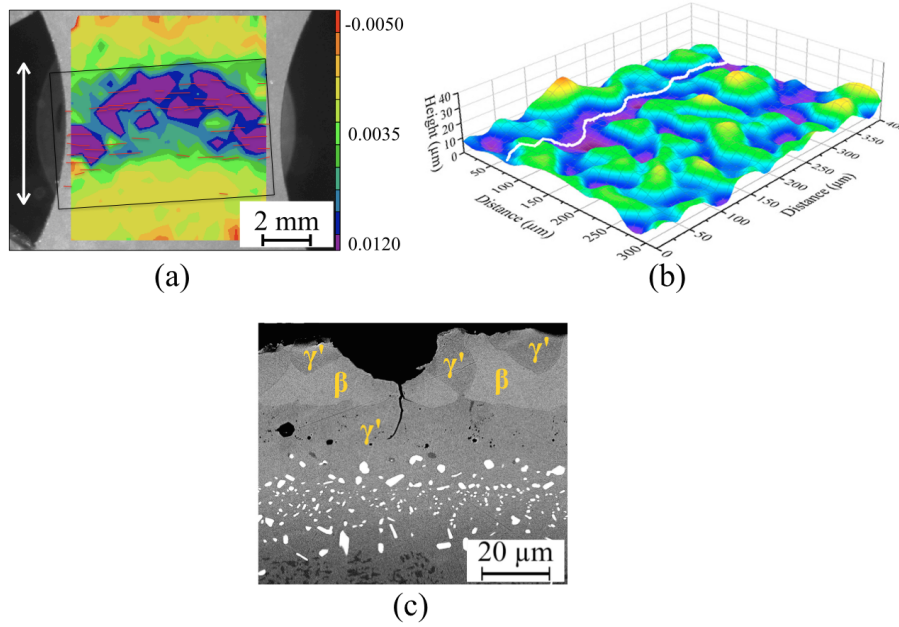


Figure 1.10: Tensile room temperature test on a substrate with BC after ageing by thermal cycling. (a) Strain field measured by DIC on the surface of the coated specimen with associated BC cracks indicated by short red lines; load direction corresponds to the double arrow, (b) roughness measured on the surface and associated crack path in white, and (c) phase transformation from  $\beta$  to  $\gamma'$  (adapted from [54])

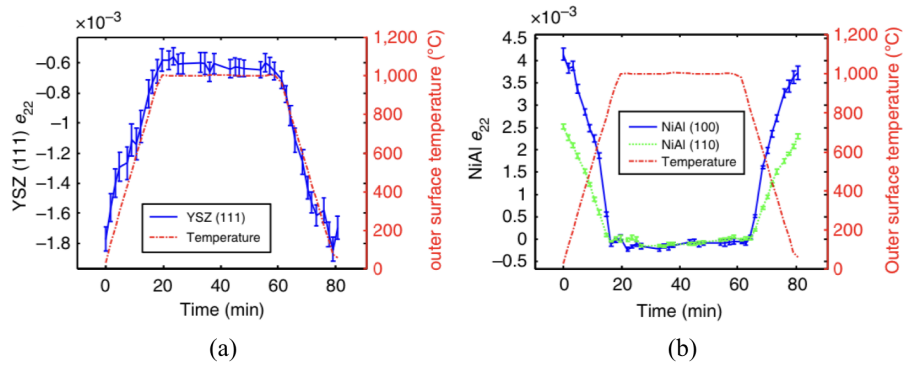


Figure 1.11: In situ measurement of temperature and strain in the loading direction in (a) YSZ layer and (b) in NiAl layer [95]

discharge machining of the coating or polishing of a ribbon from the TBC system. This kind of approach enables to measure the stress strain relationship on free standing coatings. Due to their ductility, BC samples can be tested under tensile load, see Figure 1.12(a). Targeted preparation allows also to investigate the deformation behavior of the diffusion zone between BC and substrate.

Again, strain measurement is improved by the use of DIC technique for strain field measurement. This strain field measurement enables to control the homogeneity of the loading within the gage length. This last point is a challenging issue for micro-testing. For instance, it has been shown that for (Ni,Pt)Al coating the aging in isothermal condition leads to a strong modification of the mechanical properties over a wide range of temperature, mainly induced by phase transformation from  $\beta$  to  $\gamma'$  [131, 3]. In contrast, for MCrAlY coating the internal oxidation will drive the mechanical behavior, limiting drastically the ductility increase induced by phase transformation from  $\beta+\gamma+\alpha$  to  $\beta+\gamma'+\alpha$  [179]. For new generation of so-called  $\gamma/\gamma'$  coatings, it has been shown that at RT the associated ductility was higher than the one observed for (Ni,Pt)Al coatings, but surprisingly at elevated temperature (870 °C) some authors have shown that the  $\gamma/\gamma'$  coatings fail brittle by intergranular cracking, which entails cracking of the substrate, while (Ni,Pt)Al coatings are highly ductile at this temperature [3]. In this case, the authors have tested both free standing coating and coated substrate. Testing of freestanding coating was straightforward to establish damage mechanism and to confirm for the  $\gamma/\gamma'$  coating that intergranular failure within the coating was the driving damage mechanism limiting the life of the coated substrate. Comparison of damage behaviour of a coating system with thinned substrate and applied (Ni,Pt)Al coating and free standing BC specimen were consistent, e.g. see Figure 1.12(b) where cleaved grains are observed in BC and are associated to brittle behaviour for tests conducted at low temperature.

### Micro- and Nanoindentation

Micro- and nanoindentation are interesting tools to map room-temperature elastic properties of TC, TGO, BC, inter diffusion zone (IDZ), and secondary reaction zone (SRZ) when developed in the substrate, Figure 1.13 [223, 129]. Besides, a complete analysis of pile-up or sink-in associated to indent yields access to elasto-viscoplastic behavior of the studied material [152]. The major interest of nano-indentation is to achieve local information at a submicron length scale that enables to determine individual phase behavior. Development of such methods with multi-points analysis yields elastic properties mapping in a very short-time [134]. On the other hand, the characterization of the plastic behavior needs to be coupled with FEA and local measurement by AFM and is subsequently highly time consuming. It is worth noting that the aging of APS YSZ impact elastic modulus significantly [20]. In the field of micro-testing, a recent overview addresses strengths and weaknesses of different techniques that can be used [46].

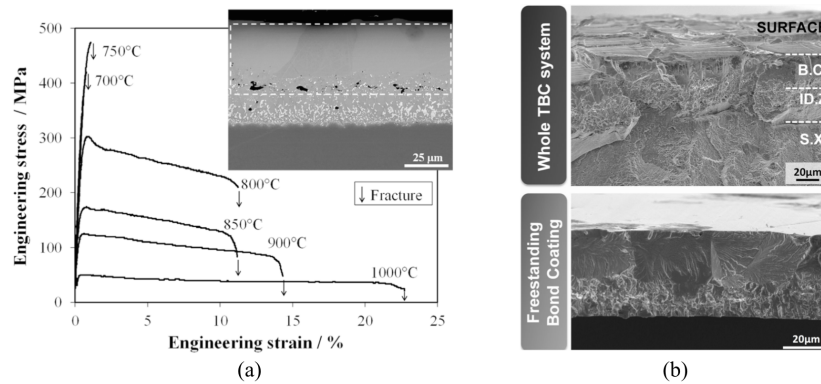


Figure 1.12: Tensile test on free standing BC specimens for (Ni,Pt)Al coating, (a) stress-strain curves at different temperatures and (b) fracture surfaces of specimens comprising SX substrate material, BC, and inter diffusion zone between SX and BC (right top) and BC only specimen (right bottom) [182]

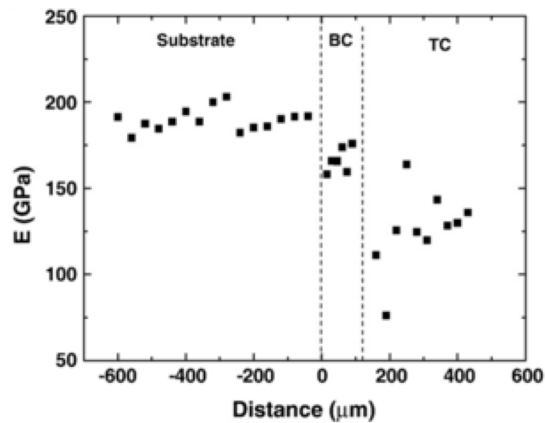


Figure 1.13: Young's modulus measurement by nanoindentation across an EB-PVD TBC system, see high dispersion in the TC associated to local intercolumnar voids [223]

### 1.3.4 Adherence of the ceramic coating layers - interfacial strength and fracture toughness

One of the major issues in TBC technology is to manage the adherence of the top coat on the substrate in the as-processed and for relevant aging conditions regarding the spallation process. Adherence of the bond-coat is seldom an issue since the processing methodology of metallic bond coats has been established for decades. However, the choice of adherence testing methodology is still chal-

### 1.3. CHARACTERIZING PROPERTIES OF PROTECTIVE COATING SYSTEMSXXXV

lenging and the lack of confidence in interfacial adherence measurement is certainly limiting robust modeling of TBC damage until failure by spallation. Tests methods for determining the adherence of a coating are evaluated using criteria of robustness (is the test reproducible?), modification of the TBC system (is there an artifact in testing conditions?), relevance of the loading as compared to in-service loading (how close to reality is the lab testing condition?) and easiness of intrinsic physical/mechanical property measurements (is the result straightforward for further modeling or limited to testing conditions?). To promote spallation of a top coat most popular methods are Tensile Adhesion Test (TAT), barb test, shear test, indentation testing (including scratch test), bending testing, and compression testing. The laser adhesion test (LASAT), which is a quite new method, will be described in more detail and evaluated. This method is based on a laser driven shock wave causing debonding of the TC. In the following, each class of adherence tests is briefly described and ranked with respect to above listed criteria. Noteworthy, TBC spallation occurs mostly at low temperature after thermal exposure. Stress relaxation at high temperature entails build up of high compressive stress in the ceramic coating layers (TC and TGO) when cooling. Thus, room temperature testing for adherence measurement is straightforward.

#### **Tensile Adhesion Test**

For performing the Tensile adhesion test (TAT) one cylinder with clamping extension is glued onto the top coat and another cylinder on the opposite side onto the substrate, aligned so that by applying a sufficient force, the coating is separated from the substrate (Figure 1.14(a) and (b)). The force is controlled by a load cell, and the values measured during the experiment are force and displacement [141].

While typically only the force needed for separating the coating from the substrate is exploited, Figure 1.14(c) reveals that the test configuration, i.e. the diameter ratio between the cylinder glued to the coating and the one glued to the substrate, influences the stress distribution over the glued area. Therefore, the separation force is not an intrinsic measure for the coating adherence but can rather provide a ranking of coating adherence for one specific test configuration.

#### **Shear Test**

The barb test has been proposed to apply a shear loading on a coated substrate, Figure 1.15(a) [74]: using a cylindrical substrate, the coating is partially removed by machining. The shear force is controlled by a die moving along the cylinder. The measured values are force and displacement [74]. Alternatively, a pillar can be machined from a TBC system, and shear loading can be obtained by moving a blade applied to the top coat up to delamination of the top coat, Figure 1.15(b) [212]. Some authors have also used indentation testing, where indent is achieved on cross section, or scratch test where indenter is moved along the top coat; recently this kind of test has been modified using laser impulse to

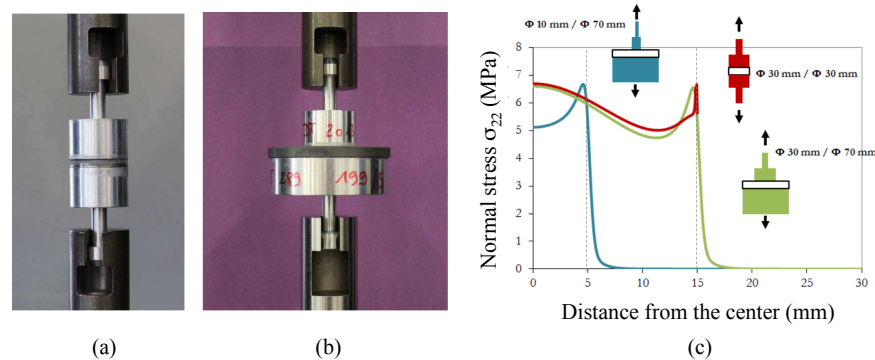


Figure 1.14: Tensile adhesion testing, (a) test configuration with both cylinders glued to the coated sample having the same diameter as the circular sample disc, (b) test configuration with a larger cylinder glued to the substrate side and a smaller to the coating side, with the sample diameter similar to that of the larger cylinder, (c) distribution of the stress component in loading direction from the sample center to the edge for different test configurations (adapted from [141])

promote scratch, e.g. see the review of Chen et al [35].

### Bending test

Bending and punching tests (where punch is applied at the center of a circular clamped plate) can be either used directly on the TBC system without any modification or used by gluing a stiffening plate on the TC surface and machining a notch, Figure 1.16 [39, 138, 184]. The stiffener enables to access energy measurement from simple modeling (analytical or FEA) [184]. By playing on condition of bending, 3- or 4-points bending, symmetric or non symmetric set-up, authors can access to mode I or mode I + II varying the mixity angle, Figure 1.16(a) and (b) [195]. Bulge and buckle testing consist in applying a force or a pressure to push the coating from the substrate (using screw, gaz or thermal shock), but these techniques are mostly applied to thin films or at least very flexible coating material [35].

### Compressive testing

Compressive testing consists in a strain-controlled test under compression, using cylindrical specimen with a sufficient diameter to length ratio for avoiding macroscopic buckling of the specimen before top coat spallation. This configuration simulates compression induced by CTE mismatch on cooling and promotes mode II decohesion, Figure 1.17 [40, 111, 169, 221, 87].

1.3. CHARACTERIZING PROPERTIES OF PROTECTIVE COATING SYSTEMSXXXVII

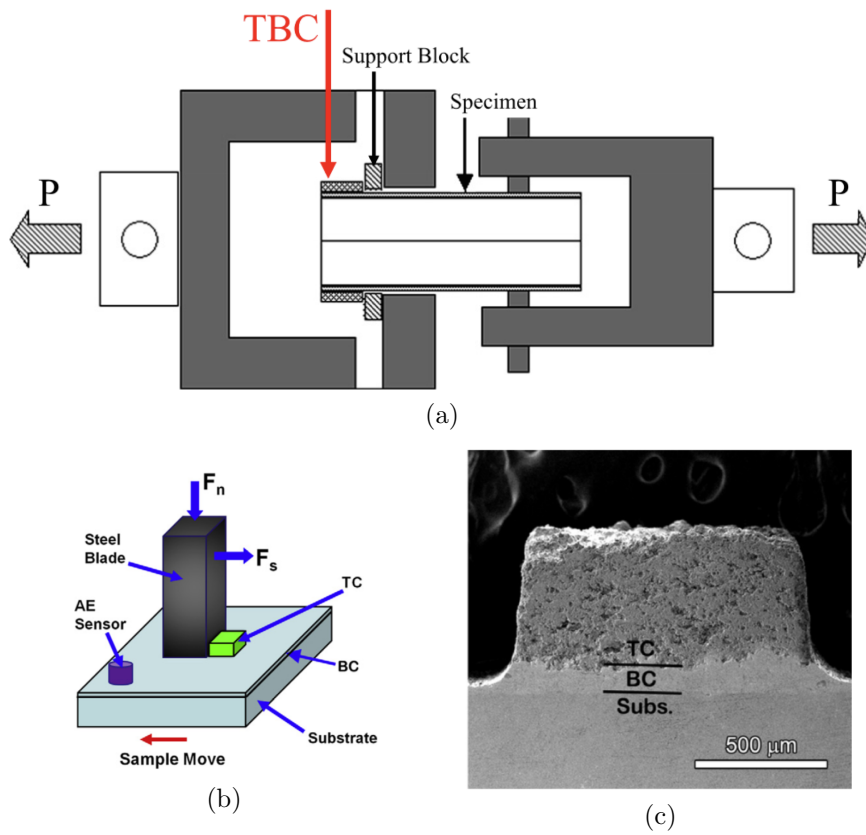


Figure 1.15: (a) Barb test from [74] and (b) shear test from [212], (b) sketch of the set-up and (c) SEM image of the machined specimen, side view

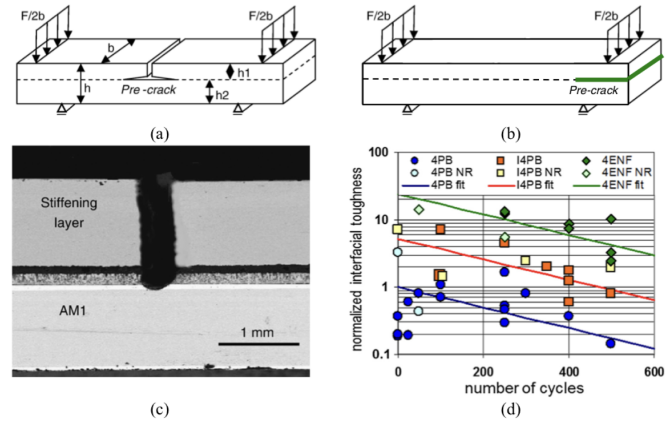


Figure 1.16: Four point bending testing with stiffening layer (a) for mode I testing "4PB" (b) for mode I and mode II "4ENF" (c) detail of notched area for "4PB" test (d) measured interfacial toughness where 4PB corresponds to (a), I4PB same as in (a) except that specimen is upside-down in the set-up so as to promote compression in the top coat and 4ENF corresponds to (b); from [184, 195]

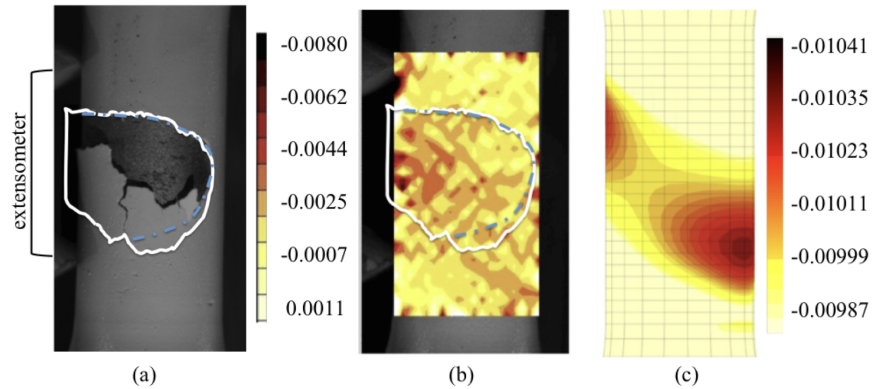


Figure 1.17: Compressive testing, (a) in situ optical observation after first spallation event, (b) strain field component in the loading direction measured by DIC: blue line represents failed ceramic observed in (a) and white line corresponds to measurement achieved by SEM, (c) strain field component in the loading direction obtained by FEA considering the misorientation of the single crystalline substrate (adapted from [108])

### **Laser Shock Adhesion Test (LASAT)**

The laser shock adhesion test (LASAT) method consists in a shock wave propagating throughout a TBC system and inducing a tensile stress at the interface. With a nanosecond pulse and a confinement medium (e.g. water or transparent adhesive tape), laser power densities from 0.1 to 8 GW/cm<sup>2</sup> can be introduced at the metallic side of a coated sample with laser spot diameters of a few mm, yielding a strain rate  $\sim 10^4 - 10^6 \text{ s}^{-1}$  in the direction of the shock wave propagation within the substrate. A so-called LASAT threshold can be measured on a coated plate by testing the minimum laser power density needed to debond the TC [19]. LASAT has also been implemented on coated turbine blades and is envisaged as a semi-destructive adhesion test [17]. Quantitatively, velocimetry temporal profiles are needed to calibrate the input stress temporal profile with peak stress in GPa and corresponding laser power densities in GW/cm<sup>2</sup>. For thick multilayered coatings like TBCs, inverse analysis of shockwave propagation is implemented by 1D Finite Difference or 2D Finite Element methods to establish the stress history (mainly in mode I) at the interface for a given input laser energy, especially the critical energy for generating the debonding threshold stress.

Based on 2D FEA, the lateral expansion (orthogonally to the principal direction of propagation) of the shockwave has been evidenced to yield larger delamination than the laser shock diameter for high energy [61]. This effect is detailed as the LASAT 2D effect. These 2D effects can explain the monotonous increasing of the crack size with the laser energy that gave a rise to the so-called 'LASAT-2D curve' as experimental output for the LASAT-2D method applied to ceramic coatings [61, 17]. It is worth noting that for typical EB-PVD TC, the LASAT induces debonding and consequently blistering of the TC due to the residual stress release. Based on elastic analysis of the blistering condition, it is possible to access the energy release rate at crack arrest making LASAT a very efficient tool to evaluate interfacial toughness [114, 72].

### **LASAT to process internal "notch" for further loading**

Thanks to the robustness of the LASAT method, it is quite easy to establish a 2D-LASAT curve (in the as-processed or aged condition) yielding the evolution of debonded diameter as a function of the LASER energy, Figure 1.18(b). It has been proposed to use a decohesion processed by LASAT to obtain a notch-like defect, this defect being circular and "blind" in the sense it is not emerging on any side of the specimen. By this way, NDT techniques can be used to monitor damage evolution from the LASAT defect, Figure 1.18(c). This methodology has been successfully applied to access damage evolution during either mechanical test [159], furnace thermal cycling [110], or burner rig test [112]. Associated to cohesive zone model (CZM) or by elastic analysis of the TC blistering, the interfacial toughness can be deduced from these tests as a function of any loading condition (thermal and/or mechanical loading) [159, 72].

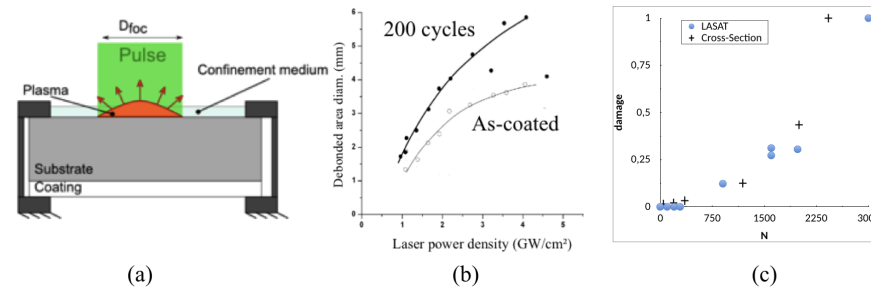


Figure 1.18: Laser Shock Adhesion Testing (LASAT) for the same EB-PVD YSZ, (Ni,Pt)Al coating AM1 single crystal system, (a) set-up and (b) examples of LASAT-2D curves in as-coated condition and after 200 thermal cycles (adapted from [60, 17, 72]), (c) comparison of damage size evolution (normalized) from artificial defects processed by LASAT measured by IR top-surface imaging (non destructive) and on SEM cross-sections (adapted from [186, 110])

### Comparative analysis

Even though tensile adhesion testing is the most popular method to characterize coating adherence, major drawbacks are limiting definitively its robustness: it is rather difficult to reproduce the same condition from test to test because the glueing influences the measurement result. Indeed, glue can penetrate porous coatings, modifying local stiffness, but mainly add a damageable layer modifying both stiffness and damage evolution. Moreover, the quantity to be measured is stress at decohesion which quantity is not seen as an intrinsic characteristic: it has been clearly established that the stress distribution within the specimen is not uniform and depends on the size of the cylinder chosen for both substrate side and top coat side [141]. The limitation in robustness is also observed for all methods including either gluing of a part (TAT, shear and bending tests when used with stiffener-plate) or machining modifying locally the microstructure of the interface (barb test, bending with notch), Figure 1.16(c). It is worth noting that the machining will probably induce micro-cracking at the interface without any possibility to control this micro-crack in size and shape, and thus will increase the level of scatter of experiments, Figure 1.16(d).

However, another strong limitation is due to the relevancy of loading as compared to in-service use. Because damage leading to spallation of a TBC system is mainly induced by CTE mismatch between each layer, in-service loading is associated to mode II cracking in the presence of micro-cracking mostly located at the TC/TGO interface for EB-PVD coating under thermal cycling [213]. Therefore, only barb, shear and compression testing seems to be fully consistent with this point. Barb and shear test enable to access directly  $K_{II,c}$  but with strong modification of the TBC system that could be a bias to the measured values. Compression testing enables to access local strain at decohesion

and spallation of the top coat, the spallation being driven by local maximum strain arising from localization in the substrate or bond-coat analyzed by DIC, Figure 1.17 [108]. However, strain at spallation does not take into consideration the actual mechanical state, that is to say that the residual stresses are not considered or should be addressed by modeling. This limitation is also a drawback for other methods. Both indentation and scratch tests have further major drawbacks considering their relevancy compared to in-service loading. For indentation achieved on cross-section, the indentation location has a major impact on results. This becomes an issue for rough interface, where it is rather difficult to determine precisely the location of measurement. Scratch testing, is straightforward to rank different coating solutions, but again it suffers from a very complex loading very far from the in-service one, except in the field of abrasible coatings. A comprehensive overview of the role of mode mixity and associated testing methods has been given by Hutchinson and Hutchinson [82].

LASAT method provides a robust methodology to obtain a clear ranking of adhesion of coating systems manufactured by a given processing method. It has been established that the ranking obtained in the as-processed condition for EB-PVD YSZ coating is consistent with both life to spallation under thermal cycling and ranking established after thermal cycling before spallation [72]. The major advantages of this method are to be a non-contact method, limiting the bias induced by specimen preparation, and to be fairly robust as compared to classical TAT [186]. Whereas the dynamic range of loading prevents from a direct interpretation of the obtained interfacial properties in quasi-static range, the measured dynamic toughness and its evolution with aging is in agreement with any other known mechanical measurement of adherence. Moreover, the notch like defect processed by LASAT and combined to the non-destructive evaluation of the resulting blister (IRT or optical image analysis and profilometry) has been successfully used to capture interfacial toughness evolution with aging [186, 110].

### 1.3.5 Advanced 3D characterization of microstructure morphology and cracks

The microstructure of protective coatings plays an important role in initiation and propagation of cracks and final failure by spallation. In a TBC system cracks may initiate either within the different layers or at the interfaces between the layers. Depending on local stresses and morphology of the microstructure, cracks propagate leading to coating failure by spallation. Damage and failure mechanisms of TBC systems have been widely investigated mainly based on observation of cross sections processed by saw or wire-cutting [57]. Such cross sections provide two dimensional (2D) data about crack initiation sites and crack paths. However, the precise 3D information of the microstructure and the size and location of cracks especially at the interfacial regions of the layers has to be addressed since the size and morphology of the so-called process zone of a crack modifies the available strain energy density for final buckling and subsequent spallation [215].

In materials science, emerging 3D techniques are now widely spread for microstructure characterization and available for application on TBC systems. As a nondestructive method X-ray computed tomography (CT) appears as an attractive method for evaluating TBC systems, but some limitations depending on the X-ray source and the imaging technique have to be considered. In general, the scanned volume and the resolution are reciprocal. Therefore, for achieving high resolution the CT is limited to small volumes. For investigating EB-PVD or APS TBC samples applied on a Ni based substrate rods of less than 500  $\mu\text{m}$  in diameter achieved an apparent resolution of about 0.9  $\mu\text{m}$  voxel size [93, 1]. Computed laminography (CL), which is similar to CT but with a different X-ray beam angle to the rotational axis of the specimen ( $90^\circ$  for CT and typically  $60^\circ$  for CL), enables analyzing a plate with an in-plane extension in the centimeter range [122]. Applied to TBC, CL has provided 3D measurement of progressive damage evolution with thermal cycling [113]. CT and CL have a limited spatial resolution of about 500 nm for CT and few  $\mu\text{m}$  for CL, respectively. As an alternative for achieving high resolution 3D reconstructions, focused ion beam (FIB) serial sectioning coupled with scanning electron microscopy (SEM) can be used. Although this method is destructive, it is relatively gentle and even brittle and weakly bonded materials such as the TGO on bare oxidized alloys are preserved [52]. After 3D reconstruction, the spatial resolution is in the range of about 2 - 20 nm, depending on the distance between the FIB slices. Thus, the FIB-SEM 3D serial sectioning tomography is an attractive method for studying 3D details of the morphology of TBCs.

Recently, results of FIB-SEM 3D serial sectioning tomography on EB-PVD TBC systems have been published. In [71], results from FIB-SEM serial sectioning have been compared to such achieved by CT using different X-ray sources. Besides some pore size distribution analysis of the BC and the diffusion zone between substrate and BC, the 3D representations have been qualitatively compared with 2D SEM images. The work of Dennstedt et al. [48] focuses on the FIB-SEM serial sectioning method and provides quantitative approaches to describe the path of complex delamination cracks. One precondition was a good segmentation between the layers and cracks by using two different detectors for imaging by SEM, the electron backscatter detector and the secondary electron detector, which provide images with complementary contrast information, compare Fig. 1.19(a) to (c). By analyzing further the area fraction of each phase detected in sections parallel to the coating plane, quantitative data to describing the crack path were derived.

## 1.4 Properties of protective coating systems

The following tables present successively the thermal conductivity, the coefficient of thermal expansion, the Young's modulus, and interfacial toughness for different TBC materials and their respective evolution as a function of temperature. The experimental techniques of characterization are indicated when not usual. Precision is given if micro-testing is used, instead of standard specimen.

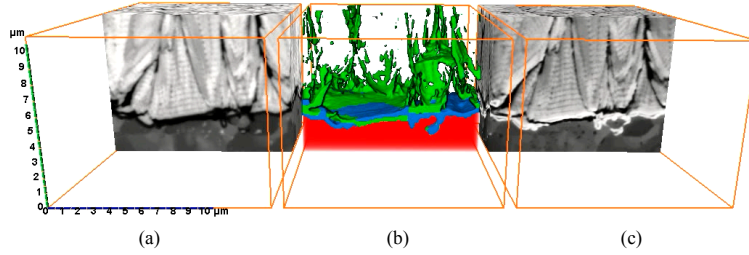


Figure 1.19: Reconstructed volume from FIB-SEM serial sectioning (Box size:  $11 \mu\text{m} \times 14.2 \mu\text{m} \times 18.88 \mu\text{m}$ ). Segmentation of the different phases BC, TGO, TC, and cracks or voids was performed by using images from Backscatter Electron (a) and Secondary Electron (c) detectors. In (b), the BC is displayed in red, the TGO in blue, cracks, respective voids in green, and the TC transparent to allow for viewing the structure of inter-columnar gaps (courtesy of A. Dennstedt).

The data are given for only few temperatures, ignored when not available and are interpolated when measurements are close to these temperatures.

Table 1.1: Thermal conductivity,  $k$  (W/ (m·K))

Layer	T (°C)						Ref.
	RT	600	800	900	1000	1100	
<b>TC</b>							
<i>EB-PVD</i>						<i>flash 1316 °C / 1.8</i>	[90]
<i>EB-PVD (as received heating up)</i>	1.4	1.2	1.2	1.3	1.3	1.3	[148]
<i>EB-PVD (as received cooling)</i>	1.6	1.4	1.4	1.4	1.4	1.4	[148]
<i>EB-PVD (200 h 1100 °C)</i>	2.1	1.6	1.6	1.6	1.5	1.5	[148]
<i>EB-PVD</i>	1.6	1.4	1.6	1.3	1.4	1.3	[18]
<i>APS (as received heating up)</i>	0.7	0.6	0.6	0.6	0.6	0.7	[148]
<i>APS (as received cooling)</i>	0.8	0.7	0.7	0.6	0.7	0.7	[148]
<i>APS (200 h 1100 °C)</i>	1.4	1.2	1.0	1.0	0.9	0.9	[148]
<i>SPPS</i>						<i>flash 1316 °C / 0.62</i>	[90]
<i>SPS (columnar)</i>	0.8	1.	0.9	0.9	0.8	0.9	[18]
<i>SPS (compact)</i>	0.7	0.7	0.8	0.7	0.7	0.6	[18]
<b>TGO</b>	33				6.7		[190]
<b>BC</b>							
<i>NiCoCrAlY</i>	10.8				32.1		[190]
<b>Substrate</b>							
<i>CMSX4</i>						31.0	[16]

Table 1.2: Coefficient of thermal expansion,  $CTE$  ( $10^{-6} \text{ K}^{-1}$ )

Layer	T ( $^{\circ}\text{C}$ )						Ref.
	RT	600	800	900	1000	1100	
<b>TC</b>							
<i>EB-PVD</i>	9.0	10.1	10.8		11.7	12.2	[200, 80] cited in [36]
<b>TGO</b>	8.0	8.7	9.0		9.3	9.6	[200, 80] cited in [36]
<b>BC</b>							
<i>(Ni,Pt)Al</i>	13.6	15.2	16.1		17.2	17.6	[164, 168] cited in [36]
<i>NiCoCrAlY</i>	10.0				17.5		[190]
<i>NiCoCrAlYTd</i>	15.1	15.1	17.9	22.0			[181]
<b>Substrate</b>							
<i>AM1</i>	8.0	13.0	14.0		15.4		[75]
<i>CMSX4</i>						16.2	[16]
<i>PWA1480</i>	14.8	16.2	16.9		17.5	18.0	[127] cited in [36]

## 1.5. EVOLUTION OF TBC MICROSTRUCTURE AND ASSOCIATED DAMAGE UNDER THERMAL AND THERMO-

In table 1.3 the average in-plane Young's modulus is given for the coatings. Gradients across the coating thickness, as observed for EB-PVD-TC layers are not considered. The elastic response of cubic single crystalline materials is described by a stiffness matrix with three independent constants. For comparison reasons, the Young's modulus in  $[001]$  direction is given.

Table 1.3: Young's Modulus (GPa); FS indicates free standing coating testing

Layer	T (°C)						Ref.
	RT	600	800	900	1000	1100	
<b>TC</b>							
<i>EB-PVD</i>	48	40	34		26	22	[200, 80] cited in [36]
<i>APS</i>	65-110						[66]
<b>TGO</b>	400	370	355		325	320	[200, 80] cited in [36]
<b>BC</b>							
<i>(Ni,Pt)Al</i>	200	160	145		120	110	[164, 168] cited in [36]
(FS)			55	35	15		[182]
(FS)	135			110 (*)			[4]
$\gamma - \gamma'$ (FS)	130			127 (*)			[4]
				(*) 870 °C			
<i>NiCoCrAlY</i>	200				120		[190]
<i>NiCoCrAlYTaN</i> (FS)	182	157	141	128	105		[180]
<b>Substrate</b>							
<i>AM1 ([001] direction)</i>	137		108		104		[30, 75]
<i>CMSX4 ([001] direction)</i>	127	106	95	90	82		[163]
<i>PWA1480</i>	220	170	155		130	120	[127] cited in [36]

## 1.5 Evolution of TBC microstructure and associated damage under thermal and thermo-mechanical loads

### 1.5.1 Thermal fatigue/cyclic oxidation testing

The most standard testing configuration for TBC lifetime evaluation consists in a cyclic oxidation test. Standard specimens are button shape coupons (one inch diameter and 1-3 mm thickness) which are chamfered on one edge. The BC is applied all over the specimen, whereas the TC is deposited only on the side with the chamfered edge, to decrease detrimental edge effect. As a standard, electrical furnace is used to prescribe the maximum temperature, the specimens being moved into and out of the furnace for heating and cooling. The applied thermal cycling consists for most of the studies in a direct heating in the furnace,

Table 1.4: Interfacial toughness evaluation for different testing and analysis methodology

System/Testing technique	Analysis	Mixity angle (°)	Aging	Gc (J/m <sup>2</sup> )
<b>TC</b>				
<i>APS/NiCoCrAlY</i> compression	FEA	-56	no	110-130
<i>EB-PVD/CoNiCrAlY</i> push-out/shear	analytical	-90	isothermal 1150 °C	120 (hox=2 μm) 20 (hox=4.5 μm)
<i>EB-PVD/NiCoCrAlY</i> bending	FEA	20	no	57±21
4-point bending	analytical	20	no	81
		20	1000 °C 100 h	63
		20	1100 °C 10 h	37
<i>EB-PVD/(Ni,Pt)Al</i> 4-point bending	analytical	20	no	110
	FEA	20 and 70	FCT 250 cycles (*)	G0/3±3G0 (**)
LASAT	analytical	0	FCT 300 cycles (*)	5
<b>TGO</b> 4-point bending	analytical			110

(\*) FCT RT - 1100 °C with 1h per cycle; (\*\*) only relative values are available.

## 1.5. EVOLUTION OF TBC MICROSTRUCTURE AND ASSOCIATED DAMAGE UNDER THERMAL AND THE

45-60 minutes dwell at maximum temperature for aero-engine application (could be extended to 24 h and more for reproducing working cycles of stationary gas turbines for energy conversion) and natural or air-assisted cooling. For reducing the time of the cooling sequence, the target minimum temperature could be set for instance to 100-200 °C without strong impact in damage evolution [188].

As a major result of this thermal cycle, the CTE mismatch between each material constitutive of the TBC system (substrate, IDZ, BC, TGO, TC) induces high stresses in each layer which result in crack initiation and subsequent interfacial damage and finally spallation as described in paragraph 1.5.3. A thermal cycle can be regarded as representative for a thermo-mechanical fatigue cycle with temperature and mechanical load cycle out-of-phase (OP-cycle). The effect of cyclic thermal loading, which mimic more closely than isothermal loading the in-service condition of an aero-engine has been systematically investigated in [40]. By varying the dwell time in thermal cycling experiments but keeping the overall time at high temperature the same, it was found that microstructure and damage evolution increase significantly with decreasing the dwell time or with other words with increasing the frequency of thermal cycling. Comparison with isothermal oxidation highlights both the detrimental effect of short dwell time in thermal cycling and the modification of damage mechanism [213, 40].

### 1.5.2 BC and TGO evolution under thermal cycling

Firstly, together with high temperature exposure TGO growth induces strain growth associated to molar volume difference of the newly formed oxide as compared to the metallic BC [187]. In addition to TGO growth, diffusion takes place. Mainly, an outward flux of Al, to form the TGO, and an inward flux of Al from the BC to the substrate should be considered. Reciprocally, a Ni flux from the substrate to the BC is observed. These diffusion processes yield phase transformation from  $\beta$ -NiAl to  $\gamma'$ -Ni<sub>3</sub>Al in the case of NiAl diffusion coating, Figure 1.20(a) and (b). For MCrAlY coating, phases evolve from  $\beta + \gamma + \alpha$  to  $\beta + \gamma' + \alpha + \sigma$  or from  $\beta + \gamma$  to  $\beta + \gamma'$  for low Cr and Co compositions, Figure 1.20(e) [124]. For  $\beta$ -NiAl diffusion coating, the martensitic transformation from B2 to L1<sub>0</sub> structure from high to low temperature has been evidenced [34].

For bare metallic coating, net mass gain (NMG) measurements under thermal cycling shows i) pure gain of mass due to BC oxidation, ii) decrease of NMG rate due to partial oxide spallation leading sometimes to a plateau (equilibrium of mass gain by oxidation and mass loss by oxide spallation), iii) decrease of NMG due to an excess of loss as compared to gain, and iv) catastrophic loss and final breakaway. In this case, the oxide spallation is mostly driven by BC/TGO failure, and the apparent adherence of the oxide decreases with aging under thermal cycling. The testing methodology being detailed in section 1.7.1.

For bare BC (i.e. without ceramic TC), the TGO could spall off from the BC when reaching high thickness and/or more likely reaching a critical interfacial fracture toughness, which leads to spallation during cooling when the stress intensity is the highest. Local discontinuities such as thickness variation of the TGO are increasing local stresses and enhancing the damage process [58].

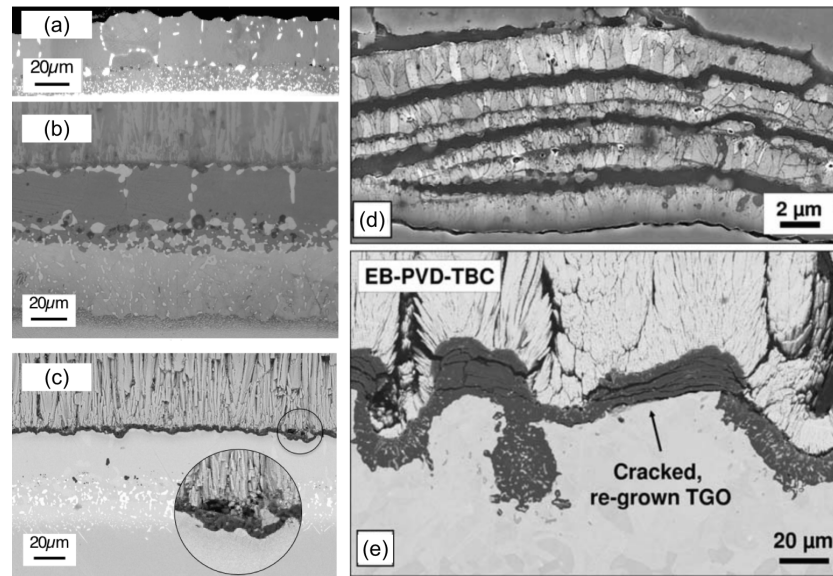


Figure 1.20: Evolution of TGO microstructure for thermal cycling (range 100–1100 °C) for (Ni,Pt)Al BC, (a) after 1000 cycles without TC observed by optical microscope (OM) (adapted from [155]), (b) with EB-PVD TC for N=1200 cycles observed by SEM in BSE mode, (c) SEM image of TBC system from (b) in SE mode (insert corresponds to a zoom of the black circle) (adapted from [113]) and for NiCoCrAlY BC, (d) SEM image in SE mode of oxide fragmentation of a system with APS TC (maximum cycle temperature 1050 °C) and (e) SEM image in SE mode of a system with EB-PVD TC (maximum cycle temperature of 1000 °C) (adapted from [124])

For improved adhesion of the TGO, as obtained by Pt addition to NiAl, large undulation of the TGO and BC are observed under thermal cycling, with the amplitude of the undulation increasing by the number of cycles. This deformation mechanism is called rumpling. Some authors have claimed that rumpling was induced by either martensitic or  $\beta$  to  $\gamma'$  phase transformation [34]. However, when limiting the partial pressure of  $O_2$  and consequently the TGO growth without substantial modification of phase transformation, the rumpling was drastically limited [189, 109]. Thus, the dominating mechanism of rumpling is the combination of the increase of the TGO volume (and subsequent oxide strain growth) and the low mechanical properties of the BC at the TGO temperature formation. For highly adherent TGO, the oxide growth induces large creep deformation in the BC at high temperature, and for thermal cycling, cumulated plastic straining is likely to amplify the undulation.

### 1.5.3 TBC evolution under thermal cycling

In the case of a complete TBC system (including ceramic TC), the TGO spallation is confined by the TC and when further exposed to high temperature strain accumulation can induce local TGO cracking without spallation, Figure 1.20(d) and (e). Subsequently, much higher TGO thickness could be observed for adherent TC as compared to bare BC, making the critical thickness of TGO non obvious.

The role of TC in rumpling could be clearly illustrated by introducing an interfacial defect by laser shock before thermal cycling (based on the non contacting LASAT method described in section 1.3.4). After furnace thermal cycling, three different subsequent morphologies could be observed on a cross-section: i) along the initial debonding introduced by laser shock the rumpling is very pronounced as usually observed for bare BC, Figure 1.21(a) and (c); ii) "far away" from initial debonded area, no rumpling is observed, but interfacial damage is consistent with damage observed without artificial defect, compare Figures 1.21(b), and 1.20(c) and iii) at the transition between large debonding and adherent TC, corresponding to interfacial crack tip, it is observed beginning of large undulation as compared to damage without rumpling, Figure 1.21(d).

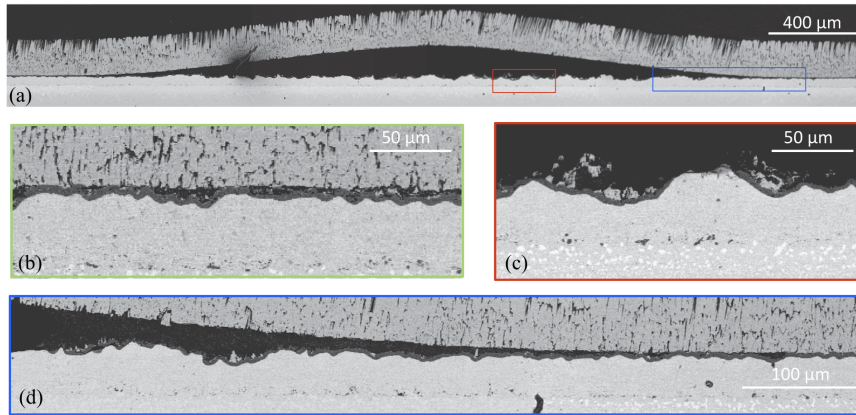


Figure 1.21: Interfacial defect introduced by LASAT in the as-processed condition and observed after 2000 thermal cycles at 1100 °C, (a) global view of the blister, (b) detail view out of (a): interface evolution without interaction with the initial defect, (c) detail view, see red rectangle in (a): initial area of decohesion, (d) detail view, see blue rectangle in (a): evolution in the vicinity of the interfacial crack tip (courtesy of Lara Mahfouz)

Even though the driving forces for rumpling are present for adherent TC, this example demonstrates that without TC decohesion, no rumpling can take

place. Except for TGO growth and rumpling, the microstructure evolution of (Ni,Pt)Al BC is very similar with or without EB-PVD TC layer for both the evolution of the  $\beta$  to  $\gamma'$  phase transformation in the external BC layer and for IDZ evolution, Figure 1.20(a) and (b).

When exposed to high temperature, sintering is the main process acting on the TC microstructure to induce an evolution of the mechanical properties and in particular an increase of the TC stiffness [102]. The crucial role of CMAS on the change of TC during service will be highlighted in section 1.6.

For complete TBC including an EB-PVD TC layer, failure yields the final spallation of the TC: spallation is observed on disk shape specimens, Figure 1.22(a) and for the same duration and aging condition, both the critical strain of TC failure, Figure 1.22(b) and the apparent interfacial toughness, Figure 1.22(c) are observed to decrease. The testing methodology is detailed in section 1.3.4. It has been shown that either the BC/TGO or the TGO/TC interfaces could be the weak interfaces: for isothermal aging and/or low adhesion of the TGO the BC/TGO damage drives final failure, whereas for thermal cycling and/or high adhesion of the TGO, the TGO/TC damage dominates final failure, see Figure 1.21(b) and (d), and refs. [213, 40].

Recent investigations of  $\gamma - \gamma'$  Pt-rich coating during thermal cycling highlights the improvement in lifetime as compared to classical  $\beta$ -(Ni,Pt)Al BC for the same substrate. However, the authors have demonstrated that the critical interface is the BC/TGO interface, where the TGO develops on a  $\gamma$  layer after aging [6].

## 1.5. EVOLUTION OF TBC MICROSTRUCTURE AND ASSOCIATED DAMAGE UNDER THERMAL AND THE

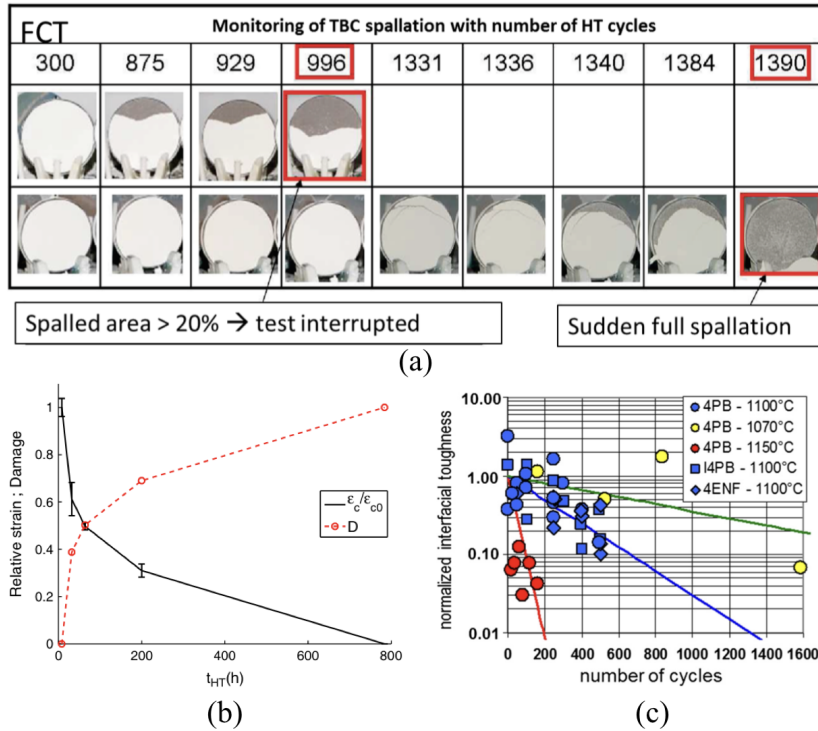


Figure 1.22: Effect of thermal furnace cycling for EB-PVD, (Ni,Pt)Al bond-coat and first generation single crystal superalloy. (a) Appearance of TBC spallation observed on button shape specimens as a function of cycle number, [60], (b) evolution of critical strain,  $\epsilon_c$ , at spallation and associated damage,  $D$ , as a function of the time spent at high temperature (adapted from [40]), and (c) interfacial toughness as a function of the number of furnace cycles and temperature [195]

### 1.5.4 Damage evolution and lifetime behavior evaluation under mechanical and thermal loading (LCF, TMF, TGMF, and burner rig)

Coated high pressure turbine blades face high mechanical and thermal fatigue loading induced by the expanding hot gas, the transient temperature differences between heated outer surface and cooling channel walls, and additional centrifugal forces in the case of rotating blades. The loading conditions are quite complex and just thermal cycling of coated specimens under laboratory conditions is not sufficient to replicate the damage processes occurring in coated turbine blades during gas turbine operating cycles. However, realistic testing in laboratory is difficult to conduct and appropriate test facilities are extremely

expensive. Therefore, simplified tests were developed aiming at either ranking of new coatings variants during material development campaigns or at better understanding of damage mechanisms under controlled loading conditions.

Low cycle fatigue (LCF) testing is straightforward to assess the influence of mechanical loads under isothermal conditions on the damage behaviour and lifetime of a coated material system. To achieve a stable temperature over the entire test, usually resistance furnaces with a high thermal inertia are used for heating the specimen. It has been observed that under LCF conditions cracks are typically induced at morphological instabilities at the surface, see Figure 1.23(a), or at the interface between BC-TC [14] or between substrate-BC, see Figure 1.23(b). The coating could be either beneficial or detrimental depending mainly on substrate composition and type of coating [145]. This point was seen to be crucial for 3rd and higher generation of single crystal superalloys for which diffusion (Ni,Pt)Al coating was observed to induce secondary reaction zone (SRZ) and drastic decrease of the LCF lifetime [37, 31], see also details in chapter ??.

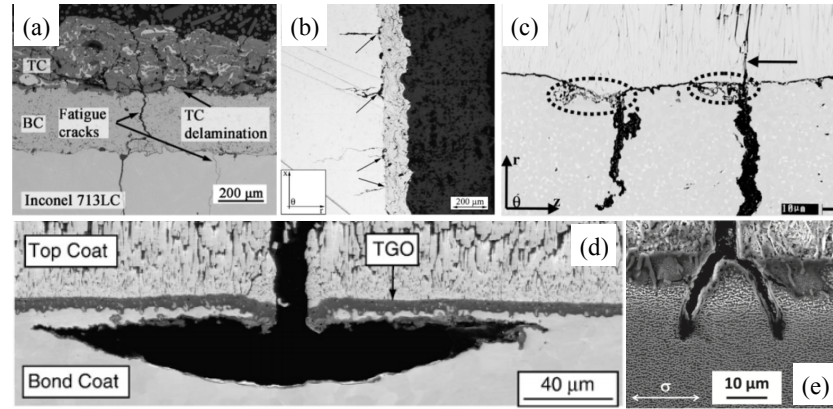


Figure 1.23: Exemplary damages observed under different thermal and mechanical testing conditions, (a) APS BC and TC after LCF test with  $R_\epsilon=-1$  [173], (b) APS BC only, LC after LCF test with  $R_\epsilon=-1$ , and  $T=850\text{ }^\circ\text{C}$  [88] (c) EB-PVD TC and APS BC, IP-TMF test:  $R_\epsilon=0$ ,  $\epsilon_a=0.7\%$  and  $100;T;1000\text{ }^\circ\text{C}$  [190] (d) IP-TGMF test:  $R_\sigma=0$ ,  $\sigma_a=100\text{ MPa}$  and  $100;T;1000\text{ }^\circ\text{C}$  with  $\Delta T=170\text{ }^\circ\text{C}$  (through thickness)[77], (e) Coating system after burner rig test in combustion environment, OP-TGMF test:  $R_\sigma=0$ ,  $\sigma_a=800\text{ MPa}$  and  $500;T;1100\text{ }^\circ\text{C}$  with  $\Delta T=150\text{ }^\circ\text{C}$  (surface) and  $\Delta T=50-70\text{ }^\circ\text{C}$  (through thickness) [106]

The effect of strain dwell under high temperature condition, evaluated in so-called Sustained Peak LCF, was also seen to be crucial in impact on TBC lifetime. This was described to be associated to a mechanism where, in addition to early cracking induced by the TBC, the stress relaxation at high temperature yields tensile stress at zero strain and increases dramatically the fatigue crack

## 1.5. EVOLUTION OF TBC MICROSTRUCTURE AND ASSOCIATED DAMAGE UNDER THERMAL AND THE

growth rate [55]. However, it is worth noting that under LCF condition the driving force for additional damage induced by the TBC is mainly associated to creep of the coating [219].

To get closer to in-service loading, thermal and mechanical cycling is combined with thermal mechanical fatigue (TMF). Thermal cycles are typically applied by means of induction heating, which allows frequencies in the range of minutes instead of hours as in the case of using resistance furnaces. Usually, in-phase (IP) cycling (maximum temperature and tensile loading are synchronous) and out-of-phase (OP) cycling (maximum temperature and compressive loading are synchronous) are distinguished, but any other phase shift between thermal and mechanical cycle can be applied. For bare BC, it has been observed that phase transformation and rumpling was increased in TMF as compared to pure thermal cycling for both IP and OP conditions [156]. It has been observed that rumpling under IP TMF results in wrinkles oriented along the mechanical loading direction [11]. In presence of the ceramic TC layer, it is currently observed that the time to TC spallation is reduced in OP as compared to IP, and that detrimental effects of oxidation and cracking are enhanced under TMF condition, see Figure 1.23(c) and (d) [190, 63].

More realistic than TMF with homogenous temperature across the cross section of the test specimen are experiments replicating the thermal gradient experienced by the turbine blade, the so called Thermal Gradient Mechanical Fatigue (TGMF) tests. Firstly, one should notice that the TC surface is the hottest part of the component, particularly for hollow blades where internal cooling decreases the substrate temperature. Therefore, in TGMF testing of coated specimens the substrate side has to be cooled and the TC surface has to be heated. No induction heating can be applied, since the electrically conductive substrate is heated, which results in a biased thermal gradient across the coating system, even if the substrate is cooled. In TGMF testing tubular specimens are used with internal air cooling through a central cooling channel and heating the outer surface by a radiation furnace. For achieving a realistic thermal gradient over the specimen wall, TGMF facilities with a focusing radiation furnace have been developed at the German Aerospace Center [15, 13]. The experiments described in [13] were conducted on coated specimens comprising directionally solidified Ni-base superalloy IN 100 as substrate, NiCoCrAlY BC, and YSZ TC, both coatings applied by EB-PVD. The maximum specimen surface temperature in each TGMF cycle was 1000 °C, and over the specimen wall a maximum temperature difference of 170 °C was achieved. The load cycle was designed to represent the fatigue load at the leading edge of a rotating turbine blade during an entire flight mission of an aero-engine. Compared to thermal cycling experiments with the same maximal temperature a premature spallation of the coating system was observed. The damage feature after TGMF testing differed significantly from that after thermal cycling. After thermal cycling the TC spalled off with adherent TGO (so called black failure) without crack formation perpendicular to the coating plane. In contrast, crack initiation in TGMF started in the TGO under tensile stress creating cracks perpendicular to the coating plane and the applied mechanical load. During propagation into the BC cracks deviated

within the BC with the crack path parallel to the interface BC and TGO and changing finally to the Interface between BC and TGO. Multiple cracks evolved simultaneous and merged leading to large scale spallation. At the location of crack initiation inelastic deformation of the BC occurred forming a smiley crack feature, Figure 1.23(e). Further mechanical experiments on the same type of coated specimens were performed with a compact radiation furnace in situ in a synchrotron facility [95, 105] in order to observe the deformation behaviour of each coating layer during mechanical loading. With these results, it was possible to explain the damage behaviour in TGMF testing and to validate predictive simulation models, which captured the observed behaviour [78, 77].

Another approach to apply thermal gradients is based on burner rig facilities, where a flame (most of facility using natural gas) is heating the coated side, and the substrate side is cooled by pressurized air. These facilities are very convenient to test also the impact of mineral particles which are ingested into the aero engine from the environment, such as oxides and silicates. With a burner rig facility developed at the Research Centre Jlich a temperature difference across a coated disc shaped specimen of about 200 °C was achieved with a maximum temperature of 1200-1300 °C at the TC surface [103], Figure 1.24(b). However, most burner rig facilities are not capable to apply mechanical loads.

Only few test rigs are developed, which allow simultaneous mechanical loading combined with a burner rig heating system. One example is the MAATRE burner rig facility [106] in which a specimen can be loaded by means of a servo-hydraulic fatigue testing machine in a realistic combustion environment using a kerosene burner. The hot gas flow is perpendicular to the length axis of a tubular specimen, which results in different conditions at the leading and trailing edges. Test results on coated specimens revealed severe damage by multiple cracking of the coating with cracks propagating into the substrate, to higher extend at the trailing edge compared to the leading edge, Figure 1.23(c)[106].

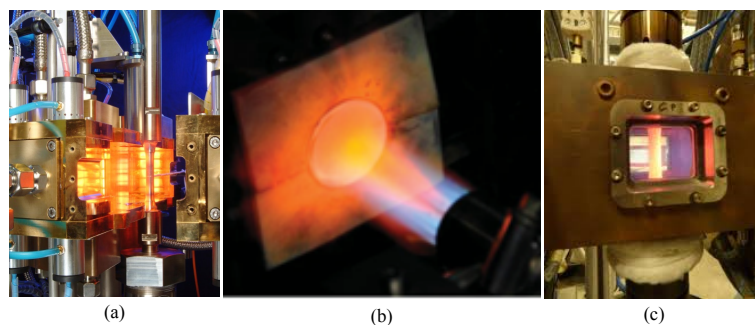


Figure 1.24: TGMF testing of TBC in presence of gradient (a) TGGMF [13], (b) Burner rig [103] and (c) Combustion environment in TGGMF condition [106]

## 1.6 Challenges due to ingested mineral particles CMAS

### 1.6.1 Damage mechanisms and TBC degradation due to CMAS attack

Recent enhancement of aircraft performances due to increased turbine inlet temperature has in return generated new and even more critical premature failures of TBC (8YPSZ) that affect their lifetime. In particular, severe degradation is due to mineral particles (sand, dust, volcanic ashes, etc.) ingested with intake air, which subsequently adhere to the hot section components (combustor, high pressure turbine blades and vanes, shrouds) as siliceous deposits [166, 21].

These deposits are mainly constituted of CaO, MgO, Al<sub>2</sub>O<sub>3</sub> and SiO<sub>2</sub> (CMAS) but also contain other metallic oxides (Fe<sub>2</sub>O<sub>3</sub>, NiO and TiO<sub>2</sub>), sometimes in large amounts. CMAS composition strongly depends on flight location [21, 196, 166, 22], resulting in various viscosities and melting temperatures [140]. With the increase in operating temperature, TBC surface temperature during service (1200 °C or higher) exceeds most of CMAS deposits melting points. Thus, CMAS melts and infiltrates very rapidly, through capillary action, the TBC open porosity (inter-columnar gaps in the case of EB-PVD coatings), leading to TBC stiffening and loss of its strain tolerance. As a result, delamination cracks can develop in the infiltrated TBC during cooling, leading to progressive spallation with engine thermal cycling [116, 96, 101]. Chemical degradation is also observed with the dissolution of yttria-stabilized zirconia during interaction with silicate melt, followed by re-precipitation of YSZ with a modified composition and morphology depending on the melt chemistry [98, 7, 51, 115, 196, 101, 197]. These two mechanisms are schematically summarized in Figure 1.25. The thermomechanical degradation mode is considered to be predominant compared to the thermochemical one. Thus, with the higher operating temperatures, CMAS-induced TBC degradation has become increasingly critical making it necessary to find alternate TBC compositions as well as coating morphologies likely to limit CMAS infiltration.

### 1.6.2 CMAS resistant compositions for ceramic coatings

The most recent CMAS mitigation strategies rely on the chemical reactivity (dissolution/reprecipitation process) between TBC and CMAS melt. It consists in modifying TBC composition to promote crystallization of phases that will arrests the CMAS front. Two kinds of alternate TBC have been proposed: in the first one, rather applicable to APS or SPPS coatings, Al<sub>2</sub>O<sub>3</sub> and TiO<sub>2</sub> are incorporated in metastable solid solution in YSZ. During TBC dissolution, alumina combines with CaO and SiO<sub>2</sub> from the melt, resulting in the near-complete CMAS crystallization into anorthite (CaAl<sub>2</sub>Si<sub>2</sub>O<sub>8</sub>) [7, 51, 101]. The second one is based on rare-earth zirconates (RE<sub>2</sub>Zr<sub>2</sub>O<sub>7</sub>, RE= from La to Yb). Indeed, its dissolution in the CMAS melt leads to the near-simultaneous precipitation

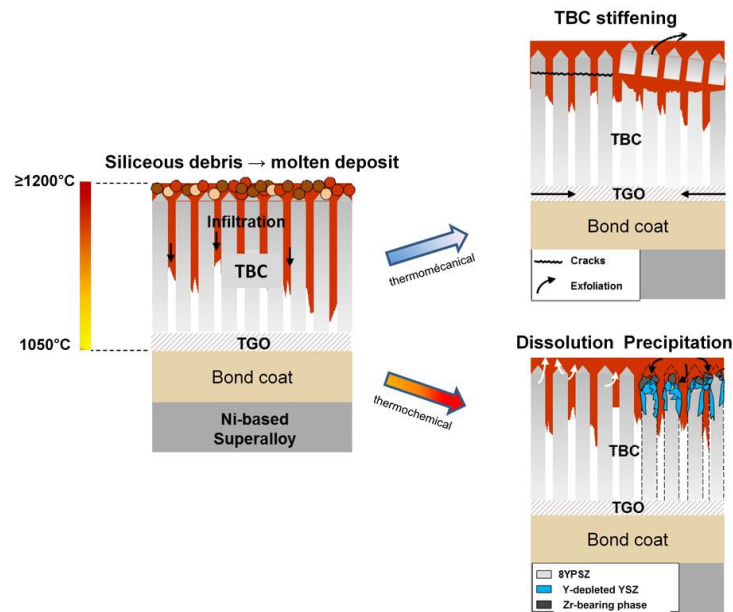


Figure 1.25: CMAS- induced degradation mechanisms of EB-PVD thermal barrier coatings

of a  $Zr(RE, Ca)O_x$  phase and a  $Ca_2RE_8(SiO_4)_6O_2$  apatite silicate. In the case of EB-PVD coatings, these two phases fill the TBC intercolumnar gaps, thus blocking further CMAS penetration. The effectiveness of this last strategy has been first demonstrated for  $Gd_2Zr_2O_7$  (Figure 1.26) [97, 101].

### 1.6.3 Characterization of damages by CMAS attack

First investigations have consisted in performing microstructural analysis of CMAS-induced coating degradation on hot section components from the field [166, 21, 116, 96, 22, 196, 206]. Such studies are infrequent as they use destructive methods and that engine parts are not easily available. They have provided very significant source data on CMAS infiltration depth in the TBC, CMAS deposits composition and distribution at the surface of the components. They have also identified failure mechanisms, as delamination cracks within or below the infiltrated TBC as well as chemical reaction between 8YPSZ coating and CMAS. Subsequently, simple laboratory furnace tests have been developed, aiming to reproduce the chemical interaction taking place in service [119, 51, 205, 209, 144, 197, 123, 98, 171, 7]. They are performed in isothermal controlled conditions at temperatures varying from 1100 °C to 1400 °C, without thermal gradient in the TBC. In order to eliminate premature TBC spalling during cooling, or degradation of superalloy mechanical properties at temper-

## 1.6. CHALLENGES DUE TO INGESTED MINERAL PARTICLES CMASXLVII

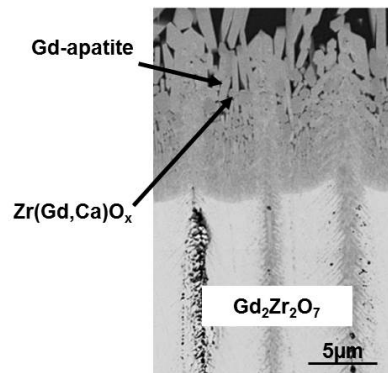


Figure 1.26: SEM micrograph showing the sealing of the intercolumnar gaps of an EB-PVD  $Gd_2Zr_2O_7$  coating by the combination of Gd-apatite and  $Zr(Gd,Ca)O_x$  crystalline phases (based on information from [101])

atures above 1200 °C, TBC system samples (TBC coating on bond-coated superalloy substrate) are not used but rather simplified TBC material: ceramic pellets (dense or porous), free standing coatings or deposited on alumina substrate (Figure 1.27). Due to the numerous oxides contained in CMAS deposit compositions, model CMAS (containing three to five oxides among  $SiO_2$ - $CaO$ - $Al_2O_3$ - $MgO$ - $Fe_2O_3$ ) are generally used. A classic composition is 33CaO-9MgO-13AlO<sub>1.5</sub>-45SiO<sub>2</sub> [98]. However, tests using sand or volcanic ashes, synthetic or sampled from the field, are also reported [68, 115, 50, 44]. CMAS (powders or plate) is deposited on top of the TBC specimen, and the assembly is heat treated in a furnace for different durations. Though such tests are not representative of the actual engine conditions, the chemical interaction mechanisms are similar to that observed using thermal-gradient tests. The understanding of 8YPSZ/CMAS interaction as well as the development of alternate coatings resulted from such tests. Mixtures of TBC and CMAS powders are also used. Either with a high ceramic concentration, required for identifying reaction products by X-ray diffraction; or with much lower ceramic concentration, for studies devoted to obtain thermodynamic or kinetic information on these reactions [139, 132, 99].

In the case of TBC coatings, such isothermal tests also provide CMAS penetration depth data and can be used to compare the effectiveness of various alternate TBC compositions or coatings morphology in limiting CMAS infiltration. X-ray elemental mapping (Si or Ca) is usually performed on coating cross-sections to determine CMAS infiltration depth (Figure 1.27).

Concerning experimental characterization of TBC failure mechanisms and evaluation of its lifetime under CMAS attack, isothermal furnace cycle tests have hardly been used as they are too harsh, leading to underestimation of TBC performance, and temperature limited because of the superalloy. Thermal

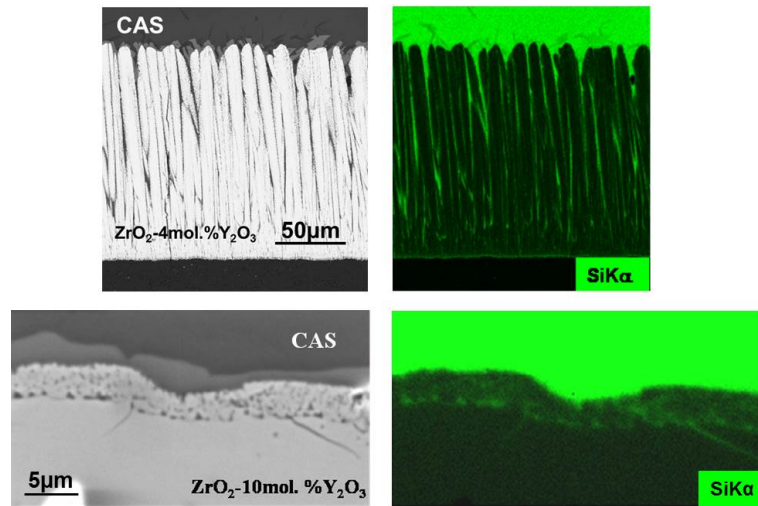


Figure 1.27: Cross-sectional SEM micrographs of YSZ EB-PVD coating (top) or dense pellet (bottom) infiltrated by a model CAS melt, and corresponding Si elemental map showing CAS penetration (light contrast)

gradient cycling tests with simultaneous CMAS injection, first performed in 2010 in the case of plasma-sprayed coatings [170, 49], are much more relevant but more difficult to develop. The heat source is either a combustion flame (burner rig) [49, 170, 103], or a continuous CO<sub>2</sub> laser [101, 85, 84]. In the case of the burner rig, the CMAS is prepared as an aqueous solution of nitrates or a dispersion of CMAS-frit in water, and is sprayed into the flame. With the laser, CMAS is pre-deposited on the TBC surface. Such experiments are often analyzed using thermo-mechanical models adapted or extended from those previously developed for TBC failure mechanisms in the absence of CMAS [56, 101, 83, 85].

#### 1.6.4 Thermal cycling behaviour in presence of CMAS

The mechanism generally adopted to describe TBC failure due to CMAS infiltration is a cold shock delamination taking place during engine shutdown and resulting from TBC densification [116]. Indeed, subsurface delamination cracks within or under infiltrated regions of the TBC are observed on ex-service turbine airfoils (Figure 1.28). They always emanate from surface-connected vertical separations, already existing after elaboration or emerging in service due to sintering or tensile stresses induced upon rapid cooling. The driving force for such TBC delamination and spalling is the release of the elastic strain energy stored in the coating upon cooling, due to the thermal expansion mismatch between the coating and the metal substrate. This elastic energy highly depends on the

### 1.6. CHALLENGES DUE TO INGESTED MINERAL PARTICLES CMASXLIX

initial thermal gradient in the TBC coating and is very sensitive to the engine cooling conditions. In particular, slow cooling prevents from the development of vertical separations in the TBC [116, 56, 101, 83, 140]. The CMAS infiltration depth in the coating is also of major importance [101, 85]. Indeed, the higher the CMAS penetration depth, the higher the increase in TBC Young's modulus, resulting in a substantial increase in the elastic energy, and thus in the delamination propensity (Figure 1.29).

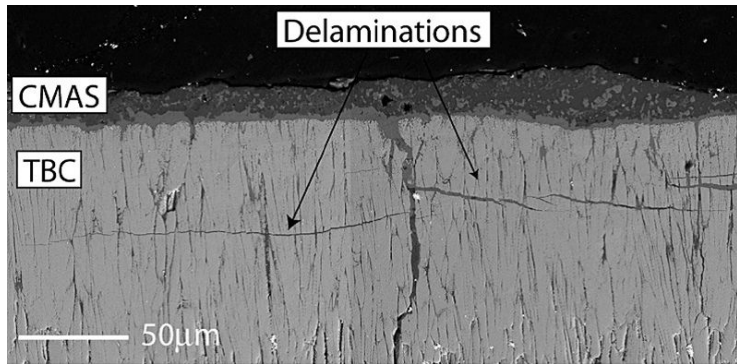


Figure 1.28: SEM micrograph on an EB-PVD 8YPSZ cross-section with delamination cracks emanating from surface-connected vertical separations (based on information from [116])

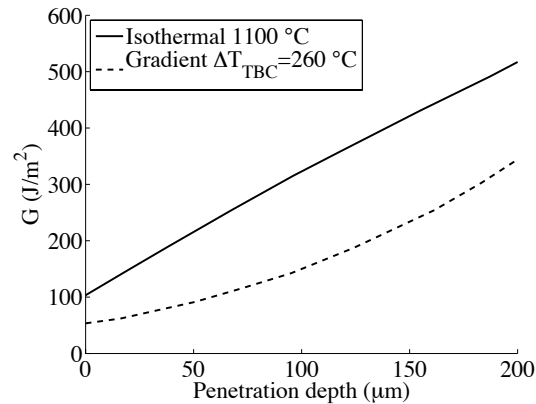


Figure 1.29: Energy release rate ( $G$ ) as a function of CMAS infiltration depth for a delamination crack at the base of a YSZ TBC ( $T_{\text{surface}}=1300 \text{ }^\circ\text{C}$ ,  $T_{\text{bond coat}}=1040 \text{ }^\circ\text{C}$  and  $T_{\text{backside}}=800 \text{ }^\circ\text{C}$ ); comparison with a TBC isothermally heated at  $1100 \text{ }^\circ\text{C}$  (based on information from reference [140])

## 1.7 Modelling issues

### 1.7.1 Assessment of microstructure evolution

#### Oxide growth kinetic

First models that can be used to describe microstructure evolution deal with oxide growth. The oxide growth could be cationic, anionic or a mix of both mechanisms [58]. Classical parabolic kinetic of oxide growth has been evidenced for MCrAlY and NiAl bond-coats, following the time evolution of oxide thickness  $h_{ox}$  accordingly to Wagner's theory [201]:

$$h_{ox}^n = h_{ox,0}^n + k \cdot t \quad (1.2)$$

where  $h_{ox,0}$  is an initial oxide thickness,  $k$  and  $n$  are material parameters, with  $n$  being often close to 2 for isothermal oxidation. In this equation,  $k$  is following Arrhenius' law:

$$k = k_0 \cdot \exp\left(-\frac{Q}{RT}\right) \quad (1.3)$$

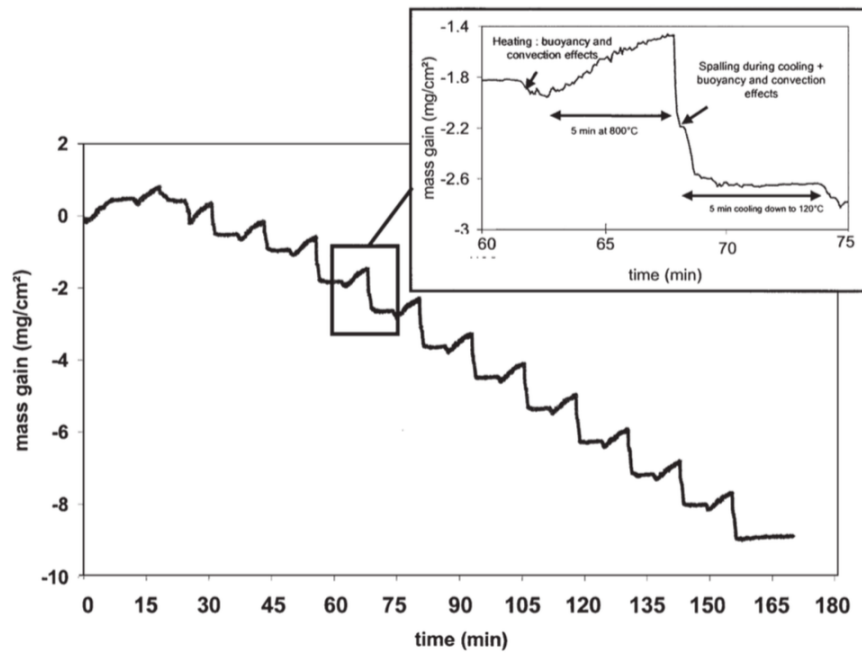
where  $k_0$  is the kinetic constant of oxide growth,  $Q$  is the activation energy of the oxide to be considered and  $R$  is the universal gas constant (8.314 kJ.mol<sup>-1</sup>). For transient temperature, and consequently for thermal cycling, the associated differential equation evaluated at the current time  $t$  and temperature  $T$  corresponds to:

$$dh_{ox} = \frac{k_0}{n} \exp\left(-\frac{Q}{RT}\right) \frac{dt}{h_{ox}^{n-1}} \quad (1.4)$$

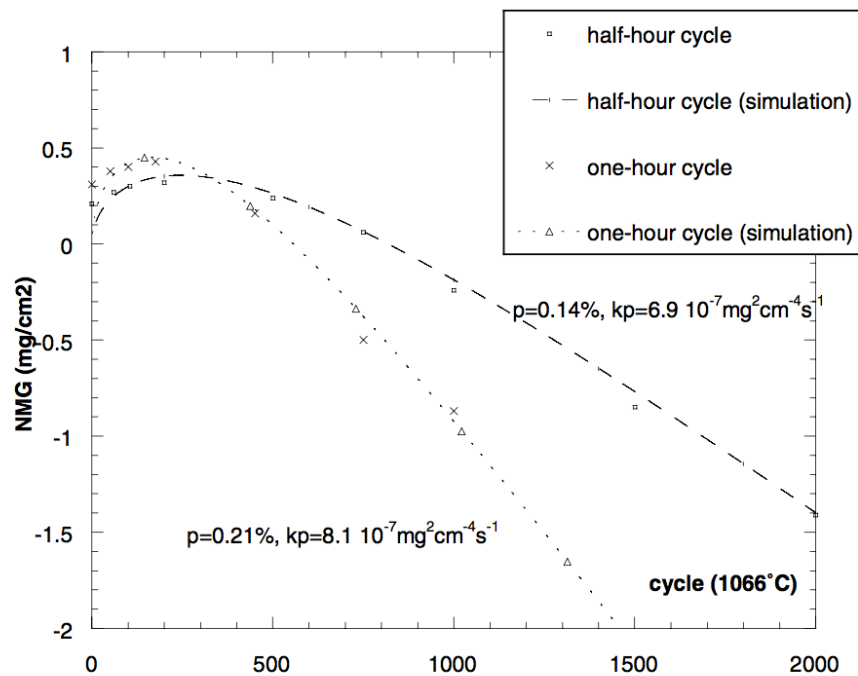
where temperature evolution is neglected during the time step  $dt$  [40].

The oxide layer is prone to damage (local cracking) and local oxide spallation, yielding a strong modification of subsequent oxidation kinetic [59, 58]. The simplest way to model a realistic oxidation kinetic is to associate to the previous parabolic growth a probability of failure with time, the so-called  $p-kp$  theory, where  $p$  describes this probability of local spallation [167, 142, 121]. The probability of failure at each thermal cycle can be measured experimentally by in situ weighting of specimen, Figure 1.30(a) [121], and leads to a very good approximation of experimental data, including sensitivity to thermal cycling frequency, Figure 1.30(b) [142].

In presence of the TC, the limited spallation of oxide strongly modifies a priori critical oxide thickness (see paragraph 1.5). Thus explicit model of TGO growth accounting for both diffusion and oxide growth kinetics are of interest [25, 65, 222]. However, very few studies have been devoted to fully coupled model between mechanical state, oxide failure and oxide kinetic. Strong coupling based on phase field has been for the time being mostly limited to other materials (including NiAl seen as a model material). Modified Fick's law accounting for stress gradient could be coupled to elastoviscoplastic material in the framework of crystal plasticity. For instance, the case of 316L alloy exhibits that oxidation induces strain localization both along grain boundary and in forming



(a)



(b)

Figure 1.30: Net mass gain evolution (a) measured experimentally in situ to derive the oxide growth kinetic  $k_p$  and probability of oxide spallation  $p$  [121] and (b) measured experimentally ex situ by weighting of specimen after each cycle and modeled by  $p - k_p$  [142]

intergranular oxide, Figure 1.31 [43, 178]. This kind of mechanism is likely to induce interfacial damage for most TBC systems, considering intergranular oxidation within the BC.

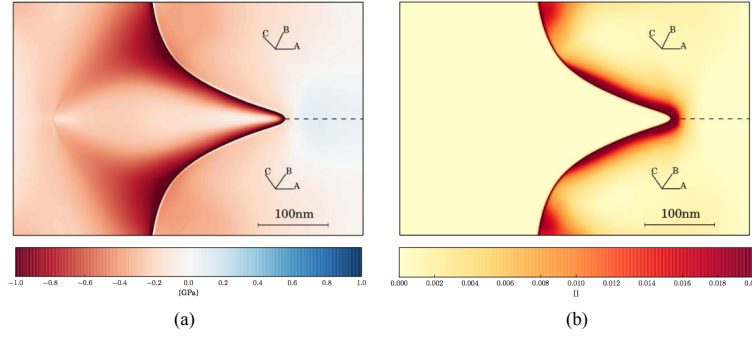


Figure 1.31: Phase field model of 316L oxidation accounting for crystal plasticity and diffusion coupled to stress level, (a) hydrostatic pressure and (b) cumulated plastic strain field [43]

### Phase transformation

Modeling of phase transformation in coated systems is of major interest for optimal design of both the composition of the bond-coat and the target composition of the substrate alloy. Basic composition evaluation could be based on binary phase diagram analysis and diffusion coefficient of Ni and Al [165, 203, 204]. Moreover, this kind of analytical model could be easily linked to oxide loss analysis to consider evolution of realistic boundary condition for diffusion analysis [143].

The major concern, similar to TGO growth analysis, is to obtain a realistic value of the diffusion coefficients. Most advanced models for the estimation of diffusion coefficients are based on CALPHAD, considering multi-component alloys and mobility database to modify the diffusion coefficient as a function of local composition [214, 33, 135] where phase field models are straightforward to model diffusion coefficient [216].

However, the computation time to obtain converged solution in 2D FEA of diffusion remains an issue to take into consideration complex composition and/or realistic morphology of precipitates. The phase field approach has been intensively used to describe aging leading to rafting in the bare substrate single crystal [67, 217]. Regarding coatings, phase field analysis has been straightforward to consider chemical, interfacial, and elastic energies for simplified materials [175]. This method provides evolution of microstructure as a function of time, with large modifications of  $\gamma'$  precipitate morphology at and near the interface between substrate and BC, Figure 1.32, yielding polycrystal formation in the substrate accordingly to the authors analysis [175]. Moreover, in presence

of temperature gradient, the rate of dissolution of  $\gamma'$  in the coating region is increased as compared to isothermal condition. It is worth noting that the height of the figure corresponds to only  $50 \mu\text{m}$  for a 2D model, a limitation owing to the high computation cost of such a model. To the authors knowledge, no results have been provided in the case of full coupling for a coated single crystal substrate implying phase transformation, oxide formation, elastoviscoplasticity, and local damage.

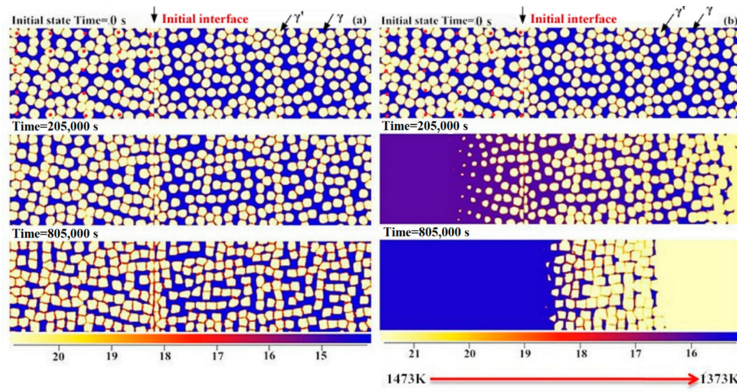


Figure 1.32: Phase-field simulated microstructure evolution of microstructure at the interface between  $\gamma/\gamma'$  bond coat and  $\gamma/\gamma'$  substrate system (Ni-18.5at.%Al-11.25at.%Cr/Ni-18at.%Al-12at.%Cr) annealed (a) at 1373 K and (b) with an effect of temperature gradient (color bar scale indicates the mole fraction of Al in atom percent, the height of the figure corresponds to  $50 \mu\text{m}$ ; vertical arrow indicates initial BC-substrate interface, BC being on left side and substrate on the right side of the pictures respectively) [175]

## 1.7.2 Assessment of mechanical state evolution

### Flat multilayer model for weak and strong coupling

The simplest way to assess the mechanical state in a multi-layered system is to consider a flat multilayer analysis assuming that the total strain is prescribed by the substrate to other layers (TGO/BC/TC). This could be applied to any mechanical behavior for each layer (elasticity, plasticity, viscoplasticity, hardening). For large thickness of the substrate as compared to each layer thickness, this approach is valuable but would be limited for thin substrate (hundreds of microns) cases and would ignore shear stress induced by mechanical properties mismatch at the interface associated to local roughness. This approach is considered as a weak coupling because of the absence of interactions between layers [40].

In presence of an interfacial crack, elastic mismatch could be easily described

by the Dundur's parameters [81]. To account for plasticity in the metal (either BC or substrate) the use of HRR field is prescribed but limited to Ramberg-Osgood non-linear behavior [162]. FEA is in this case straightforward by the use of cohesive zone model (CZM): the interfacial behavior is explicitly described by non-linear laws fitted to describe the interfacial toughness, the behavior being non-linear after damage initiation for either monotonic or fatigue loading [154]. In this case, the shear is modeled without coarse assumption and could also integrate description of coupling between local damage and modification of thermal conductivity [147]. CZM could be applied either to simplified substrate/TC model or to full description of each layer constitutive of the TBC (TGO/BC/TC).

### Describing interfacial morphology

The assumption of a flat interface between BC and TC is oversimplifying the mechanical state. Especially, APS coatings show a high roughness at the surface and consequently at the interface between BC and TC. EB-PVD coating systems are processed to have a smoother interface. However, in EB-PVD systems localized asperities or undulations occur in industrial coating processes. Particularly, accounting for local roughness could provide a driving force for local damage associated to out-of-plane stress which is ignored in a flat interface assumption. Thus, Chang et al have proposed to focus the analysis on a simplified sinusoidal 2D pattern representative of the roughness at the interface between top coat and bond coat [32]. In this way, it is possible to address the influence of local roughness and the interaction between each layer constitutive of the TBC system.

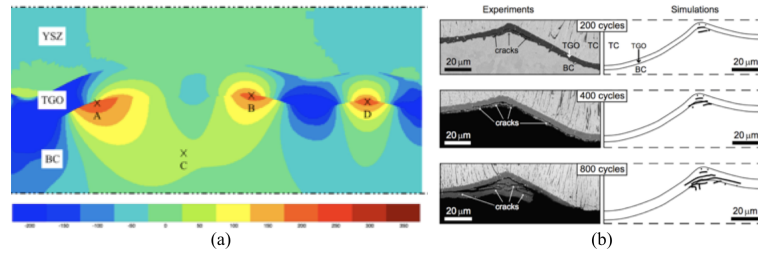


Figure 1.33: Modeling of interfacial imperfection by (a) different wave lengths and amplitudes of roughness to highlight local stress concentrations [107] (b) oxide cracking at a single undulation with increasing number of thermal cycles with experimental findings on the left and simulation results on the right [79]

Derived from the sinusoidal pattern approach, a class of analytical models has been developed by Balint and Hutchinson [10]. These models are of high interest to account for both shear and out-of-plane interactions between layers, that is straightforward to assess the evolution of rumpling with thermal cycling [12, 11, 194] and complex thermal mechanical cycling [161].

This approach has been very successful and led to most of open literature models with continuous increase in complexity. First, it has been proposed to consider the most advanced mechanical behavior of each layer to obtain relevant stress state in TBC after high temperature stress relaxation [25]. Some authors have also tested the influence of microstructure evolution (oxide growth, martensitic transformation) [27, 91], the influence of oxide cracking [79], the influence of 2D and 3D realistic morphologies to access relevant evolution of mechanical state in the TBC [107], Figure 1.33(a) and (b). While in a coating system with adherent TC the BC is constraint and roughness evolution during thermal and mechanical loading is limited, the situation changes drastically at local separations between TC and BC. In [92] Karlsson et al. developed a model to describe the growth of undulations at local delaminations between BC and an EB-PVD top coat during thermal cycling. They introduced a term for not only thickening but also lengthening of the TGO and were able to capture with their model the experimentally observed amplitude increase of initially existing undulations at local delaminations in a PtAl-BC and EB-PVD TC system. Later, Shi et al. [161] modelled the amplitude growth of initial undulations for a NiCoCrAlY BC for thermal, thermal gradient and thermal gradient mechanical fatigue (TGMF) loading and could capture well respective experimental results, Figure 1.34.

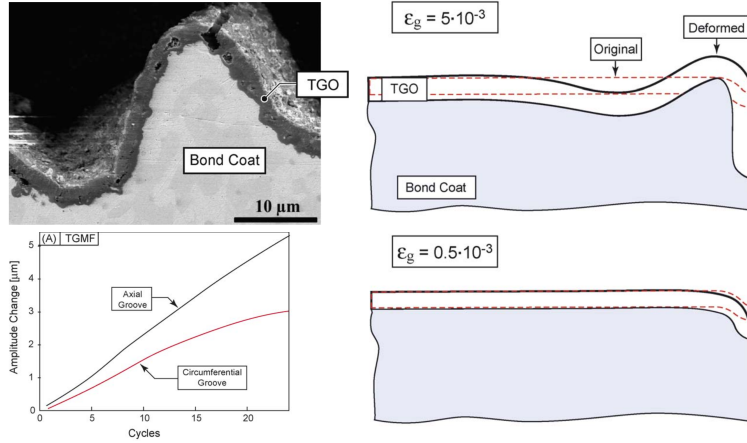


Figure 1.34: Rumpling modeling by initial defect meshing and strain increase associated to oxide growth in plane and out of plane (thickening and lengthening strain) and thermal gradient mechanical fatigue (TGMF) loading [161]

### 1.7.3 Lifetime modeling

Pioneer works have been formulated by Miller [118]: he proposed to view damage growth as a result of the coupling between oxide growth, modeled by the NMG at

the current cycle  $W_N$ , to mechanical loading, modeled by the thermal expansion mismatch strain  $\varepsilon_r$ . He therefore obtained a formalism very similar to standard fatigue damage laws:

$$\sum_{N=1}^{N_f} \left\{ \left( 1 - \frac{\varepsilon_{f0}}{\varepsilon_r} \right) \left( \frac{W_N}{W_C} \right)^m + \frac{\varepsilon_{f0}}{\varepsilon_r} \right\}^{-b} = 1 \quad (1.5)$$

where  $W_C$  is the NMG yielding failure in one cycle,  $\varepsilon_{f0}$  is the critical strain at failure without aging,  $m$  and  $b$  being material parameters to be identified.

While Miller in [118] did not consider microstructural features, but used global values for critical strain, Chang et al. [32] calculated local stress concentrations for a simplified 2D model representing undulations as occurring in APS manufactured TBC coatings. However, for this simplified sinusoidal pattern, the link between local failure, assumed to be associated to oxide failure, to the macroscopic TC failure is not obvious. Busso et al. have proposed a model based on mapping of local roughness influence on local stress (out-of-plane component) seen as the driving force for local damage induced by thermal fatigue, to establish a failure criterion [26]. Another approach based on local modelling of oxide cracking by CZM shows spectacular results in capturing experimentally observed micro-cracking [79]. But for most of these models, the limiting factor is the extremely high sensitivity of prediction to the knowledge of the mechanical behavior of the bond-coat, including the impact of aging and multiaxial and non-proportional loading in a wide range of temperature. As elaborated in section 1.3.3, limited robust results are available on bond coat materials, especially only few data are reported on properties after aging.

As mentioned before, it is further quite difficult to transpose descriptions of local damage processes to macroscopic spallation of the TBC. For this purpose, models have been developed, which link progressive damage of the interfacial region during cyclic loading to fatigue crack growth at the interface between BC and TC leading to TC spallation.

Miller presented in [118] an approach, which combines the strain induced by oxidation with the mismatch strain between TC and substrate during a thermal cycle to an effective strain  $\varepsilon_e$  as driving force for the propagation  $da/dN$  of a defined crack of length  $a$ :

$$\frac{da}{dN} = A\varepsilon_e^b a^d \quad (1.6)$$

$$\varepsilon_e = (\varepsilon_f - \varepsilon_r)(w/w_c)^m + \varepsilon_r \quad (1.7)$$

with  $\varepsilon_r$  the mismatch strain between TC and substrate,  $\varepsilon_f$  the failure strain of the TC in the as-processed condition,  $w$  the NMG and  $w_c$  a critical mass gain causing TC failure in a single thermal cycle. Other terms being materials parameters to be optimized on experimental database. More recently, it has been established that two damage terms could be used to describe the damage

induced by isothermal oxidation  $D_{\text{ox}}$ , using a direct function of the oxide thickness, and the damage induced by thermal cycling  $D_r$ , combining cumulated plasticity in the bond-coat to oxide growth [40]:

$$dD_{\text{ox}} = \frac{m}{h_0} \left( \frac{h_{\text{ox}}}{h_0} \right)^{m-1} dh_{\text{ox}} \quad (1.8)$$

where  $h_{\text{ox}}$  is the current oxide thickness (accounting for temperature and time increment by incremental formulation of oxidation model seen in equation 1.2),  $m$  and  $h_0$  being the material dependent parameters to be identified.

$$dD_r = N \frac{m}{h_0} \left( \frac{\varepsilon_{\text{cum}}}{\varepsilon_0} \right)^n \left( \frac{h_{\text{ox}}}{h_0} \right)^{m-1} dh_{\text{ox}} + \left( \frac{\varepsilon_{\text{cum}}^0}{\varepsilon_0} \right)^n \left( \frac{h_{\text{ox}}}{h_0} \right)^m dN \quad (1.9)$$

where  $\varepsilon_{\text{cum}}$  is the cumulated plastic strain evaluated in the BC layer based on a flat multi-layer assumption,  $N$  is the current cycle,  $n$  and  $\varepsilon_0$  being the material dependent parameters to be identified. The macroscopic damage parameter  $D$  is the combination of integrated values of damage  $D_{\text{ox}}$  and  $D_r$ , with  $D = (1 - D_{\text{ox}})(1 - D_r)$ .

TC spallation occurs in this case when compressive strain in the TC reaches a critical strain at spallation controlled by interfacial damage, assuming that buckling strain is the critical parameter:

$$\varepsilon_{\text{crit}} = \frac{1.2235}{1 + \nu_1} \left( \frac{h}{R_0} \right)^2 (1 - D) \quad (1.10)$$

where  $h$  is the TC thickness and  $R_0$  is the initial radius of a circular delaminated area with both  $h$  and  $R_0$  relevant for buckling [40]. In [?, 108] it was shown that elastic anisotropy and plastic strain localization, as it is the case for single crystalline superalloys, both result in strain variation depending on the orientation and influences the shape of the delamination and the time until buckling occurs.

The models by [118] and [40] explored the interfacial crack growth and TC failure as a stability criterion governed by interfacial toughness evolution as a function of loading history. The reason for this is that it is difficult to observe slow or stable crack growth in EB-PVD systems which have rather smooth interfaces and show more or less spontaneous spallation.

In APS-TBC systems the coating lifetime is mainly governed by crack growth in the vicinity of the TC/TGO interface and allows for measurement of progressive spallation in the course of thermal cycling [89]. In this study, button shape specimen and edge delamination is considered. The proposed approach yields to a fatigue crack growth rate evaluation:

$$\frac{dc}{dN} = A(G)^m \quad (1.11)$$

where  $c$  is a macroscopic crack length,  $A$  and  $m$  being the classical Paris law parameters and  $G$  is the energy release rate. These measurements and model are straightforward for APS YSZ coating because after local spallation at the edge of the specimen, the remaining TC is still adherent to the substrate yielding to a progressive delamination of the TC. Moreover, a linear relationship between interfacial decohesion and spallation has been established, see Figure 1.35.

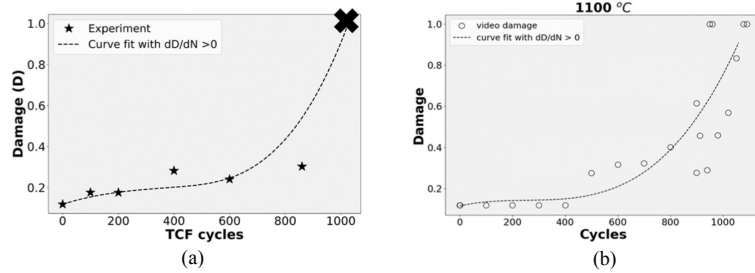


Figure 1.35: Fatigue model based on Paris like crack growth analysis for an APS TBC system under thermal cycling, (a) maximum interfacial crack length, and (b) spalled TC area fraction as a function of cycles number [89]

Based on 4 points bending measurement, Figure 1.16, Vaunois and coworkers have proposed in [195] to determine a damage model controlling the decrease of interfacial toughness by mixing out-of-plane stress and plasticity associated to rumpling like damage as developed in Courcier et al. [40].

Inspired by the complex interface analysis detailed above, including a sinusoidal pattern to describe rough interface, it has been proposed to explore the influence of local roughness and defects on crack propagation using CZM [169]. Main results have shown that the sensitivity to local defects was rather low as compared to the global interfacial toughness. This result fully justifies that, to describe global decohesion of the TC at the length scale of the component, direct CZM models are straightforward [147, 159]. In this case, the interfacial toughness should be a function of the aging of the material, described by a lower length scale model such as described in [79] or [155]. However, a difference should be kept in mind between microstructure evolution and damage evolution, here related to interfacial decohesion: for the same TBC system and similar thermomechanical loading, the respective evolution of phase transformation in the BC, Fig. 1.36(b), and interfacial damage, Fig. 1.36(c), yield different localization paths.

CZM approach has been successfully applied to describe the influence of biaxial complex loading on a simplified coating system consisting of a ceramic layer directly applied onto a superalloy substrate [159]. It has been shown that an initial circular defect, here obtained by the LASAT method, turns into an elliptical one for macroscopic combination of tension and compression in the plane of the substrate. This effect was induced by local closure and opening of

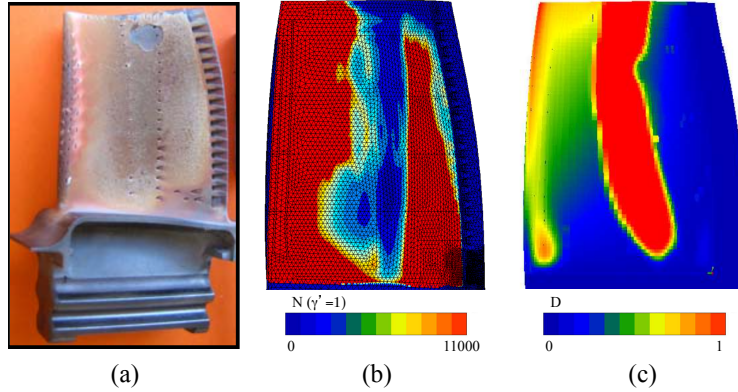


Figure 1.36: High pressure turbine blade, (a) photo of a blade after use in-service [183], (b) phase transformation in bond coat due to thermal exposure, showing the calculated number of cycles to reach a volumic fraction of  $\gamma'=1$  (complete transformation from  $\beta$  to  $\gamma'$ ) [155], and (c) calculated interfacial damage of the TBC system after thermal exposure [147]

the delamination crack between ceramic layer and substrate under compression and tension with a more pronounced crack growth in tensile direction than in the compressive direction [159], see Figure 1.37. It is worth noting that some similar observation can be made on single crystal substrate when uniaxial loading is applied (isothermal or TMF loading): here the anisotropy of the substrate induces a strong Poisson effect, where for compressive loading the orthogonal direction is bearing tensile strain inducing an elliptical decohesion [208, 108].

#### 1.7.4 Concluding remarks: Challenges from theory to application

The fantastic progress in coating technology, physical understanding of microstructure and damage evolution, characterization of TBC and modelling could let us dream about a full model predicting life as a direct function of the chosen manufacturing process and composition of the TBC. However, only partial junctions could be made nowadays including:

- from composition to microstructure and microstructure evolution, diffusion and phase field models are promising to predict aging;
- from microstructure evolution, testing of free standing coatings or complete TBC using synchrotron facilities gives access to layers mechanical properties;

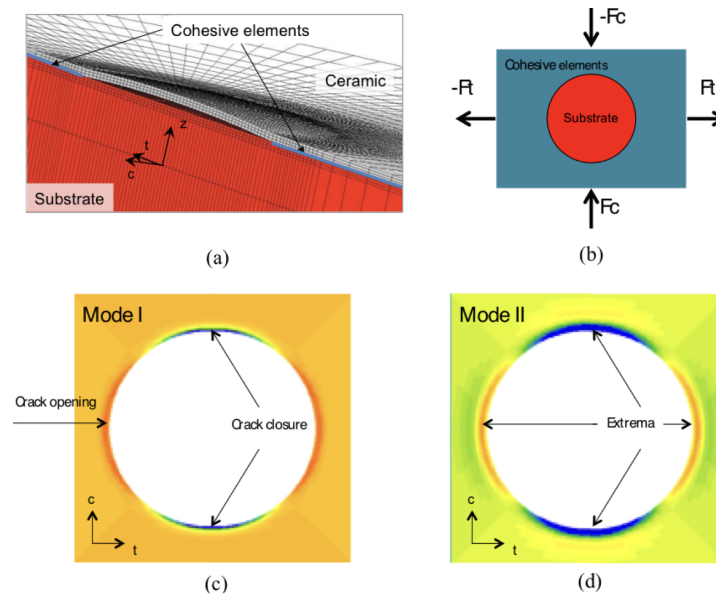


Figure 1.37: Modeling of in-plane biaxial testing (a) perspective view of the half-model highlighting ceramic blister and substrate, (b) schematic top-view without ceramic layer, no cohesive elements are used within the blister making the substrate visible;  $F_t$  and  $F_c$  indicate in-plane tension and compression, respectively, (c) opening stress component ( $\sigma_{zz}$ ), and (d) shear stress component ( $\sigma_{tc}$ ) highlighting equivalence in shear mode for  $c$  and  $t$  directions adapted from [159, 158]

- from morphology and local mechanical properties, FEA yields stress evolution for complex loading conditions;
- from adhesion testing, interfacial toughness assessment enables to predict lifetime of the TBC.

Among missing links, the most critical issue is certainly from microstructure to mechanical properties, including interfacial properties. It is also critical today to give a clear physical basis of the coupling between complex thermo-mechanical loading and observed large impact on phase transformation. However, it is worth noting that a full field model including phase field approach implies a very large CPU time to compute few  $\mu\text{m}^3$ . At a larger scale length, for instance to determine interfacial damage by CZM, implies finite elements sized to few microns to deal with tenths to hundreds of  $\mu\text{m}^3$ . As a direct consequence, computing a component could not be achieved with local models but should be based on homogenized model (analytical or not) to stay within a reasonable computing time for design purpose.

# Bibliography

- [1] S. Ahmadian, A. Browning, and E. H. Jordan. Three-dimensional x-ray micro-computed tomography of cracks in a furnace cycled air plasma sprayed thermal barrier coating. *Scripta Materialia*, 97:13–16, 2015. One citation in page [XXXII](#).
- [2] M. Ahrens, R. Vaßen, D. Stöver, and S. Lampenscherf. Sintering and creep processes in plasma-sprayed thermal barrier coatings. *Journal of thermal spray technology*, 13(3):432–442, 2004. One citation in page [XIII](#).
- [3] M. Z. Alam, S. Kamat, V. Jayaram, and D. K. Das. Tensile behavior of a free-standing pt-aluminide (ptal) bond coat. *Acta materialia*, 61(4):1093–1105, 2013. 2 citations in pages [XXI](#) and [XXIII](#).
- [4] M. Z. Alam, C. Parlikar, D. Chatterjee, and D. K. Das. Comparative tensile behavior of freestanding  $\gamma/\gamma'$  and  $\beta$ -(Ni,Pt)Al bond coats and effect on tensile properties of coated superalloy. *Materials Design*, 114:505–514, 2017. One citation in page [XXXV](#).
- [5] A. Anwaar, L. Wei, Q. Guo, B. Zhang, and H. Guo. Novel prospects for plasma spray–physical vapor deposition of columnar thermal barrier coatings. *Journal of Thermal Spray Technology*, 26(8):1810–1822, 2017. One citation in page [XV](#).
- [6] P. Audigié, A. Rouaix-Van de Put, A. Malié, C. Thouron, and D. Monceau. High-temperature cyclic oxidation behaviour of pt-rich  $\gamma$ - $\gamma'$  coatings. part ii: Effect of pt and al on the system lifetime. *Corrosion Science*, 150:1–8, 2019. One citation in page [XL](#).
- [7] A. Aygun, A. L. Vasiliev, N. P. Padture, and X. Ma. Novel thermal barrier coatings that are resistant to high-temperature attack by glassy deposits. *Acta Materialia*, 55(20):6734–6745, 2007. 2 citations in pages [XLV](#) and [XLVI](#).
- [8] H.-A. Bahr, H. Balke, T. Fett, I. Hofinger, G. Kirchhoff, D. Munz, A. Neubrand, A. Semenov, H.-J. Weiss, and Y. Yang. Cracks in functionally graded materials. *Materials Science and Engineering: A*, 362(1-2):2–16, 2003. One citation in page [XXXVI](#).

- [9] E. Bakan and R. Vaßen. Ceramic top coats of plasma-sprayed thermal barrier coatings: materials, processes, and properties. *Journal of Thermal Spray Technology*, 26(6):992–1010, 2017. One citation in page [XVII](#).
- [10] D. Balint and J. Hutchinson. An analytical model of rumpling in thermal barrier coatings. *J. Mech. Phys. Sol.*, 53:949–973, 2005. One citation in page [LIV](#).
- [11] D. Balint, S.-S. Kim, Y.-F. Liu, R. Kitazawa, Y. Kagawa, and A. Evans. Anisotropic tgo rumpling in EB-PVD thermal barrier coatings under in-phase thermomechanical loading. *Acta Materialia*, 59(6):2544–2555, 2011. 2 citations in pages [XLIII](#) and [LIV](#).
- [12] D. S. Balint and J. W. Hutchinson. Undulation instability of a compressed elastic film on a nonlinear creeping substrate. *Acta Materialia*, 51(13):3965 – 3983, 2003. One citation in page [LIV](#).
- [13] M. Bartsch, B. Baufeld, S. Dalkiliç, L. Chernova, and M. Heinzelmänn. Fatigue cracks in a thermal barrier coating system on a superalloy in multiaxial thermomechanical testing. *International Journal of Fatigue*, 30(2):211–218, 2 2008. 2 citations in pages [XLIII](#) and [XLIV](#).
- [14] M. Bartsch, B. Baufeld, S. Dalkiliç, and I. Mircea. Testing and characterization of ceramic thermal barrier coatings. In *Materials Science Forum*, volume 492, pages 3–8. Trans Tech Publ, 2005. One citation in page [XLII](#).
- [15] M. Bartsch, G. Marci, K. Mull, and C. Sick. Fatigue testing of ceramic thermal barrier coatings for gas turbine blades. *Adv. Eng. Mat.*, 2:127–129, 1999. One citation in page [XLIII](#).
- [16] B. Baufeld, M. Bartsch, and M. Heinzelmänn. Advanced thermal gradient mechanical fatigue testing of CMSX-4 with an oxidation protection coating. *Int. J. Fat.*, 30:219–225, 2008. 2 citations in pages [XXXIII](#) and [XXXIV](#).
- [17] G. Bégué, G. Fabre, V. Guipont, M. Jeandin, P. Bilhe, J. Y. Guedou, and F. Lepoutre. Laser shock adhesion test (lasat) of EB-PVD tbc: Towards an industrial application. *Surface and Coatings Technology*, 237:305–312, 2013. 2 citations in pages [XXIX](#) and [XXX](#).
- [18] B. Bernard, A. Quet, L. Bianchi, V. Schick, A. Joulia, A. Malié, and B. Rémy. Effect of suspension plasma-sprayed YSZ columnar microstructure and bond coat surface preparation on thermal barrier coating properties. *Journal of Thermal Spray Technology*, 26(6):1025–1037, 2017. One citation in page [XXXIII](#).
- [19] L. Berthe, M. Arrigoni, M. Boustie, J. P. Cuq-Lelandais, C. Broussillou, G. Fabre, M. Jeandin, V. Guipont, and M. Nivard. State-of-the-art laser adhesion test (LASAT). *Nondestructive Testing and Evaluation*, 26:303–317, 2011. One citation in page [XXIX](#).

- [20] G. Bolelli, M. G. Righi, M. Z. Mughal, R. Moscatelli, O. Ligabue, N. Antolotti, M. Sebastiani, L. Lusvarghi, and E. Bemporad. Damage progression in thermal barrier coating systems during thermal cycling: A nano-mechanical assessment. *Materials & Design*, 166:107615, 2019. One citation in page [XXIII](#).
- [21] M. P. Borom, C. A. Johnson, and L. A. Peluso. Role of environment deposits and operating surface temperature in spallation of air plasma sprayed thermal barrier coatings. *Surface and Coatings Technology*, 86:116–126, 1996. 2 citations in pages [XLV](#) and [XLVI](#).
- [22] W. Braue and P. Mechnich. Recession of an EB-PVD YSZ coated turbine blade by CaSO<sub>4</sub> and Fe, ti-rich CMAS-type deposits. *Journal of the american ceramic society*, 94(12):4483–4489, 2011. 2 citations in pages [XLV](#) and [XLVI](#).
- [23] W. J. Brindley, R. A. Miller, and B. J. Aikin. Controlled thermal expansion coat for thermal barrier coatings, Jan. 26 1999. US Patent 5,863,668. One citation in page [XII](#).
- [24] R. Bürgel, H. J. Maier, and T. Niendorf. Hochtemperaturlegierungen. In *Handbuch Hochtemperatur-Werkstofftechnik*, pages 340–484. Springer, 2011. One citation in page [IX](#).
- [25] E. Busso, J. Lin, and S. Sakurai. A mechanistic study of oxydation-induced degradation in a plasma-sprayed thermal barrier coating system. Part I: model formulation. *Acta Mater.*, 49:1515–1528, 2001. 2 citations in pages [L](#) and [LV](#).
- [26] E. Busso, J. Lin, and S. Sakurai. A mechanistic study of oxydation-induced degradation in a plasma-sprayed thermal barrier coating system. Part II: life prediction model. *Acta Mater.*, 49:1529–1536, 2001. One citation in page [LVI](#).
- [27] E. Busso, L. Wright, H. Evans, L. McCartney, S. Saunders, S. Osgerby, and J. Nunn. A physics-based life prediction methodology for thermal barrier coating systems. *Acta Materialia*, 55(5):1491 – 1503, 2007. One citation in page [LV](#).
- [28] G. Cailletaud and J.-L. Chaboche. Macroscopic description of the microstructural changes induced by varying temperature : Example of IN100 cyclic behaviour. In K. Miller and R. Smith, editors, *3rd Int. Conf. on Mechanical behaviour of metals*, pages 23–32, Cambridge, UK, 1979. ICM3. No citations.
- [29] L. Cao, P. Wollgramm, D. Bürger, A. Kostka, G. Cailletaud, and G. Eggeler. How evolving multiaxial stress states affect the kinetics of rafting during creep of single crystal ni-base superalloys. *Acta Mater.*, 158:381–392, 2018. No citations.

- [30] P. Caron, D. Cornu, T. Khan, and J. De Monicault. Development of a hydrogen resistant superalloy for single crystal blade application in rocket engine turbopumps. *Office national d etudes et de recherches aerospaciales onera-publications-tp*, 1996. One citation in page [XXXV](#).
- [31] P. Caron and O. Lavigne. Recent studies at Onera on superalloys for single crystal turbine blades. *AerospaceLab*, 3:p. 1–14, Nov. 2011. One citation in page [XLII](#).
- [32] G. Chang, W. Phucharoen, and R. Miller. Finite element thermal stress solutions for thermal barrier coatings. *Surface and Coatings Technology*, 32(1):307 – 325, 1987. 2 citations in pages [LIV](#) and [LVI](#).
- [33] H. Chen and D. McCartney. Some aspects on modelling of the  $\beta$ -phase depletion behaviour under different oxide growth kinetics in hvof conical coatings. *Surface and Coatings Technology*, 313:107–114, 2017. One citation in page [LII](#).
- [34] M. W. Chen, M. L. Glynn, R. T. Ott, T. C. Hufnagel, and K. J. Hemker. Characterization and modeling of a martensitic transformation in a platinum modified diffusion aluminide bond coat for thermal barrier coatings. *Acta Materialia*, 51(14):4279 – 4294, 2003. 2 citations in pages [XXXVII](#) and [XXXVIII](#).
- [35] X. Chen, C. Shaw, L. Gelman, and K. T. Grattan. Advances in test and measurement of the interface adhesion and bond strengths in coating-substrate systems, emphasising blister and bulk techniques. *Measurement*, 2019. One citation in page [XXVI](#).
- [36] J. Cheng, E. H. Jordan, B. Barber, and M. Gell. Thermal/residual stress in an electron beam physical vapor deposited thermal barrier coating system. *Acta Materialia*, 46(16):5839 – 5850, 1998. 2 citations in pages [XXXIV](#) and [XXXV](#).
- [37] M. Chieux. *Vieillessement des systemes Barriere Thermique : transformation de phases, oxydation et effet du soufre sur l'adhrence*, in French. PhD thesis, Mines - ParisTech, France, 2010. One citation in page [XLII](#).
- [38] T. Clyne and S. Gill. Residual stresses in thermal spray coatings and their effect on interfacial adhesion: a review of recent work. *Journal of Thermal Spray Technology*, 5(4):401, 1996. One citation in page [XXXVI](#).
- [39] H. Cohrt and F. Thümmeler. Degradation mechanisms of thermal barrier coatings in bending tests. *Surface and Coatings Technology*, 32(1-4):339–348, 1987. One citation in page [XXVI](#).
- [40] C. Courcier, V. Maurel, L. Remy, S. Quilici, I. Rouzou, and A. Phelippeau. Interfacial damage based life model for EB-PVD thermal barrier coating. *Surface and Coatings Technology*, 205(13-14):3763 – 3773, 2011. 8 citations in pages [XXVI](#), [XXXVII](#), [XL](#), [XLI](#), [L](#), [LIII](#), [LVII](#), and [LVIII](#).

- [41] V. Crespo, I. Cano, S. Dosta, and J. Guilemany. The influence of feedstock powders on the cgs deposition efficiency of bond coats for tbc. *Journal of Alloys and Compounds*, 622:394–401, 2015. One citation in page [XI](#).
- [42] J.-P. Culié, G. Cailletaud, and A. Lasalmonie. La contrainte interne en viscoplasticité : comparaison des approches mécaniques et microscopiques. *La recherche aérospatiale*, 1982-2:51–61, 1982. No citations.
- [43] V. De Rancourt, K. Ammar, B. Appolaire, E. P. Busso, and S. Forest. Modelling stress-diffusion controlled phase transformations: application to stress corrosion cracking. In *CSMA 2013, 11e Colloque National en Calcul des Structures*, 2013. One citation in page [LII](#).
- [44] D. De Wet, R. Taylor, and F. Stott. Corrosion mechanisms of zro2-y2o3 thermal barrier coatings in the presence of molten middle-east sand. *Le Journal de Physique IV*, 3(C9):C9–655, 1993. One citation in page [XLVII](#).
- [45] R. Decker. Strengthening mechanisms in nickel-base superalloys. In *Steel Strengthening Mechanism Symposium*, Zürich, Switzerland, May 5–6, 1969. No citations.
- [46] G. Dehm, B. N. Jaya, R. Raghavan, and C. Kirchlechner. Overview on micro-and nanomechanical testing: New insights in interface plasticity and fracture at small length scales. *Acta Materialia*, 142:248–282, 2018. One citation in page [XXIII](#).
- [47] J. Demasi and K. Sheffler. Mechanisms of thermal barrier coating degradation and failure. *Nasa*, 1985. One citation in page [VII](#).
- [48] A. Dennstedt, F. Gaslain, M. Bartsch, V. Guipont, and V. Maurel. Three-dimensional characterization of cracks in a columnar thermal barrier coating system for gas turbine applications. *Integrating Materials and Manufacturing Innovation*, pages 1–13, 2019. One citation in page [XXXII](#).
- [49] J. M. Drexler, A. Aygun, D. Li, R. Vaßen, T. Steinke, and N. P. Padture. Thermal-gradient testing of thermal barrier coatings under simultaneous attack by molten glassy deposits and its mitigation. *Surface and Coatings Technology*, 204(16-17):2683–2688, 2010. One citation in page [XLVIII](#).
- [50] J. M. Drexler, A. D. Gledhill, K. Shinoda, A. L. Vasiliev, K. M. Reddy, S. Sampath, and N. P. Padture. Jet engine coatings for resisting volcanic ash damage. *Advanced Materials*, 23(21):2419–2424, 2011. One citation in page [XLVII](#).
- [51] J. M. Drexler, K. Shinoda, A. L. Ortiz, D. Li, A. L. Vasiliev, A. D. Gledhill, S. Sampath, and N. P. Padture. Air-plasma-sprayed thermal barrier coatings that are resistant to high-temperature attack by glassy deposits. *Acta Materialia*, 58(20):6835–6844, 2010. 2 citations in pages [XLV](#) and [XLVI](#).

- [52] C. Duhamel, J. Caballero, T. Couvant, J. Crépin, F. Gaslain, C. Guerre, H.-T. Le, and M. Wehbi. Intergranular oxidation of nickel-base alloys: potentialities of focused ion beam tomography. *Oxidation of Metals*, 88(3-4):447–457, 2017. One citation in page [XXXII](#).
- [53] C. Eberl, X. Wang, D. S. Gianola, T. D. Nguyen, M. Y. He, A. G. Evans, and K. J. Hemker. In situ measurement of the toughness of the interface between a thermal barrier coating and a ni alloy. *Journal of the American Ceramic Society*, 94(s1):s120–s127, 2011. 2 citations in pages [XXI](#) and [XXXVI](#).
- [54] V. A. Esin, V. Maurel, P. Breton, A. Koster, and S. Selezneff. Increase in ductility of pt-modified nickel aluminide coating with high temperature ageing. *Acta Materialia*, 105:505 – 518, 2016. 2 citations in pages [XXI](#) and [XXII](#).
- [55] A. Evans, M. He, A. Suzuki, M. Gigliotti, B. Hazel, and T. Pollock. A mechanism governing oxidation-assisted low-cycle fatigue of superalloys. *Acta materialia*, 57(10):2969–2983, 2009. 2 citations in pages [XXI](#) and [XLIII](#).
- [56] A. Evans and J. Hutchinson. The mechanics of coating delamination in thermal gradients. *Surface and Coatings Technology*, 201(18):7905–7916, 2007. 2 citations in pages [XLVIII](#) and [XLIX](#).
- [57] A. G. Evans, D. R. Mumm, J. W. Hutchinson, G. H. Meier, and F. S. Pettit. Mechanisms controlling the durability of thermal barrier coatings. *Progress in Materials Science*, 46(5):505 – 553, 2001. 2 citations in pages [VII](#) and [XXXI](#).
- [58] H. E. Evans and R. C. Lobb. Conditions for the initiation of oxide-scale cracking and spallation. *Corrosion Science*, 24(3):209 – 222, 1984. 2 citations in pages [XXXVII](#) and [L](#).
- [59] U. R. Evans. The Mechanism of Oxidation and Tarnishing. *Trans. Electrochem. Soc.*, 91:547–&, 1947. One citation in page [L](#).
- [60] G. Fabre. *Influence des propriétés optiques et de l'endommagement de barrières thermiques EB-PVD pour la mesure d'adhérence par choc laser LASAT-2D (in French)*. PhD thesis, Mines ParisTech, 2013. 2 citations in pages [XXX](#) and [XLI](#).
- [61] G. Fabre, V. Guipont, M. Jeandin, M. Boustie, J. P. Cuq-Lelandais, L. Berthe, A. Pasquet, and J.-Y. Guedou. LAsar Shock Adhesion Test (LASAT) of Electron Beam Physical Vapor Deposited Thermal Barrier Coatings (EB-PVD TBCs). In Heilmaier, M, editor, *Euro Superalloys 2010*, volume 278 of *Advanced Materials Research*, pages 509–514, 2011. One citation in page [XXIX](#).

- [62] P. Fauchais, R. Etchart-Salas, V. Rat, J.-F. Coudert, N. Caron, and K. Wittmann-Ténèze. Parameters controlling liquid plasma spraying: solutions, sols, or suspensions. *Journal of Thermal Spray Technology*, 17(1):31–59, 2008. One citation in page [XIV](#).
- [63] H. Feng, N. Ming, L. Jiedong, H. Xu, C. Guofeng, and Z. Zhongjiao. Effect of strain ranges and phase angles on the thermomechanical fatigue properties of thermal barrier coating system. *Rare Metal Materials and Engineering*, 46(12):3693–3698, 2017. One citation in page [XLIII](#).
- [64] A. Feuerstein, J. Knapp, T. Taylor, A. Ashary, A. Bolcavage, and N. Hitchman. Technical and economical aspects of current thermal barrier coating systems for gas turbine engines by thermal spray and ebpvd: a review. *Journal of Thermal Spray Technology*, 17(2):199–213, 2008. 4 citations in pages [VIII](#), [IX](#), [X](#), and [XIII](#).
- [65] J. Frachon. *Multiscale approach to predict the lifetime of EB-PVD thermal barrier coatings*. PhD thesis, Mines ParisTech, 14 Decembre 2009. One citation in page [L](#).
- [66] L. Gao, H. Guo, L. Wei, C. Li, S. Gong, and H. Xu. Microstructure and mechanical properties of yttria stabilized zirconia coatings prepared by plasma spray physical vapor deposition. *Ceramics International*, 41(7):8305–8311, 2015. One citation in page [XXXV](#).
- [67] A. Gaubert, Y. Le Bouar, and A. Finel. Coupling phase field and viscoplasticity to study rafting in Ni-based superalloys. *Philosophical Magazine B*, 90(1–4):375–404, 2010. One citation in page [LII](#).
- [68] A. D. Gledhill, K. M. Reddy, J. M. Drexler, K. Shinoda, S. Sampath, and N. P. Padture. Mitigation of damage from molten fly ash to air-plasma-sprayed thermal barrier coatings. *Materials Science and Engineering: A*, 528(24):7214–7221, 2011. One citation in page [XLVII](#).
- [69] H. Gleiter and E. Hornbogen. Hardening by coherent precipitates. *Acta Metall.*, 13:576–578, 1965. No citations.
- [70] T. Go, Y. Sohn, G. Mauer, R. Vaßen, and J. Gonzalez-Julian. Cold spray deposition of cr2alc max phase for coatings and bond-coat layers. *Journal of the European Ceramic Society*, 39(4):860–867, 2019. One citation in page [XII](#).
- [71] Y. Gu, B. Ao, G. Wu, and W. Wu. Three-dimensional structure analysis of EB-PVD thermal barrier coatings. In Y. Tian, T. Xiao, and P. Liu, editors, *Second Symposium on Novel Technology of X-Ray Imaging*, volume 11068, pages 638 – 643. International Society for Optics and Photonics, SPIE, 2019. One citation in page [XXXII](#).

- [72] V. Guipont, G. Begue, G. Fabre, and V. Maurel. Buckling and interface strength analyses of EB-PVD tbc combining laser shock adhesion test (lasat) to thermal cycling. *Surf. Coat. Technol.*, under edition(special issue 46th ICMCTF), 2019. 4 citations in pages [XXIX](#), [XXX](#), [XXXI](#), and [XXXVI](#).
- [73] H. Guo, R. Vaßen, and D. Stöver. Atmospheric plasma sprayed thick thermal barrier coatings with high segmentation crack density. *Surface and Coatings technology*, 186(3):353–363, 2004. One citation in page [XIV](#).
- [74] S. Guo, D. Mumm, A. M. Karlsson, and Y. Kagawa. Measurement of interfacial shear mechanical properties in thermal barrier coating systems by a barb pullout method. *Scripta Materialia*, 53(9):1043–1048, 2005. 2 citations in pages [XXV](#) and [XXVII](#).
- [75] F. Hanriot. *Étude du comportement du superalliage AM1 sous sollicitations cycliques*. PhD thesis, ENSMP, 1993. 2 citations in pages [XXXIV](#) and [XXXV](#).
- [76] W. He, G. Mauer, M. Gindrat, R. Wäger, and R. Vaßen. Investigations on the nature of ceramic deposits in plasma spray–physical vapor deposition. *Journal of Thermal Spray Technology*, 26(1-2):83–92, 2017. One citation in page [XV](#).
- [77] M. T. Hernandez, D. Cojocar, M. Bartsch, and A. M. Karlsson. On the opening of a class of fatigue cracks due to thermo-mechanical fatigue testing of thermal barrier coatings. *Computational materials science*, 50(9):2561–2572, 2011. 2 citations in pages [XLII](#) and [XLIV](#).
- [78] M. T. Hernandez, A. M. Karlsson, and M. Bartsch. On tgo creep and the initiation of a class of fatigue cracks in thermal barrier coatings. *Surface and Coatings Technology*, 203(23):3549–3558, 2009. One citation in page [XLIV](#).
- [79] T. S. Hille, T. J. Nijdam, A. S. Suiker, S. Turteltaub, and W. G. Sloof. Damage growth triggered by interface irregularities in thermal barrier coatings. *Acta Materialia*, 57(9):2624 – 2630, 2009. 4 citations in pages [LIV](#), [LV](#), [LVI](#), and [LVIII](#).
- [80] R. Hillery, B. Pilsner, R. McKnight, T. Cook, and M. Hartle. Thermal barrier coating life prediction model development. 1988. 2 citations in pages [XXXIV](#) and [XXXV](#).
- [81] J. Hutchinson and Z. Suo. Mixed mode cracking in layered materials. volume 29 of *Advances in Applied Mechanics*, pages 63 – 191. Elsevier, 1991. One citation in page [LIV](#).
- [82] R. G. Hutchinson and J. W. Hutchinson. Lifetime assessment for thermal barrier coatings: tests for measuring mixed mode delamination toughness.

- Journal of the American Ceramic Society*, 94:s85–s95, 2011. One citation in page [XXXI](#).
- [83] R. W. Jackson and M. R. Begley. Critical cooling rates to avoid transient-driven cracking in thermal barrier coating (tbc) systems. *International Journal of Solids and Structures*, 51(6):1364–1374, 2014. 2 citations in pages [XLVIII](#) and [XLIX](#).
- [84] R. W. Jackson, E. M. Zaleski, B. T. Hazel, M. R. Begley, and C. G. Levi. Response of molten silicate infiltrated gd<sub>2</sub>zr<sub>2</sub>o<sub>7</sub> thermal barrier coatings to temperature gradients. *Acta Materialia*, 132:538–549, 2017. One citation in page [XLVIII](#).
- [85] R. W. Jackson, E. M. Zaleski, D. L. Poerschke, B. T. Hazel, M. R. Begley, and C. G. Levi. Interaction of molten silicates with thermal barrier coatings under temperature gradients. *Acta Materialia*, 89:396–407, 2015. 2 citations in pages [XLVIII](#) and [XLIX](#).
- [86] A. Jadhav, N. P. Padture, F. Wu, E. H. Jordan, and M. Gell. Thick ceramic thermal barrier coatings with high durability deposited using solution-precursor plasma spray. *Materials Science and Engineering: A*, 405(1-2):313–320, 2005. One citation in page [XV](#).
- [87] F. Jing, J. Yang, Z. Yang, and W. Zeng. Critical compressive strain and interfacial damage evolution of EB-PVD thermal barrier coating. *Materials Science and Engineering: A*, page 139038, 2020. One citation in page [XXVI](#).
- [88] M. Jinnestrand and H. Brodin. Crack initiation and propagation in air plasma sprayed thermal barrier coatings, testing and mathematical modelling of low cycle fatigue behaviour. *Materials Science and Engineering: A*, 379(1-2):45–57, 8/15 2004. One citation in page [XLII](#).
- [89] K. P. Jonnalagadda, R. Eriksson, X.-H. Li, and R. L. Peng. Fatigue life prediction of thermal barrier coatings using a simplified crack growth model. *Journal of the European Ceramic Society*, 39(5):1869 – 1876, 2019. 2 citations in pages [LVII](#) and [LVIII](#).
- [90] E. H. Jordan, C. Jiang, J. Roth, and M. Gell. Low thermal conductivity yttria-stabilized zirconia thermal barrier coatings using the solution precursor plasma spray process. *Journal of thermal spray technology*, 23(5):849–859, 2014. One citation in page [XXXIII](#).
- [91] A. M. Karlsson and A. Evans. A numerical model for the cyclic instability of thermally grown oxides in thermal barrier systems. *Acta Materialia*, 49(10):1793–1804, 2001. One citation in page [LV](#).
- [92] A. M. Karlsson, J. Hutchinson, and A. Evans. A fundamental model of cyclic instabilities in thermal barrier systems. *Journal of the Mechanics and Physics of Solids*, 50(8):1565–1589, 2002. One citation in page [LV](#).

- [93] D. Khoshkhou, M. Mostafavi, C. Reinhard, M. Taylor, D. Rickerby, I. Edmonds, H. Evans, T. Marrow, and B. Connolly. Three-dimensional displacement mapping of diffused pt thermal barrier coatings via synchrotron x-ray computed tomography and digital volume correlation. *Scripta Materialia*, 115:100–103, 2016. One citation in page [XXXII](#).
- [94] S.-S. Kim, Y.-F. Liu, and Y. Kagawa. Evaluation of interfacial mechanical properties under shear loading in EB-PVD tbc's by the pushout method. *Acta Materialia*, 55(11):3771 – 3781, 2007. One citation in page [XXXVI](#).
- [95] K. Knipe, A. Manero, S. F. Siddiqui, C. Meid, J. Wischek, J. Okasinski, J. Almer, A. M. Karlsson, M. Bartsch, and S. Raghavan. Strain response of thermal barrier coatings captured under extreme engine environments through synchrotron x-ray diffraction. *Nature communications*, 5(1):1–7, 2014. 3 citations in pages [XXI](#), [XXII](#), and [XLIV](#).
- [96] S. Krämer, S. Faulhaber, M. Chambers, D. Clarke, C. Levi, J. Hutchinson, and A. Evans. Mechanisms of cracking and delamination within thick thermal barrier systems in aero-engines subject to calcium-magnesium-alumino-silicate (CMAS) penetration. *Materials Science and Engineering: A*, 490(1-2):26–35, 2008. 2 citations in pages [XLV](#) and [XLVI](#).
- [97] S. Krämer, J. Yang, and C. G. Levi. Infiltration-inhibiting reaction of gadolinium zirconate thermal barrier coatings with CMAS melts. *Journal of the American Ceramic Society*, 91(2):576–583, 2008. One citation in page [XLVI](#).
- [98] S. Krämer, J. Yang, C. G. Levi, and C. A. Johnson. Thermochemical interaction of thermal barrier coatings with molten CaO–MgO–Al<sub>2</sub>O<sub>3</sub>–SiO<sub>2</sub> (CMAS) deposits. *Journal of the American Ceramic Society*, 89(10):3167–3175, 2006. 3 citations in pages [XLV](#), [XLVI](#), and [XLVII](#).
- [99] A. R. Krause, X. Li, and N. P. Padture. Interaction between ceramic powder and molten calcia-magnesia-alumino-silicate (CMAS) glass, and its implication on CMAS-resistant thermal barrier coatings. *Scripta Materialia*, 112:118–122, 2016. One citation in page [XLVII](#).
- [100] R. Kromer, J. Cormier, S. Costil, D. Courapied, L. Berthe, and P. Peyre. High temperature durability of a bond-coatless plasma-sprayed thermal barrier coating system with laser textured ni-based single crystal substrate. *Surface and Coatings Technology*, 337:168–176, 2018. One citation in page [XII](#).
- [101] C. G. Levi, J. W. Hutchinson, M.-H. Vidal-Sétif, and C. A. Johnson. Environmental degradation of thermal-barrier coatings by molten deposits. *MRS bulletin*, 37(10):932–941, 2012. 5 citations in pages [XLV](#), [XLVI](#), [XLVII](#), [XLVIII](#), and [XLIX](#).

- [102] V. Lughi, V. K. Tolpygo, and D. R. Clarke. Microstructural aspects of the sintering of thermal barrier coatings. *Materials Science and Engineering: A*, 368(1-2):212–221, 2004. One citation in page [XL](#).
- [103] D. E. Mack, T. Wobst, M. O. D. Jarligo, D. Sebold, and R. Vaßen. Lifetime and failure modes of plasma sprayed thermal barrier coatings in thermal gradient rig tests with simultaneous CMAS injection. *Surface and Coatings Technology*, 324:36–47, 2017. 2 citations in pages [XLIV](#) and [XLVIII](#).
- [104] J. Manara, M. Arduini-Schuster, H.-J. Rätzer-Scheibe, and U. Schulz. Infrared-optical properties and heat transfer coefficients of semitransparent thermal barrier coatings. *Surface and Coatings Technology*, 203(8):1059–1068, 2009. One citation in page [XIX](#).
- [105] A. Manero, S. Sofronsky, K. Knipe, C. Meid, J. Wischek, J. Okasinski, J. Almer, A. M. Karlsson, S. Raghavan, and M. Bartsch. Monitoring local strain in a thermal barrier coating system under thermal mechanical gas turbine operating conditions. *JOM*, 67(7):1528–1539, 2015. 2 citations in pages [XXI](#) and [XLIV](#).
- [106] F. Mauget, F. Hamon, M. Morisset, J. Cormier, F. Riallant, and J. Mendez. Damage mechanisms in an EB-PVD thermal barrier coating system during TMF and TGMF testing conditions under combustion environment. *Int. J. Fat.*, 99:225–234, 2017. 2 citations in pages [XLII](#) and [XLIV](#).
- [107] V. Maurel, E. Busso, J. Frachon, J. Besson, and F. N’Guyen. A methodology to model the complex morphology of rough interfaces. *International Journal of Solids and Structures*, 51(19):3293 – 3302, 2014. 2 citations in pages [LIV](#) and [LV](#).
- [108] V. Maurel, P. de Bodman, and L. Remy. Influence of substrate strain anisotropy in tbc system failure. *Surface and Coatings Technology*, 206(7):1634 – 1639, 2011. 4 citations in pages [XXVIII](#), [XXXI](#), [LVII](#), and [LIX](#).
- [109] V. Maurel, V. A. Esin, P. Sallot, F. Gaslain, S. Gailliege, and L. Rémy. Rumpling of nickel aluminide coatings: a reassessment of respective influence of thermal grown oxide and phase transformations. *Materials at High Temperatures*, 33(4-5):318–324, 2016. One citation in page [XXXVIII](#).
- [110] V. Maurel, V. Guipont, M. Theveneau, B. Marchand, and F. Coudon. Thermal cycling damage monitoring of thermal barrier coating assisted with lasat (laser shock adhesion test). *Surface and Coatings Technology*, 380:125048, 2019. 3 citations in pages [XXIX](#), [XXX](#), and [XXXI](#).
- [111] V. Maurel, M. Harvey, and L. Rémy. Aluminium oxide spallation on NiAl coating induced by compression surface. *Surface & Coatings Technology*, 205:3158–3166, 2011. One citation in page [XXVI](#).

- [112] V. Maurel, L. Mahfouz, V. Guipont, B. Marchand, F. Gaslain, A. Koster, A. Dennstedt, M. Bartsch, and F. Coudon. Recent progress in local characterization of damage evolution in thermal barrier coating under thermal cycling. *Superalloys*, 2020. One citation in page [XXIX](#).
- [113] V. Maurel, R. Soullignac, L. Helfen, T. Morgeneyer, A. Koster, and L. Remy. Three-dimensional damage evolution measurement in ebpvd tbc using synchrotron laminography. *Oxidat. of Metals*, 79(3-4, SI):313–323, 2013. 2 citations in pages [XXXII](#) and [XXXVIII](#).
- [114] J. P. McDonald, M. Thouless, and S. M. Yalisove. Mechanics analysis of femtosecond laser-induced blisters produced in thermally grown oxide on si(100). *Journal of Materials Research*, 25(6):1087–1095, 2010. One citation in page [XXIX](#).
- [115] P. Mechnich, W. Braue, and U. Schulz. High-temperature corrosion of EB-PVD yttria partially stabilized zirconia thermal barrier coatings with an artificial volcanic ash overlay. *Journal of the American Ceramic Society*, 94(3):925–931, 2011. 2 citations in pages [XLV](#) and [XLVII](#).
- [116] C. Mercer, S. Faulhaber, A. Evans, and R. Darolia. A delamination mechanism for thermal barrier coatings subject to calcium–magnesium–aluminosilicate (CMAS) infiltration. *Acta materialia*, 53(4):1029–1039, 2005. 4 citations in pages [XLV](#), [XLVI](#), [XLVIII](#), and [XLIX](#).
- [117] R. Mevrel and R. Pichoir. Les revêtements par diffusion. *Mat. Sci. and Engng A*, 88:1–9, 1987. One citation in page [XXI](#).
- [118] R. Miller. Oxidation-based model for thermal barrier coating life. *Journal of the American Ceramic Society*, 67(8):517 – 521, 1984. 3 citations in pages [LV](#), [LVI](#), and [LVII](#).
- [119] P. Mohan, B. Yuan, T. Patterson, V. Desai, and Y. H. Sohn. Degradation of yttria stabilized zirconia thermal barrier coatings by molten CMAS (CaO-MgO-Al<sub>2</sub>O<sub>3</sub>-SiO<sub>2</sub>) deposits. In *Materials Science Forum*, volume 595, pages 207–212. Trans Tech Publ, 2008. One citation in page [XLVI](#).
- [120] M. Mollard, F. Pedraza, B. Bouchaud, X. Montero, M. Galetz, and M. Schütze. Influence of the superalloy substrate in the synthesis of the pt-modified aluminide bond coat made by slurry. *Surface and Coatings Technology*, 270:102–108, 2015. One citation in page [XII](#).
- [121] D. Monceau and D. Poquillon. Continuous thermogravimetry under cyclic conditions. *Oxidation of Metals*, 61:143–163, 2004. 2 citations in pages [L](#) and [LI](#).
- [122] T. Morgeneyer and J. Besson. Flat to slant ductile fracture transition: Tomography examination and simulations using shear-controlled void nucleation. *Scripta Materialia*, 65(11):1002 – 1005, 2011. One citation in page [XXXII](#).

- [123] R. Naraparaju, M. Hüttermann, U. Schulz, and P. Mechnich. Tailoring the EB-PVD columnar microstructure to mitigate the infiltration of CMAS in 7YSZ thermal barrier coatings. *Journal of the European Ceramic Society*, 37(1):261–270, 2017. One citation in page [XLVI](#).
- [124] D. Naumenko, V. Shemet, L. Singheiser, and W. J. Quadackers. Failure mechanisms of thermal barrier coatings on mcraly-type bondcoats associated with the formation of the thermally grown oxide. *Journal of Materials Science*, 44(7):1687–1703, Apr 2009. 2 citations in pages [XXXVII](#) and [XXXVIII](#).
- [125] P. Nguyen, A. G. Kotousov, S. Y. Ho, and S. Wildy. Investigation of thermo-mechanical properties of slurry based thermal barrier coatings under repeated thermal shock. In *Key Engineering Materials*, volume 417, pages 197–200. Trans Tech Publ, 2010. One citation in page [XV](#).
- [126] J. R. Nicholls, K. Lawson, A. Johnstone, and D. Rickerby. Methods to reduce the thermal conductivity of EB-PVD tbc. *Surface and Coatings Technology*, 151:383–391, 2002. One citation in page [XIX](#).
- [127] D. Nissley, T. Meyer, and K. P. Walker. Life prediction and constitutive models for engine hot section anisotropic materials program. 1992. 2 citations in pages [XXXIV](#) and [XXXV](#).
- [128] W. Nowak, D. Naumenko, G. Mor, F. Mor, D. E. Mack, R. Vassen, L. Singheiser, and W. Quadackers. Effect of processing parameters on mcraly bondcoat roughness and lifetime of aps-tbc systems. *Surface and coatings technology*, 260:82–89, 2014. One citation in page [XI](#).
- [129] C. Oskay, M. Rudolphi, E. Affeldt, M. Schütze, and M. Galetz. Evolution of microstructure and mechanical properties of nial-diffusion coatings after thermocyclic exposure. *Intermetallics*, 89:22–31, 2017. One citation in page [XXIII](#).
- [130] N. P. Padture, M. Gell, and E. H. Jordan. Thermal barrier coatings for gas-turbine engine applications. *Science*, 296(5566):280–284, 2002. One citation in page [VII](#).
- [131] D. Pan, M. W. Chen, P. K. Wright, and K. J. Hemker. Evolution of a diffusion aluminate bond coat for thermal barrier coatings during thermal cycling. *Acta Mater.*, 51(8):2205–2217, 2003. 2 citations in pages [XXI](#) and [XXIII](#).
- [132] F. Perrudin, C. Rio, M. Vidal-Sétif, C. Petitjean, P.-J. Panteix, and M. Vilasi. Gadolinium oxide solubility in molten silicate: dissolution mechanism and stability of  $\text{Ca}_2\text{Gd}_8(\text{SiO}_4)_6\text{O}_2$  and  $\text{Ca}_3\text{Gd}_2(\text{Si}_3\text{O}_9)_2$  silicate phases. *Journal of the European Ceramic Society*, 37(7):2657–2665, 2017. One citation in page [XLVII](#).

- [133] F. Pettit and G. Goward. Oxidation–corrosion–erosion mechanisms of environmental degradation of high-temperature materials. *Coatings for High-Temperature Applications*, pages 1–32, 1983. One citation in page [IX](#).
- [134] P. S. Phani and W. Oliver. A critical assessment of the effect of indentation spacing on the measurement of hardness and modulus using instrumented indentation testing. *Materials & Design*, 164:107563, 2019. One citation in page [XXIII](#).
- [135] R. Pillai, M. Taylor, T. Galiullin, A. Chyrkin, E. Wessel, H. Evans, and W. Quadackers. Predicting the microstructural evolution in a multi-layered corrosion resistant coating on a ni-base superalloy. *Materials at high temperatures*, 35(1-3):78–88, 2018. One citation in page [LII](#).
- [136] A. Pineau. Influence of uniaxial stress on the morphology of coherent precipitates during coarsening - elastic energy considerations. *Acta Metall.*, 24:559–564, 1976. No citations.
- [137] F. M. Pitek and C. G. Levi. Opportunities for tbc in the zro2-yo1.5-tao2.5 system. *Surface and Coatings Technology*, 201(12):6044–6050, 2007. One citation in page [XVII](#).
- [138] P. Planques, V. Vidal, P. Lours, V. Proton, F. Crabos, J. Huez, and B. Viguier. Characterization of the mechanical properties of thermal barrier coatings by 3 points bending tests and modified small punch tests. *Surface and Coatings Technology*, 332:40–46, 2017. One citation in page [XXVI](#).
- [139] D. L. Poerschke, T. L. Barth, and C. G. Levi. Equilibrium relationships between thermal barrier oxides and silicate melts. *Acta Materialia*, 120:302–314, 2016. One citation in page [XLVII](#).
- [140] D. L. Poerschke, R. W. Jackson, and C. G. Levi. Silicate deposit degradation of engineered coatings in gas turbines: progress toward models and materials solutions. *Annual Review of Materials Research*, 47:297–330, 2017. 2 citations in pages [XLV](#) and [XLIX](#).
- [141] E. Pons. *Propriétés d’adhérence de revêtements projetés plasma sur substrats fragiles: caractérisation et identification de lois d’interface par Modèles de Zones Cohésives*. PhD thesis, Université Grenoble Alpes, 2016. 3 citations in pages [XXV](#), [XXVI](#), and [XXX](#).
- [142] D. Poquillon and D. Monceau. Initiation of geometric roughening in polycrystalline metal films. *Oxidation of metals*, 59(3-4):409 – 431, 2003. 2 citations in pages [L](#) and [LI](#).
- [143] D. Poquillon, N. Vialas, and D. Monceau. Numerical modelling of diffusion coupled with cyclic oxidation. application to alumina-forming coatings

- used for industrial gas turbine blades. In *Materials Science Forum*, volume 595, pages 159–168. Trans Tech Publ, 2008. One citation in page [LII](#).
- [144] G. Pujol, F. Ansart, J.-P. Bonino, A. Malié, and S. Hamadi. Step-by-step investigation of degradation mechanisms induced by CMAS attack on YSZ materials for tbc applications. *Surface and Coatings Technology*, 237:71–78, 2013. One citation in page [XLVI](#).
- [145] K. Rahmani and S. Nategh. Influence of aluminide diffusion coating on low cycle fatigue properties of rené 80. *Materials Science and Engineering: A*, 486(1-2):686–695, 2008. One citation in page [XLII](#).
- [146] B. Rajasekaran, G. Mauer, and R. Vaßen. Enhanced characteristics of hvof-sprayed mcraly bond coats for tbc applications. *Journal of thermal spray technology*, 20(6):1209–1216, 2011. One citation in page [X](#).
- [147] N. Rakotomalala. *Coupled thermomechanical simulation of the failure of thermal barrier coatings of turbine blades (in French)*. PhD thesis, Mines ParisTech, 2014. 3 citations in pages [LIV](#), [LVIII](#), and [LIX](#).
- [148] H.-J. Rätzer-Scheibe and U. Schulz. The effects of heat treatment and gas atmosphere on the thermal conductivity of aps and EB-PVD PYSZ thermal barrier coatings. *Surface and coatings technology*, 201(18):7880–7888, 2007. One citation in page [XXXIII](#).
- [149] H.-J. Rätzer-Scheibe, U. Schulz, and T. Krell. The effect of coating thickness on the thermal conductivity of EB-PVD PYSZ thermal barrier coatings. *Surface and Coatings Technology*, 200(18-19):5636–5644, 2006. 2 citations in pages [XVIII](#) and [XIX](#).
- [150] R. C. Reed. *The superalloys: fundamentals and applications*. Cambridge university press, 2008. One citation in page [VII](#).
- [151] L. Remy. Oxidation effects in high temperature creep and fatigue of engineering alloys. In *Corrosion–Deformation Interactions; Fontainebleau; France; 5-7 Oct. 1992; Corrosion–Deformation Interactions*, pages 425–459, Avenue du Hoggar, Zone Industrielle de Courtaboeuf, B.P. 112, F-91944 Les Ulis Cedex A, France, 5-7 Oct. 1992 1993. Ecole Nationale Supérieure des Mines de Paris, Les Editions de Physique. One citation in page [XXI](#).
- [152] E. Renner, Y. Gaillard, F. Richard, F. Amiot, and P. Delobelle. Sensitivity of the residual topography to single crystal plasticity parameters in berkovich nanoindentation on fcc nickel. *International Journal of Plasticity*, 77:118–140, 2016. One citation in page [XXIII](#).
- [153] S. Rezanka, G. Mauer, and R. Vaßen. Improved thermal cycling durability of thermal barrier coatings manufactured by ps-pvd. *Journal of thermal spray technology*, 23(1-2):182–189, 2014. One citation in page [XV](#).

- [154] K. Roe and T. Siegmund. An irreversible cohesive zone model for interface fatigue crack growth simulation. *Engineering Fracture Mechanics*, 70(2):209 – 232, 2003. One citation in page [LIV](#).
- [155] P. Sallot. *Modélisation de la durée de vie d'un revêtement aluminofumeur en conditions de sollicitations thermo-mécaniques (in French)*. PhD thesis, Mines ParisTech, 2012. 3 citations in pages [XXXVIII](#), [LVIII](#), and [LIX](#).
- [156] P. Sallot, V. Maurel, L. Rémy, F. N'Guyen, and A. Longuet. Microstructure evolution of a platinum-modified nickel-aluminide coating during thermal and thermo-mechanical fatigue. *Metal. Mater. Trans. A*, 46(10):4589–4600, 2015. One citation in page [XLIII](#).
- [157] S. Sampath, U. Schulz, M. O. Jarligo, and S. Kuroda. Processing science of advanced thermal-barrier systems. *MRS bulletin*, 37(10):903–910, 2012. One citation in page [VII](#).
- [158] H. Sapardanis. *Fissuration à l'interface d'un revêtement plasma céramique et d'un substrat métallique sous sollicitations dynamique et quasi-statique multiaxiales (in French)*. PhD thesis, Paris Sciences et Lettres, 2016. One citation in page [LX](#).
- [159] H. Sapardanis, V. Maurel, A. Köster, S. Duvinage, F. Borit, and V. Guipont. Influence of macroscopic shear loading on the growth of an interfacial crack initiated from a ceramic blister processed by laser shock. *Surface and Coatings Technology*, 291:430–443, 2016. 4 citations in pages [XXIX](#), [LVIII](#), [LIX](#), and [LX](#).
- [160] U. Schulz, M. Menzebach, C. Leyens, and Y. Yang. Influence of substrate material on oxidation behavior and cyclic lifetime of EB-PVD tbc systems. *Surface and Coatings Technology*, 146:117–123, 2001. 2 citations in pages [XII](#) and [XIII](#).
- [161] J. Shi, A. M. Karlsson, B. Baufeld, and M. Bartsch. Evolution of surface morphology of thermo-mechanically cycled nicocraly bond coats. *Materials Science and Engineering: A*, 434(1-2):39–52, 2006. 2 citations in pages [LIV](#) and [LV](#).
- [162] C. Shih. Cracks on bimaterial interfaces: elasticity and plasticity aspects. *Materials Science and Engineering: A*, 143(1-2):77–90, 1991. One citation in page [LIV](#).
- [163] D. Siebörger, H. Knake, and U. Glatzel. Temperature dependence of the elastic moduli of the nickel-base superalloy CMSX-4 and its isolated phases. *Mat. Sci. and Engng A*, 298:26–33, 2001. One citation in page [XXXV](#).
- [164] G. Simmons and H. Wang. *Single crystal elastic constants and calculated aggregated properties: a handbook*. The MIT Press, Cambridge, MA, 1971. 2 citations in pages [XXXIV](#) and [XXXV](#).

- [165] M. Singleton, J. Murray, and P. Nash. Aluminum-nickel. *Binary alloy phase diagrams*, 1:140–143, 1986. One citation in page [LII](#).
- [166] J. L. Smialek. The chemistry of Saudi Arabian sand: a deposition problem on helicopter turbine airfoils. *in: 3rd International SAMPE Metals Conference*, M63, 1992. 2 citations in pages [XLV](#) and [XLVI](#).
- [167] J. L. Smialek. Universal characteristics of an interfacial spalling cyclic oxidation model. *Acta Materialia*, 52(8):2111 – 2121, 2004. One citation in page [L](#).
- [168] C. Smithells. Metals reference book, edited by ea brandes, 1983. 2 citations in pages [XXXIV](#) and [XXXV](#).
- [169] R. Soullignac, V. Maurel, L. Remy, and A. Koster. Cohesive zone modelling of thermal barrier coatings interfacial properties based on three-dimensional observations and mechanical testing. *Surf. Coat. Technol.*, 237:95 – 104, 2013. 2 citations in pages [XXVI](#) and [LVIII](#).
- [170] T. Steinke, D. Sebold, D. E. Mack, R. Vaßen, and D. Stöver. A novel test approach for plasma-sprayed coatings tested simultaneously under CMAS and thermal gradient cycling conditions. *Surface and Coatings Technology*, 205(7):2287–2295, 2010. One citation in page [XLVIII](#).
- [171] F. Stott, D. De Wet, and R. Taylor. Degradation of thermal-barrier coatings at very high temperatures. *MRS Bulletin*, 19(10):46–49, 1994. One citation in page [XLVI](#).
- [172] M. Subanovic, D. Sebold, R. Vassen, E. Wessel, D. Naumenko, L. Singheiser, and W. Quadakkers. Effect of manufacturing related parameters on oxidation properties of mcraly-bondcoats. *Materials and corrosion*, 59(6):463–470, 2008. One citation in page [XI](#).
- [173] I. Šulák, K. Obrtlík, L. Čelko, T. Chráska, D. Jech, and P. Gejdoš. Low cycle fatigue performance of ni-based superalloy coated with complex thermal barrier coating. *Materials Characterization*, 139:347–354, 2018. One citation in page [XLII](#).
- [174] A. Suzuki and C. Rae. Secondary reaction zone formations in coated ni-base single crystal superalloys. In *Journal of Physics: Conference Series*, volume 165, page 012002. IOP Publishing, 2009. One citation in page [XII](#).
- [175] N. Ta, L. Zhang, and Y. Du. A trial to design  $\gamma/\gamma'$  bond coat in ni–al–cr mode tbc's aided by phase-field simulation. *Coatings*, 8(12):421, 2018. 2 citations in pages [LII](#) and [LIII](#).
- [176] M. Taylor, H. Evans, C. Ponton, and J. Nicholls. A method for evaluating the creep properties of overlay coatings. *Surf. Coat. Technol.*, 124:13–18, 2000. 2 citations in pages [XX](#) and [XXI](#).

- [177] T. Taylor, D. Appleby, A. Weatherill, and J. Griffiths. Plasma-sprayed yttria-stabilized zirconia coatings: structure-property relationships. *Surface and Coatings Technology*, 43:470–480, 1990. One citation in page [XIII](#).
- [178] B. Ter-Ovanesian, A. Villani, É. Andrieu, and S. Forest. Oxidation-assisted cracking. In *Mechanics-Microstructure-Corrosion Coupling*, pages 339–358. Elsevier, 2019. One citation in page [LII](#).
- [179] D. Texier, C. Cadet, T. Straub, C. Eberl, and V. Maurel. Tensile behavior of air plasma spray mcraly coatings: Role of high temperature agings and process defects. *Metal. Mater. Trans. A*, 51:2766–2777, 2020. One citation in page [XXIII](#).
- [180] D. Texier, D. Monceau, F. Crabos, and E. Andrieu. Tensile properties of a non-line-of-sight processed beta-gamma-gamma prime MCrAlY coating at high temperature. *Surface & Coatings Technology*, 326:28–36, Oct. 2017. One citation in page [XXXV](#).
- [181] D. Texier, D. Monceau, Z. Hervier, and E. Andrieu. Effect of interdiffusion on mechanical and thermal expansion properties at high temperature of a MCrAlY coated Ni-based superalloy. *Surface & Coatings Technology*, 307:81–90, Dec. 2016. One citation in page [XXXIV](#).
- [182] D. Texier, D. Monceau, S. Selezneff, A. Longuet, and E. Andrieu. High temperature micromechanical behavior of a pt-modified nickel aluminide bond-coating and of its interdiffusion zone with the superalloy substrate. *Mater. Sci. Engng. A*, pages 1–6, 2020. 3 citations in pages [XXI](#), [XXIV](#), and [XXXV](#).
- [183] P.-Y. Théry. *Adhérence de barrières thermiques pour aube de turbine avec couche de liaison  $\beta$ -(Ni, Pt) Al ou  $\beta$ -NiAl (Zr) (in French)*. PhD thesis, 2007. One citation in page [LIX](#).
- [184] P. Y. Thery, M. Poulain, M. Dupeux, and M. Braccini. Adhesion energy of a YPSZ EB-PVD layer in two thermal barrier coating systems. *Surf. Coat. Technol.*, 202(4-7):648–652, 2007. 2 citations in pages [XXVI](#) and [XXVIII](#).
- [185] P. Y. Thery, M. Poulain, M. Dupeux, and M. Braccini. Spallation of two thermal barrier coating systems: experimental study of adhesion and energetic approach to lifetime during cyclic oxidation. *Journal of Materials Science*, 44(7):1726–1733, 2009. One citation in page [XXXVI](#).
- [186] M. Theveneau, V. Guipont, B. Marchand, F. Coudon, and V. Maurel. Damage monitoring and thermal cycling life of thermal barrier coating involving lasat (laser shock adhesion test). *46th ICMCTF, San Diego, CA*, 2019. 2 citations in pages [XXX](#) and [XXXI](#).

- [187] V. Tolpygo and D. Clarke. Wrinkling of  $\alpha$ -alumina films grown by oxidation. ii. oxide separation and failure. *Acta Materialia*, 46(14):5167–5174, 1998. One citation in page [XXXVII](#).
- [188] V. K. Tolpygo, D. Clarke, and K. Murphy. Evaluation of interface degradation during cyclic oxidation of EB-PVD thermal barrier coatings and correlation with tgo luminescence. *Surface and Coatings Technology*, 188:62–70, 2004. One citation in page [XXXVII](#).
- [189] V. K. Tolpygo and D. R. Clarke. On the rumpling mechanism in nickel-aluminide coatings: Part I: an experimental assessment. *Acta Mater.*, 52(17):5115–5127, 2004. One citation in page [XXXVIII](#).
- [190] E. Tzimas, H. Mullejans, S. D. Peteves, J. Bressers, and W. Stamm. Failure of thermal barrier coating systems under cyclic thermomechanical loading. *Acta Materialia*, 48(18-19):4699 – 4707, 2000. 5 citations in pages [XXXIII](#), [XXXIV](#), [XXXV](#), [XLII](#), and [XLIII](#).
- [191] K. VanEvery, M. J. Krane, R. W. Trice, H. Wang, W. Porter, M. Besser, D. Sordelet, J. Ilavsky, and J. Almer. Column formation in suspension plasma-sprayed coatings and resultant thermal properties. *Journal of thermal spray technology*, 20(4):817–828, 2011. One citation in page [XV](#).
- [192] R. Vassen, X. Cao, F. Tietz, D. Basu, and D. Stöver. Zirconates as new materials for thermal barrier coatings. *Journal of the American Ceramic Society*, 83(8):2023–2028, 2000. One citation in page [XVII](#).
- [193] R. Vaßen, H. Kaßner, G. Mauer, and D. Stöver. Suspension plasma spraying: process characteristics and applications. *Journal of thermal spray technology*, 19(1-2):219–225, 2010. One citation in page [XV](#).
- [194] J.-R. Vaunois, J.-M. Dorvaux, P. Kanouté, and J.-L. Chaboche. A new version of a rumpling predictive model in thermal barrier coatings. *European Journal of Mechanics - A/Solids*, 42:402 – 421, 2013. One citation in page [LIV](#).
- [195] J.-R. Vaunois, M. Poulain, P. Kanouté, and J.-L. Chaboche. Development of bending tests for near shear mode interfacial toughness measurement of EB-PVD thermal barrier coatings. *Engineering Fracture Mechanics*, 171:110 – 134, 2017. 5 citations in pages [XXVI](#), [XXVIII](#), [XXXVI](#), [XLI](#), and [LVIII](#).
- [196] M. Vidal-Setif, N. Chellah, C. Rio, C. Sanchez, and O. Lavigne. Calcium–magnesium–alumino-silicate (CMAS) degradation of EB-PVD thermal barrier coatings: Characterization of CMAS damage on ex-service high pressure blade tbc. *Surface and Coatings Technology*, 208:39–45, 2012. 2 citations in pages [XLV](#) and [XLVI](#).

- [197] M. Vidal-Setif, C. Rio, D. Boivin, and O. Lavigne. Microstructural characterization of the interaction between 8yps (EB-PVD) thermal barrier coatings and a synthetic cas. *Surface and Coatings Technology*, 239:41–48, 2014. 2 citations in pages [XLV](#) and [XLVI](#).
- [198] K. Von Niessen, M. Gindrat, and A. Refke. Vapor phase deposition using plasma spray-pvd. *Journal of thermal spray technology*, 19(1-2):502–509, 2010. One citation in page [XV](#).
- [199] C. Vorkötter, D. Mack, O. Guillon, and R. Vaßen. Superior cyclic life of thermal barrier coatings with advanced bond coats on single-crystal superalloys. *Surface and Coatings Technology*, 361:150–158, 2019. One citation in page [XII](#).
- [200] J. Wachtman. *Mechanical properties of Ceramics*. 1996. 2 citations in pages [XXXIV](#) and [XXXV](#).
- [201] C. Wagner. Theoretical Analysis of the Diffusion Processes Determining the Oxidation Rate of Alloys. *Journal of the Electrochemical Society*, 99(10):369–380, 1952. One citation in page [L](#).
- [202] H. Wang, R. B. Dinwiddie, and W. D. Porter. Development of a thermal transport database for air plasma sprayed zro 2-y 2 o 3 thermal barrier coatings. *Journal of thermal spray technology*, 19(5):879–883, 2010. One citation in page [XX](#).
- [203] H. Wei, X. Sun, Q. Zheng, H. Guan, and Z. Hu. Estimation of interdiffusivity of the nial phase in ni-al binary system. *Acta materialia*, 52(9):2645–2651, 2004. One citation in page [LII](#).
- [204] H. Wei, X. Sun, Q. Zheng, G. Hou, H. Guan, and Z. Hu. An inverse method for determination of the interdiffusivity in aluminide coatings formed on superalloy. *Surface and Coatings Technology*, 182(1):112 – 116, 2004. One citation in page [LII](#).
- [205] R. Wellman, G. Whitman, and J. Nicholls. CMAS corrosion of EB PVD TBCs: Identifying the minimum level to initiate damage. *Int. J. Refract. Metals Hard Mater.*, 28:124–132, 2010. One citation in page [XLVI](#).
- [206] G. Witz, V. Shklover, W. Steurer, S. Bachegowda, and H.-P. Bossmann. High-temperature interaction of yttria stabilized zirconia coatings with CaO–MgO–Al<sub>2</sub>O<sub>3</sub>–SiO<sub>2</sub> (CMAS) deposits. *Surface and Coatings Technology*, 265:244–249, 2015. One citation in page [XLVI](#).
- [207] P. Wright and A. Evans. Mechanisms governing the performance of thermal barrier coatings. *Current Opinion in Solid State and Materials Science*, 4(3):255 – 265, 1999. One citation in page [VII](#).

- [208] P. K. Wright. Influence of cyclic strain on life of a pvd tbc. *Materials Science and Engineering A*, 245(2):191 – 200, 1998. One citation in page [LIX](#).
- [209] J. Wu, H.-B. Guo, Y.-Z. Gao, and S.-K. Gong. Microstructure and thermo-physical properties of yttria stabilized zirconia coatings with CMAS deposits. *Journal of the European Ceramic Society*, 31(10):1881–1888, 2011. One citation in page [XLVI](#).
- [210] J. Wu, X. Wei, N. P. Padture, P. G. Klemens, M. Gell, E. García, P. Miranzo, and M. I. Osendi. Low-thermal-conductivity rare-earth zirconates for potential thermal-barrier-coating applications. *Journal of the American Ceramic Society*, 85(12):3031–3035, 2002. One citation in page [VII](#).
- [211] H. Xu and H. Guo. *Thermal barrier coatings*. Elsevier, 2011. One citation in page [VIII](#).
- [212] Z.-H. Xu, Y. Yang, P. Huang, and X. Li. Determination of interfacial properties of thermal barrier coatings by shear test and inverse finite element method. *Acta materialia*, 58(18):5972–5979, 2010. 2 citations in pages [XXV](#) and [XXVII](#).
- [213] N. Yanar, F. Pettit, and G. Meier. Failure characteristics during cyclic oxidation of yttria stabilized zirconia thermal barrier coatings deposited via electron beam physical vapor deposition on platinum aluminide and on nicocraly bond coats with processing modifications for improved performances. *Metallurgical and Materials Transactions A*, 37(5):1563–1580, 2006. 3 citations in pages [XXX](#), [XXXVII](#), and [XL](#).
- [214] K. Yuan, R. Eriksson, R. L. Peng, X.-H. Li, S. Johansson, and Y.-D. Wang. Modeling of microstructural evolution and lifetime prediction of mcraly coatings on nickel based superalloys during high temperature oxidation. *Surface and Coatings Technology*, 232:204–215, 2013. One citation in page [LII](#).
- [215] P. D. Zavattieri, L. G. Hector Jr, and A. F. Bower. Cohesive zone simulations of crack growth along a rough interface between two elastic–plastic solids. *Engineering Fracture Mechanics*, 75(15):4309–4332, 2008. One citation in page [XXXI](#).
- [216] L. Zhang, Y. Du, Q. Chen, I. Steinbach, and B. Huang. Atomic mobilities and diffusivities in the fcc, l12 and b2 phases of the ni-al system. *International journal of materials research*, 101(12):1461–1475, 2010. One citation in page [LII](#).
- [217] L. Zhang, I. Steinbach, and Y. Du. Phase-field simulation of diffusion couples in the ni–al system. *International Journal of Materials Research*, 102(4):371–380, 2011. One citation in page [LII](#).

- [218] P. Zhang, E. Sadeghimeresht, S. Chen, X.-H. Li, N. Markocsan, S. Joshi, W. Chen, I. A. Buyanova, and R. L. Peng. Effects of surface finish on the initial oxidation of hvaf-sprayed nicocraly coatings. *Surface and Coatings Technology*, 364:43–56, 2019. One citation in page [X](#).
- [219] D. Zhu and R. A. Miller. Investigation of thermal fatigue behavior of thermal barrier coating systems. *Surface and Coatings Technology*, 94:94–101, 1997. One citation in page [XLIII](#).
- [220] D. Zhu and R. A. Miller. Development of advanced low conductivity thermal barrier coatings. *International Journal of Applied Ceramic Technology*, 1(1):86–94, 2004. One citation in page [XVII](#).
- [221] W. Zhu, L. Yang, J. Guo, Y. Zhou, and C. Lu. Determination of interfacial adhesion energies of thermal barrier coatings by compression test combined with a cohesive zone finite element model. *International Journal of Plasticity*, 64:76 – 87, 2015. 2 citations in pages [XXVI](#) and [XXXVI](#).
- [222] W. Zhu, Z. Zhang, L. Yang, Y. Zhou, and Y. Wei. Spallation of thermal barrier coatings with real thermally grown oxide morphology under thermal stress. *Materials & Design*, 146:180 – 193, 2018. One citation in page [L](#).
- [223] N. Zotov, M. Bartsch, and G. Eggeler. Thermal barrier coating systems analysis of nanoindentation curves. *Surface and Coatings Technology*, 203(14):2064–2072, 2009. 2 citations in pages [XXIII](#) and [XXIV](#).